Printing Mechanism and Microstructure Control in Wire-laser Directed Energy Deposition of Metallic Materials

---

A
Dissertation
Presented to
the faculty of the School of Engineering and Applied Science
University of Virginia

---

in partial fulfillment
of the requirements for the degree

Doctor of Philosophy

by

Lin Gao

December 2023

APPROVAL SHEET

This
Dissertation
is submitted in partial fulfillment of the requirements
for the degree of
Doctor of Philosophy

Author: Lin Gao

This Dissertation has been read and approved by the examing committee:

Advisor: Tao Sun

Advisor:

Committee Member: Bi-Cheng Zhou

Committee Member: Sean R. Agnew

Committee Member: Andrew Chuang

Committee Member: Xiaodong Li

Committee Member:

Committee Member:

Accepted for the School of Engineering and Applied Science:

Jennifer L. West, School of Engineering and Applied Science
December 2023

Contents

List of Figures

List of Tables

List of Abbreviations and Symbols

Abbreviations and Symbols	**Definition**
DED	Directed energy deposition
AM	Additive manufacturing
LED	Linear energy density
VED	Volumetric energy density
LPBF	Laser powder bed fusion
FCC	Face-centered cubic
BCC	Body-centered cubic
SS	Stainless Steel
L	Liquid
CET	Columnar-to-equiaxed transition
ISRO	Icosahedral short-range ordering
EBSD	Electron back-scattered diffraction
EDS	Energy-dispersive spectroscopy
CNT	Classic nucleation theory
HCP	Hexagonal-close-packed
TEM	Transmission electron microscopy
WAAM	Wire arc additive manufacturing
PDF	Pair distribution function

RAPDF	Rapid acquisition pair distribution function
APS	Advanced Photon Source
ANL	Argonne National Laboratory
CTE	Coefficient of thermal expansion
SEM	Scanning electron microscopy
TD	Transvers direction
SD	Scanning direction
BD	Building direction
IPF	Inverse pole figure
FEAR	Fitted ellipse aspect ratio
G	Temperature gradient
R	Solidification rate
XCT	X-ray computed tomography
NIR	Near-infrared
EVPSC	Elastic-viscoplastic self-consistent
CRSS	Critical resolved shear stress
KAM	Kernel average misorientation
PF	Pole figures
ODF	Orientation distribution function
GND	Geometry necessary dislocation

UTS	Ultimate tensile strength
ADP	Atomic displacement parameter
MRO	Medium-range ordering
ICO	Icosahedral
SRO	Short-range ordering
TB	Twinning boundary
E_L	Local energy density
β	Energy absorption coefficient
P	Laser power
d	Laser beam size
V	traveling (scanning) speed
F	wire feeding rate
A	Cross-sectional area of feedstock wire
$I(Q)$	X-ray total scattering
Q	Scattering vector
$G(r)$	Reduced pair distribution function
$S(Q)$	Total-scattering structure function
T_L	Liquidus temperature
T_S	Solidus temperature

Acknowledgment

First and foremost, I would like to express my deepest gratitude to my Ph.D. advisor, Prof. Tao Sun. As the first Ph.D. student in his group, I learned a lot from him, not only about professional knowledge but also the rigorous research attitude. His mentoring and patience continuously supported me in pursuing each milestone of my Ph.D. journey. Also, I would like to acknowledge my dissertation committee, including Prof. Bi-Cheng Zhou, Prof. Sean R. Agnew, Prof. Xiaodong Li, Dr. Andrew C. Chuang, and Prof. Tao Sun. Without their guidance and support, this dissertation could not have been finalized and presented. I appreciate Prof. Sean R. Agnew, Prof. Ji Ma, and Prof. Leonid Zhigilei's professional help in my research. I would also like to thank all the professors who have taught me in their classes, including Prof. Elizabeth J. Opila, Prof. Sean R. Agnew, Prof. Tao Sun, Prof. Petra Reinke, Prof. Kyusang Lee, Prof. Richard Martukanitz, Prof. Bi-Cheng Zhou, Prof. Haydn Wadley, Prof. James Burns, Prof. James Howe. I would like to thank all the NMCF staff, especially Richard White and Diane Dickie, for training me to operate the characterization instruments. I also appreciate all the staff of our MSE department, especially Bryana Amador, Tanner R. Fitzgerald, Ig Jakovac, Jeannie Reese, Tonya J. Reynolds, Sherri Sullivan, Jerry Weaver, and Peggy Gibson (who retired in 2021).

I appreciate the beamline scientists and engineers at the Advanced Photon Source, especially Dr. Andrew C. Chuang, Dr. Peter Kenesei, Pavel D. Shevchenko, Dr. Viktor Nikitin, Alex Deriy, and Ali Mashayekhi, for their help and support on my synchrotron experiments. I thank Matt Viton, Jesus Peña Rodriguez in Meltio and Marcin Serdeczny in Flow Science Inc. for their technical

support in using the DED system and Flow-3D software. I also thank my UVa-MSE colleagues and friends, especially Dr. Wenhao Lin, Dr. Jishnu Bhattaryya, Yuan Xu, and Chaobo Chen, for their help in my research. I also appreciate the help and support from my group mates, including Dr. Zhongshu Ren, Kyle Mumm, Lilly Balderson, Arthur Zhang, and undergraduate researchers.

I am grateful to my wife, Xiaoming Li, and my parents. Their unlimited love and patience provided important spiritual support throughout my Ph.D. journey.

Abstract

Wire-laser directed energy deposition (DED) is a metal additive manufacturing (AM) technology widely used by various sectors to fabricate large-scale components due to its fast production rate, high material utilization, and low manufacturing cost. The emerging multi-laser printhead with a coaxial wire feeder can significantly reduce the directional dependence in the printing process; however, the fundamental knowledge of this new process is still limited. For this purpose, this dissertation aims to develop a deep understanding of the coaxial wire-laser DED process and offer fresh insights into the microstructure control of as-printed samples, further expediting the wide adoption of this technique in industrial production.

This dissertation employed various characterization approaches and high-fidelity multi-physics simulations to investigate the coaxial wire-laser DED of 316L stainless steel and Inconel 718 alloys. This dissertation comprises three research chapters: Chapters 3, 4, and 5. Chapter 3 focuses on a wire-laser DED process of Inconel 718 alloy with intentionally constrained energy input. O*perando* synchrotron x-ray characterization and multi-physics modeling were employed in synergy to investigate the printing behavior and microstructure evolution in the melt pool. This study revealed that, under this specific printing condition, the feedstock wire only partially melted as it entered the melt pool. Despite the wire continuing to be heated and melted by the surrounding melt pool, solid particles, such as MC-carbide, were released and remained in the bottom region of the rear melt pool, consequently resulting in microstructure heterogeneity in the as-printed part. Chapter 4 introduces a wiggle deposition strategy to control the solidification microstructure in wire-laser DED by generating an unstable melt pool. A certain level of melt-pool instability altered the crystallographic texture and, consequently, the mechanical anisotropy of printed samples. Chapter 5 focuses on an "abnormal" columnar-to-equiaxial transition and icosahedral-short-range-ordering-mediated solidification in metal AM. *Operando* high-energy synchrotron x-ray diffraction and total-scattering analysis were adopted to investigate the atomic structure of the melt pool and the role of atomic ordering in the rapid solidification of metal AM processes. This chapter presents a comprehensive understanding of the "abnormal" columnar-to-equiaxial transition in metal AM and provides experimental insights to enrich the modern solidification theory.

Keywords: Wire-laser directed energy deposition, operando synchrotron x-ray characterization, multi-physics simulation, microstructure control.

1. Introduction

1.1 Metal additive manufacturing and wire-laser directed energy deposition

Flexible design and integrated manufacturing are of extraordinary significance for technological innovation and industrial sustainability. Additive manufacturing (AM), also known as 3D printing, is a revolutionary manufacturing technology that can directly produce parts with near-net shapes through a layer-by-layer fabrication strategy. The emergence and development of this technology open up new opportunities for industries to manufacture products with complex shapes and/or materials with low workability directly [1,2]. Therefore, metal AM is now widely accepted for designing and producing functional and structural components for aerospace, medical, energy, and automotive applications. A prominent example of its application in the aerospace sector is the production of the fuel nozzle for the GE LEAP aero engine (Fig. 1.1). Metal AM allows the one-step production of complex parts, reducing the need to assemble multiple components. In addition to lowering costs, AM offers significant improvements in weight reduction and strengthening for the fabricated nozzles because this manufacturing technique allows for the optimization of the nozzle's interior channels. As reported, the fuel nozzle manufactured by AM is 25% lighter and stronger than the counterpart manufactured using conventional methods. Due to the above advantages, metal AM techniques are now beginning to replace traditional manufacturing processes in producing certain parts. Meanwhile, various AM techniques have been developed to meet the unique demands of processing different components and materials.

Figure 1.1*: A fuel nozzle for the GE LEAP aero engine fabricated by metal AM [3].*

Wire-laser directed energy deposition (DED) is one of the mainstream AM techniques for producing metallic components. This technique employs one or multiple high-power laser beams to directly melt the wire feedstock fed through the deposition head, which scans across the build platform to print patterns based on computer designs [4,5]. Wire-laser DED exhibits a much higher deposition rate than most other AM techniques, making it advantageous for rapidly building large parts. Furthermore, wire feedstock is cheaper and more convenient to store than metallic powders, which significantly reduces the manufacturing cost and enhances the accessibility of this AM technique. In addition, the wire-laser DED system can have the exclusive hot-wire function built in to preheat the filler material as it is fed through the printhead [6]. This function allows it to efficiently process materials such as aluminum alloys with relatively low laser absorptivity. Additionally, the multi-axis motion control and flexible material feeding in the DED system make this technique highly effective for repairing and coating high-value parts and producing compositionally graded materials [7]. Benefiting from the user-friendly operation system, more commercial wire-laser DED machines enter the scene, further popularizing this technique in academic research and industrial production.

1.2 Coaxial wire-laser configuration of the deposition head

According to the form of input materials, DED can be categorized as wire-fed and powder-blown DED. Wire-fed DED offers higher material utilization, faster deposition rate, greater energy efficiency, fewer structural defects, and better surface quality of the printed parts compared to the powder-blown feeding option [8]. Due to these advantages, wire-laser DED has been widely used in aerospace, automobile, and energy industries for building large-scale components. The wire DED technology was initially developed by Harwell *et al.* in 2000 [9]. The deposition head in the first-generation wire DED system was configured with a center-vertical laser beam and an off-angle wire feeding system, as shown in Fig. 1.2a. However, the printing process using such a deposition head exhibits significant direction dependence because of the asymmetrical material feeding [10]. For example, different geometry conditions between the wire feeding direction and deposition direction can significantly affect the deposition quality. Hence, lateral wire feeding limits the flexibility of adopting different deposition strategies. This issue has been addressed recently by the development of the coaxial deposition head [11]. Figure 1.2b is the schematic diagram showing a representative coaxial deposition head. In this case, the wire is fed through the center of the deposition head, and multiple laser beams surrounding the wire focus on the wire tip or deposition region. By contrast, this innovative design provides a more uniform laser distribution, thereby promoting compositional and structural homogeneity in as-printed products. Owing to these advantages, the wire DED based on the coaxial deposition head is gaining more and more attention.

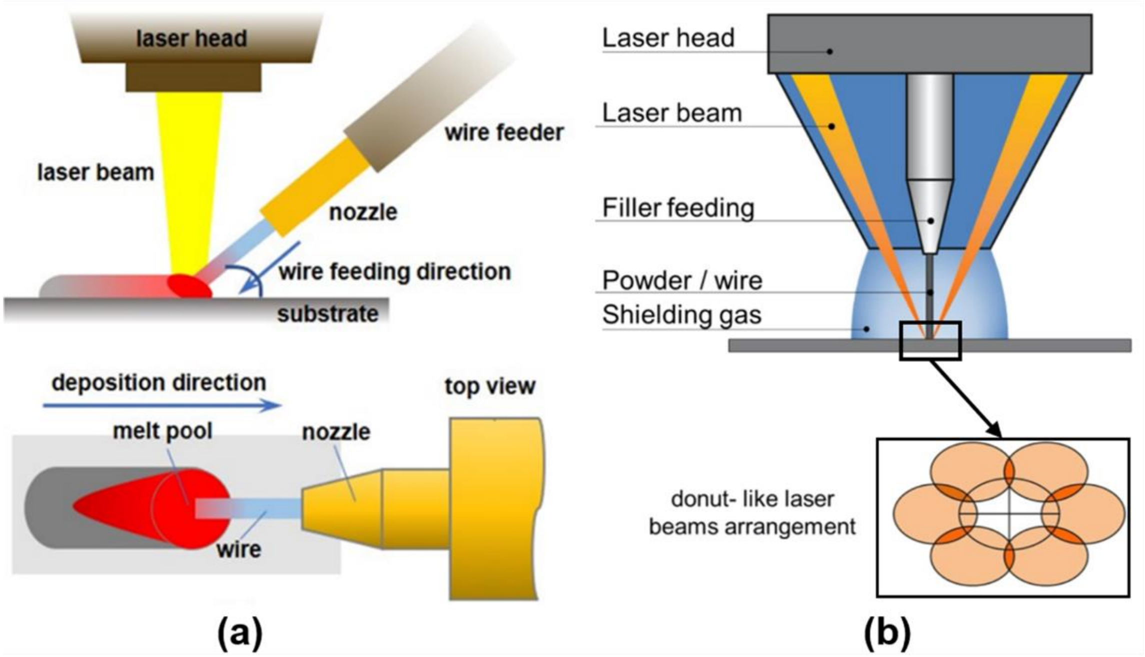

Figure 1.2*: Schematic diagrams of wire laser DED with (a) lateral and (b) coaxial wire feeding [8,10].*

In coaxial wire-laser DED, the near-annular energy distribution and unique interaction between the wire and melt pool led to more complex printing behavior and unexpected microstructures of the printed samples, such as unique microstructure heterogeneity. Despite many efforts made to investigate the coaxial wire DED process, the understanding of some underlying mechanisms remains limited. To accelerate the adoption of this technique in the industry, additional investigations, assisted by advanced characterizations (such as *operando* synchrotron techniques) and multi-physics modeling, are required to fill the knowledge gap.

1.3 Overview of principal Physics involved in DED processes

Unlike traditional manufacturing methods such as casting, AM processes involve more complex physical events, which leads to unique microstructures and competitive performances of AM samples [12–14]. The energy transfer from the heat source to feedstock materials governs the AM process, which can be described by local energy density (E_L). The E_L can be obtained by:

$$E_L = \frac{\beta P}{dV} \qquad \text{eq. 1.1}$$

where β, P, d, and V are energy absorption coefficient, laser power, beam size, and traveling (scanning) speed, respectively [15]. Laser absorptivity is a material-dependent parameter. For example, Fe and Ni typically present much higher laser absorption than Al and Cu. It also should be noted that the laser absorptivity of materials is relevant to several factors, such as laser wavelength, temperature, and the incident angle of the laser. The laser powder and traveling speed are two parameters that can be directly controlled and adjusted in printing. Adopting appropriate AM parameters is critical for producing high-quality and consistent products. Each material has a specific processing window for the AM printing, such as the combination of P-V conditions. Overheating or underheating can both be detrimental to stable printing. In addition to E_L, linear energy density (LED) and volumetric energy density (VED) are standard parameters used to evaluate the energy input during DED processing. They can be calculated through the following equations:

$$LED = \frac{P}{V} \qquad \text{eq. 1.2}$$

$$VED = \frac{P}{AF} \qquad \text{eq. 1.3}$$

where A and F correspond to the cross-sectional area and feeding rate (in length per unit of time) of feedstock wire. The VED indicates the energy input per unit volume of the feedstock, which is practical for describing the energy balance between input and deposition. This parameter has been demonstrated to play a crucial role in controlling melting behavior, thereby affecting printing quality [16]. Excessive energy input can cause a pendant droplet at the wire tip, which may then result in dripping balling beads once gravity overcomes the surface tension. Conversely, insufficient energy input can cause wire bending and stubbing, as the filler wire cannot completely melt into the melt pool. Unstable printing may occur under either overheating or underheating conditions, leading to discontinuous and uneven printing tracks. Thus, achieving a stable printing process and reducing defects requires a good balance between the energy input and wire feeding rate.

During a general AM process, the focused laser can rapidly melt feedstock materials and generate a melt pool at the printing region, i.e., a superheated molten metal region. Because wire-laser DED typically employs a large laser beam to ensure sufficient melting of feedstocks, a large melt pool is generated and remains in conduction mode without generating the "keyhole."

Keyholing commonly occurs in laser powder bed fusion (LPBF) and is pertinent to the severe evaporation depression induced by a laser with highly concentrated energy distribution. The conduction mode of wire-laser DED prevents the formation of printing defects induced by an unstable keyhole. On the other hand, the penetration depth of the melt pool is shallow into the preceding layer but still provides enough bonding between these two deposited layers.

The intense heating and heat conduction result in severe temperature variations within the melt pool, that is, a large temperature gradient. The temperature gradient typically ranges from 100 to 1000 K/mm for the DED process and varies with printing parameters [15]. The temperature variation leads to density and surface tension gradients, thereby driving significant melt flow within the melt pool and on the free surface. The melt-pool dynamics play a critical role in governing heat transfer and composition transfer inside the melt pool [17]. The rear boundary of the melt pool consists of a mushy zone mixed with both solid and liquid phases. Rapid and directional solidification takes place through the mushy zone due to fast cooling and the large temperature gradient. Solidification microstructures strongly depend on the temperature gradient (G) and solidification rate (R), as described by the solidification selection map shown in Fig. 1.3. The solidification rate, also known as the growth rate, refers to the moving velocity of the liquid/solid (L/S) interface.

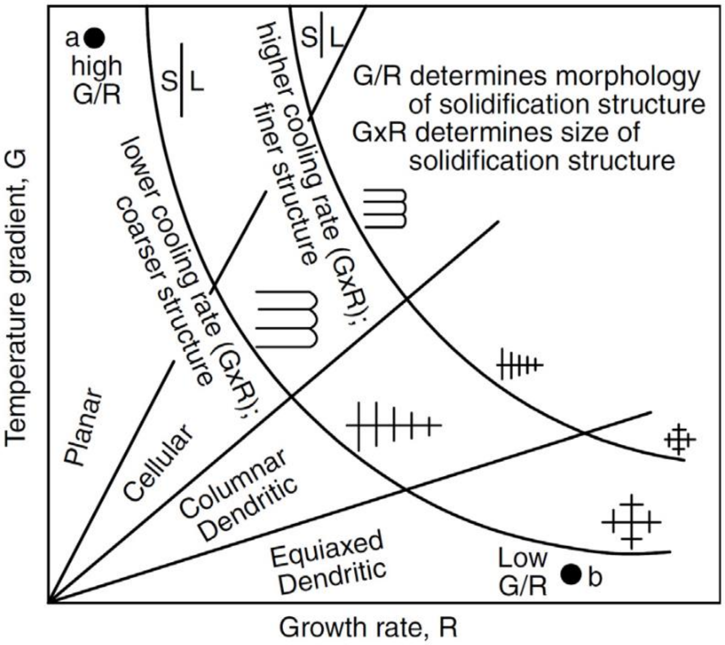

Figure 1.3: *The correlation between thermal conditions, specifically temperature gradient G and growth rate R, and resultant solidification microstructures including grain morphology and size [18].*

As suggested by Fig. 1.3, the G/R and G×R indicate the L/S-interface stability and cooling rate, which dominate the grain morphology and size, respectively. Due to the relatively lower cooling rate compared to other powder-based AM techniques, wire-laser DED generally produces large columnar grains in as-printed components. Specifically, grains tend to grow along the maximum heat flow direction at the solidification front during the solidification process. As a result, the growth direction is typically perpendicular to the local L/S interface. However, the morphology of the mushy zone and rear melt-pool boundary is generally complex, leading to varied solidification behavior in local regions and, subsequently, intrinsic microstructure heterogeneity in the as-printed samples. In addition, for face-centered cubic (FCC) and body-centered cubic (BCC) metals, <100>

is the preferred crystal growth direction. Therefore, a significant crystallographic texture forms accompanied by the generation of coarse columnar grains. Furthermore, element segregation, heterogeneous nucleation, and epitaxial growth are common features in the DED and other AM samples.

As a result of the layer-by-layer printing process, repeated heating provides an intrinsic heat treatment for the preceding layers [19]. Figure 1.4 displays the representative temperature history of the bottom region of a printed sample during the entire layer-by-layer DED process. This intrinsic heat treatment involves cyclic temperature fluctuations and is location-dependent. Subsequent thermal cycling imposes an annealing treatment for the previously deposited layers, possibly inducing microstructure evolution, such as the precipitation of secondary phases. Furthermore, the reheating effect contributes to the accumulation of thermal stress. Significant residual stress leads to part distortion and delamination, which are detrimental to the printing process and the performance of as-fabricated components.

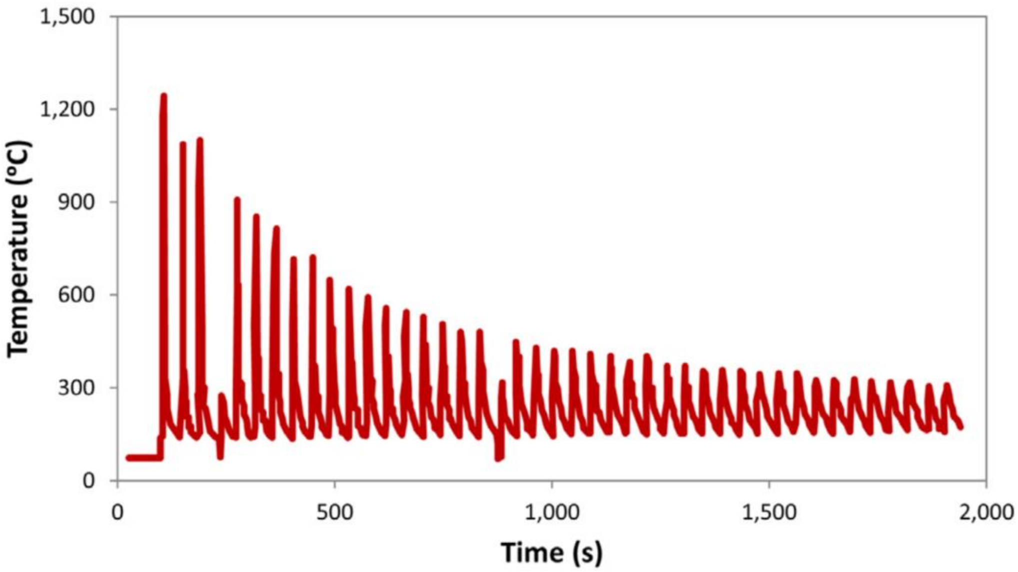

Figure 1.4: *A representative temperature cycling during the layer-by-layer DED of H13 tool steel [15]*

1.4 Microstructure of Inconel 718 and 316L stainless steel

Inconel 718 alloy and 316L stainless steel (SS) are common and commercially available wire feedstocks for wire-based AM due to their excellent printability and wide application in fabricating engineering components. The nominal composition of these two alloys is listed in Table 1.1. Inconel 718 is a nickel-based superalloy with many applications requiring high strength at elevated temperatures. This material also exhibits excellent tensile and impact strength, along with good oxidation and corrosion resistance, making it an ideal material for fabricating structural parts, particularly in the aerospace industry. However, Inconel 718 has poor workability and is challenging to manufacture by conventional methods due to its low thermal conductivity and limited material removal rate. Metal AM, characterized by near-net shaping, opens a new opportunity to manufacture Inconel 718 components. The microstructure of Inconel 718 comprises a complex phase configuration, including the FCC matrix phase (γ), carbides, and various intermetallic phases. Figure 1.5 is a classic Scheil solidification plot of Inconel 718 calculated using the *Thermo-calc* Software package [20]. This plot indicates the possible phases in Inconel 718 and their evolution during non-equilibrium solidification. The crystal structures of these potential solid phases at room temperature are summarized in Table 1.2 [21–23]. It should be noted that the Sigma phase is less likely to form in the metal AM process because solidifying the Sigma phase requires a lower cooling rate [24]. As suggested by the Scheil solidification plot, MC carbide phases, typically referring to the NbC carbide, have a high melting temperature close to that of the matrix phase. Laves phase is a topologically close-packed phase and typically detrimental to the mechanical properties of Inconel 718 [25]. This is because, on the one hand, the formation of Laves phase consumes the principal elements needed for precipitation strengthening. Metastable γ' and γ'' are two primary strengthening precipitates in Inconel 718, achievable through post-treatment. On the other hand, Laves phase tends to form a chained or networked geometry, which is susceptible to crack initiation and propagation during mechanical loading. For the AM processes of Inconel 718, element segregation, particularly Nb and Mo, is also a common feature in the as-printed sample, which also leads to the heterogeneous distribution of secondary phases. Given the complex phase configuration and its significant effects on the macroscopic performance of AM products, many efforts have been made to explore practical approaches for better microstructure control in the AM of Inconel 718 alloy. These approaches include adopting special printing strategies [26] and applying extra printing accessories [27].

Table 1.1: *The composition of 316L SS and Inconel 718 alloy in weight percentage.*

Elements	316L SS	Inconel 718
Cr	16-18	17-21
Ni	10-14	50-55
Mo	2-3	2.8-3.3
C	0.03 max	0.08 max
Mn	2	0.35 max
P	0.045	0.015 max
S	0.03	0.015 max
Si	0.75	0.035 max
N	0.1	-
Fe	Balance	Balance
Nb + Ta	-	4.75-5.5
Ti	-	0.65-1.15
Al	-	0.2-0.8
Co	-	1.0 max

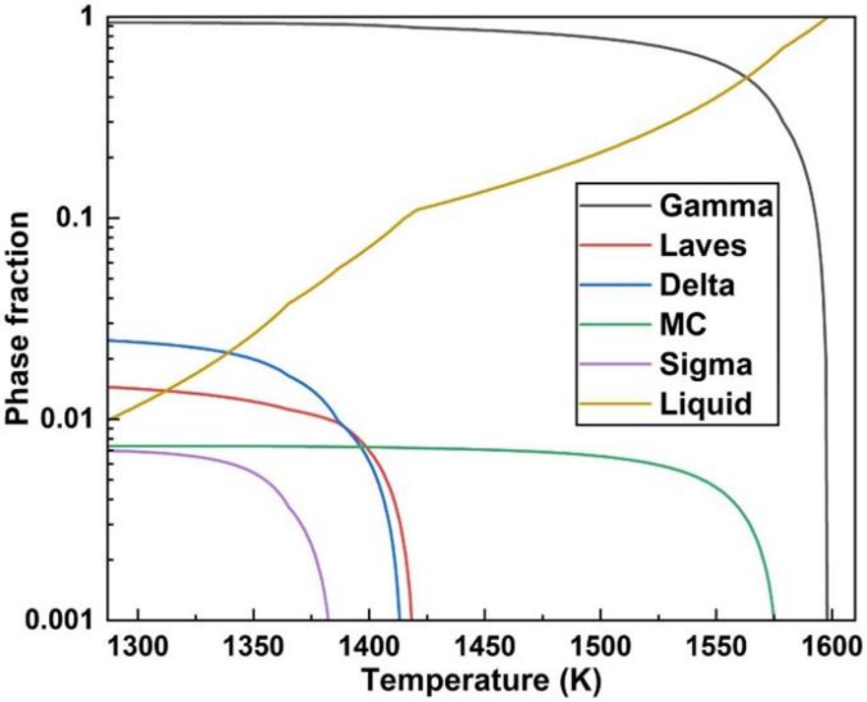

Figure 1.5*: The classic Scheil solidification plot for the non-equilibrium solidification of Inconel 718 alloy. This plot was calculated by using the classic Scheil model in the Thermo-calc Software package [20]. Databases of TCNI9: Ni-alloys v9.1 and MOBNI5: Ni-Alloys Mobility v5.1 were employed to calculate the phase fraction during solidification with a temperature step of 1 K. Two major assumptions were made: (i) the kinetics of atomic diffusion is infinitely fast in liquid but forbidden in solid, and (ii) the solidification interface is in thermodynamic equilibrium. However, the current model cannot explain additional kinetics phenomena within the present study.*

Table 1.2: *Crystal structures of solid phases in Inconel 718 alloy at room temperature* [21–23]. *The lattice parameters and space group of possible solid phases in Inconel 718 at room temperature are summarized.*

Phase	**Lattice parameters**	**Space group**
Gamma	a = 0.3598 nm	Fm-3m
Laves	a = 0.5150 nm, c = 0.8480 nm	$P6_3/mmc$
Delta	a = 0.5100 nm, b = 0.4226 nm, c = 0.4504 nm	Pmmn
MC-carbide	a = 0.4435 nm	Fm-3m
Sigma	a = b = 0.8800 nm, c = 0.4560 nm	$P4_2/mnm$

Commercial 316L SS wire is another common and easily accessible feedstock for wire-based AM processes. This material is not only economical but also characterized by superb ductility, excellent corrosion resistance, and acceptable strength. Hence, 316L SS has a wide application in marine industries, architectural fields, and fabricating nuclear reactors. In addition, the excellent biocompatibility of this material further expanded its impact on fields directly connected with our daily lives, including the manufacturing of medical devices, pharmaceutical equipment, and food containers. Commercial 316L SS is a representative austenitic steel, mainly consisting of an austenite (γ) matrix with an FCC structure and minor ferrite (δ) with a BCC structure. The ferrite phase typically exhibits a reticular morphology within the austenite matrix of DED-processed 316L SS samples. For austenitic steels, there is an allotropic transformation between austenite and ferrite phases with temperature variation. The ferrite phase is thermodynamically favored at elevated temperatures. Composition also plays a critical role in the phase content of the as-solidified sample and the solidification process, as shown by the conventional Schaeffler's diagram and austenitic steel solidification diagram [28,29]. The 316L SS consists of ~10% ferrite under equilibrium conditions. The solidification sequence of 316L SS in DED and wire-arc AM mainly follows the Ferritic-Austenitic mode [30,31], i.e., the FA mode sketched in Fig. 1.6b. In this mode, solidification initiates with the generation of the primary ferrite phase, associated with the reaction Liquid (L) → δ. At the dendritic/cellular boundaries of ferritic grains, the γ phase forms through the peritectic reaction L + δ → γ. After solidification, rapid cooling drives the solid-state phase transformation from primary ferrite to austenite. Therefore, the austenite constitutes the matrix of the DED-processed 316L SS samples; however, the remaining ferrite shows reticular morphology and is distributed within the austenite matrix.

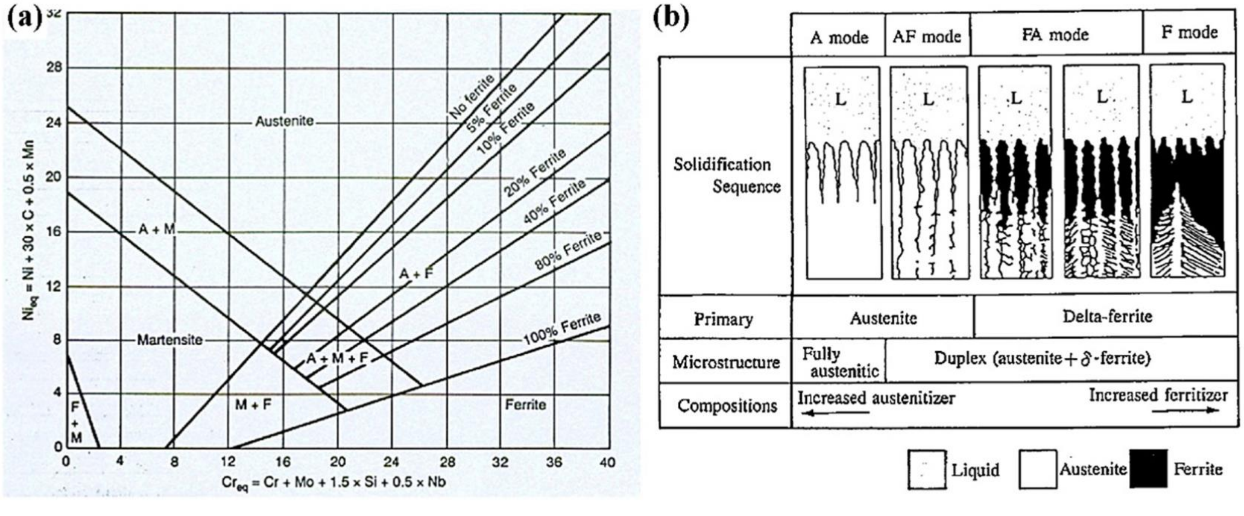

***Figure 1.6**: (a) The conventional Schaeffler's diagram showing the effect of composition on the phase content of steels under the equilibrium solidification condition. (b) The austenitic steel solidification diagram illustrating various solidification sequences [28,29].*

1.5 Crystallographic texture of DED samples

As explained in Chapter 1.3, large columnar grains are widely distributed in components fabricated by wire-laser DED because of the relatively lower cooling rate during solidification. As sketched in Fig. 1.7, the coarse columnar/dendritic grains grow along the maximum heat flow inside the melt pool. Furthermore, grain growth tends to take place along the specific crystal orientation of materials, and the favorable growth orientation is <100> for materials with a cubic structure. The directional growth of these large columnar grains and the preferred crystal growth direction result in strong crystallographic texture [32]. Consequently, coarse columnar/dendritic grains with a significant crystallographic texture are common features of DED-processed samples.

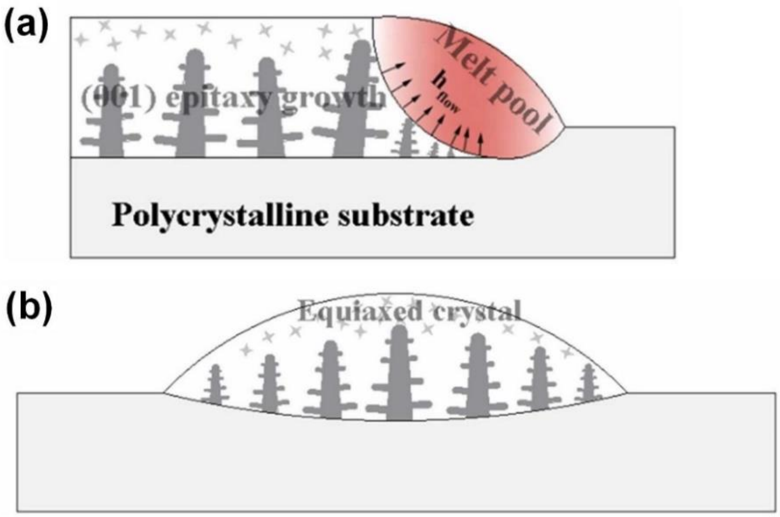

Figure 1.7*: Schematic diagrams showing the grain growth in the melt pool [33]. Figures (a) and (b) represent the central longitudinal section and the transverse section, respectively.*

The crystallographic texture is an important concern in metal AM owing to its significant effect on the mechanical anisotropy of the printed components. For many structural applications, isotropic mechanical properties of a DED material are desired, as they make it easier to predict how the material will behave under different types of loads and allow for a more efficient use of the material. Nevertheless, due to the complex physical events in the printing process, microstructure heterogeneity, coupled with crystallographic texture, inherently introduces significant anisotropy to AM components. For example, the lack of perfect bonding between layers results in distinct mechanical properties for DED samples when loaded horizontally and vertically [34]. Moreover, the residual stress, printing defects, and directional grain morphology also contribute to the anisotropy in the mechanical properties of DED components [35]. Nevertheless, controlling texture provides an additional possibility to counterbalance the anisotropy resulting from other factors and to produce components with superior properties. Furthermore, another novel application of texture control has been developed to encode data into metal parts. Sofinowski et al. recently integrated a linear barcode and a Quick Response code on a 316L SS substrate by varying the crystallographic texture spatially in LPBF [36]. Thus, the precise control of the crystallographic texture is of great importance for improving the performance of AM products and expanding applications of metal AM.

Texture control in laser AM can be achieved in two ways. One group of approaches involves introducing additional factors or processing steps, such as applying magnetic fields during printing [37], employing hybrid deposition processes [38], adding nucleation agents in the melt pool [39], and carrying out post-heat-treatments for as-deposited samples [40,41]. The magnetic-field-assisted AM typically uses a static electromagnet apparatus to generate a steady transverse magnetic field during printing. Thus, the favorable growth direction of crystals is constrained by both the heat flux and magnetic fields, consequently varying the crystallographic texture of as-printed samples. The metal AM hybridized with in-situ layer-wise deformation processing, such as in-situ ultrasonic impact peening, was also developed to control the microstructure of as-printed samples. In the hybrid manufacturing process, impact loading can be applied to each layer after printing, preventing the epitaxial growth of columnar grains and forming finer equiaxed grains through both plastic deformation and intrinsic recrystallization. Moreover, adding refractory powders is another practical approach to yield more random crystallographic textures. The remaining particles inside the melt pool can promote the nucleation rate during solidification, thereby suppressing the generation of strong crystallographic textures induced by grain growth. In addition, performing post-treatments is a common procedure to improve the quality of as-printed components, especially in industrial production. Hot isostatic pressing is a standard industrial practice that imposes both high temperature and isostatic pressure on printed samples. This approach can reduce the porosity and induce recrystallization while keeping the original shape of the as-printed products.

Except for adopting additional accessories or procedures mentioned above, a more straightforward approach to texture control involves directly altering laser conditions and deposition strategies across layers [42–46]. The essence of this approach is to vary the thermal condition in the melt pool, thereby interrupting the continuous epitaxial growth of columnar grains along the build direction. Adjusting the printing parameters allows the alternation of the melt pool morphology, particularly during the transition from conduction mode to keyhole mode in LPBF.

As illustrated in Fig. 1.8, the thermal conditions within the melt pool are correlated to the melt pool morphology. At greater melt-pool depths, the primary heat flow is horizontally distributed, indicated by red arrows. Thus, grain growth initiates at the lateral side of the melt pool and grows horizontally toward the center. In the case of a shallow melt pool resulting from low energy input, the preferred direction of grain growth is from the bottom toward the upper melt pool, consequently leading to distinct grain morphologies and crystallographic textures. Based on this theory, layer-wise texture control has been developed through the epitaxial growth between adjacent tracks or following layers. As shown in Fig. 1.9, alternating the scanning direction between layers can generate a specific texture based on the geometric conditions of epitaxial grain growth between layers. In comparison, these methods based on printing strategies are more economical and practical because no additional accessories or extra procedures are required. However, such approaches are more difficult to manipulate, especially for wire-based AM processes. The primary reason is that, despite the wide variation range of melt pool morphology in LPBF, the wire-based AM processes generally yield a shallow melt pool, challenging the flexible control of crystallographic textures through melt-pool morphology. In addition, texture control by only changing the printing parameters is likely accompanied by significant modification of solidification microstructures, such as grain morphologies, residual stress, and printing defects, which may have a complicated influence on the mechanical properties of AM products. For the above reasons, developing novel methods to achieve more flexible texture control is still desirable for further developing metal AM.

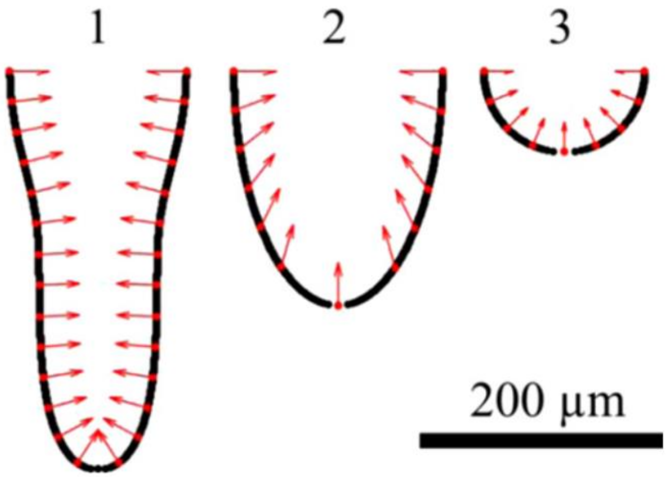

Figure 1.8: *Schematic illustrations displaying the transverse section of melt pools with different geometries [47]. Red arrows mark the local heat flow corresponding to each melt pool.*

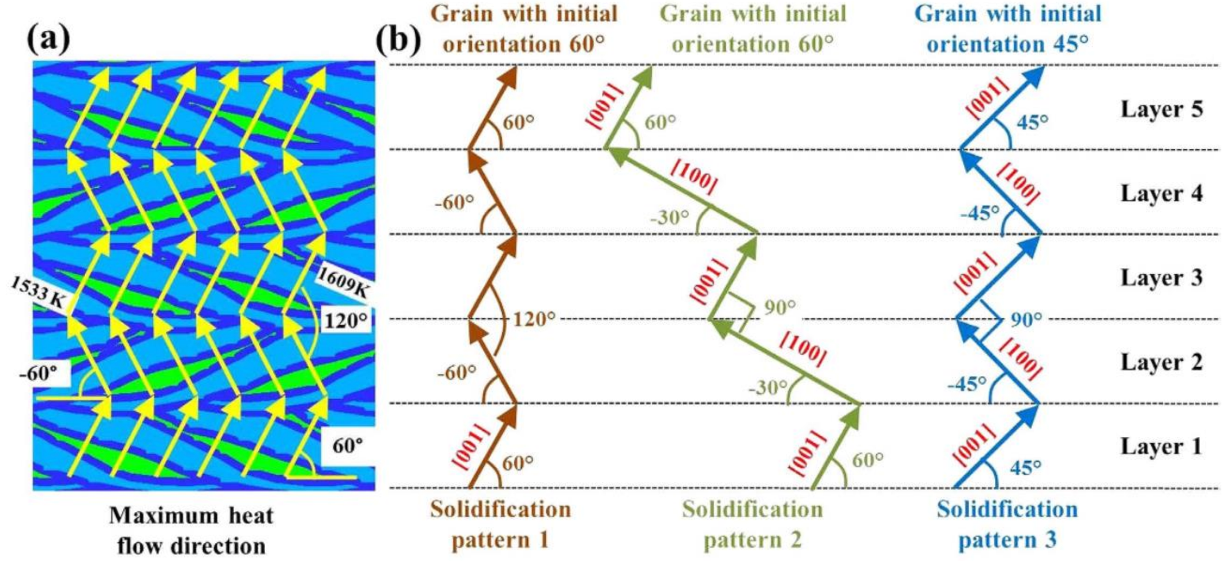

Figure 1.9: *Schematic illustrations showing the epitaxial growth between adjacent layers [43]. (a) The computed temperature field and the preferable growth direction (marked by yellow arrows). (b) Epitaxial growth patterns of grains with different orientations. The scanning directions between layers are reversed. The macroscopic texture depends on the geometry of epitaxial growth of grains*

between layers.

1.6 "Abnormal" columnar-to-equiaxed transition (CET) in metal AM

Producing metallic materials with finer grain structures is desirable for many engineering applications. Promoting columnar-to-equiaxed transition (CET) is still one of the most active research areas in metal AM. CET in metal AM generally results from the promoted nucleation rate induced by varying thermal conditions during solidification [48–50]. As illustrated by the solidification map shown in Fig. 1.3, the grain size and morphology strongly depend on G and R within the melt pool. A fast cooling rate suppresses the formation of columnar grains but promotes grain refinement. Therefore, directly adjusting the printing parameters, such as increasing scanning speed, can induce CET. However, it is intrinsically challenging for the wire-laser DED process because of the inherently low G×R value compared to LPBF. Moreover, as explained in Chapter 1.3, the available printing conditions are subject to a specific processing window. In addition to the normal CET based on the thermal conditions of solidification, adding nucleation agents [51] and performing post-treatment [52] are alternative methods employed in AM for refining microstructures. However, an "abnormal" CET based on nonclassical nucleation theory was reported recently and received much attention from the AM community [53–55].

The "abnormal" CET refers to the formation of small and equiaxial grains in local regions of as-printed samples in which only coarse columnar grains are supposed to generate according to the solidification map. According to the present theory, this phenomenon was attributed to the formation of icosahedral short-range ordering (ISRO) in undercooled liquid metal during solidification. In 2013, Kurtuldu *et al.* [56] discovered that the nucleation of the icosahedral solid cluster $Al_{45}Cr_7$ may significantly influence the solidification behavior of Al alloy. By adding trace amounts of Cr (ppm level) to the melt of an Al-Zn alloy, the sample surprisingly formed a large number of refined grains after solidification. In addition, a five-fold twinned crystallographic relationship was observed among several neighboring grains. The underlying mechanisms, incorporating the nonclassical nucleation theory, will be elaborated on in the next chapter. Briefly, they believed that the presence of icosahedral atomic orderings or metastable icosahedral solid clusters ($Al_{45}Cr_7$ phase here) in liquid metals can suppress grain growth but facilitate grain nucleation by providing additional nucleation sites.

Recently, Bambach *et al.* [10] and Cazic *et al.* [55], at about the same time, observed "abnormal" grain refinement in the coaxial wire laser DED process of the commercial Inconel 718 alloy, as shown in Fig. 1.10. Interestingly, in the printed bulk sample, the tiny equiaxed grains only appeared at certain regions of each melted track. Bambach *et al.* utilized three DED approaches, i.e., powder, cold-wire, and hot-wire DED techniques, to print Inconel 718 bulk samples. Surprisingly, the refined grains were only observed in the hot-wire DED sample. The hot-wire and cold-wire DED refer to either preheating the wire or not. The hot-wire function requires less laser power to melt the wire feedstock. Thus, the authors believed that the wire was not fully melted throughout the deposition process owing to the lower energy input and that recrystallization occurred in the unmelted wire, thereby leading to local grain refinement. However, Cazic *et al.* characterized the grain refinement region using electron back-scattered diffraction (EBSD) to analyze the orientation relationships among several neighboring grains. The five-fold symmetry and a mass of twinning boundaries were observed among these grains. In addition, the grain refinement region in each deposition track was close to the bottom fusion boundary, as shown in Figs. 1.10b and 1.10c. Thus, they believed that ISRO-mediated solidification happened in the DED process, analogous to Kurtuldu's finding in the casting of Al-Zn-Cr alloys, but the generation of ISRO was attributed to the insufficient remelting of the preceding layer rather than the alloy composition.

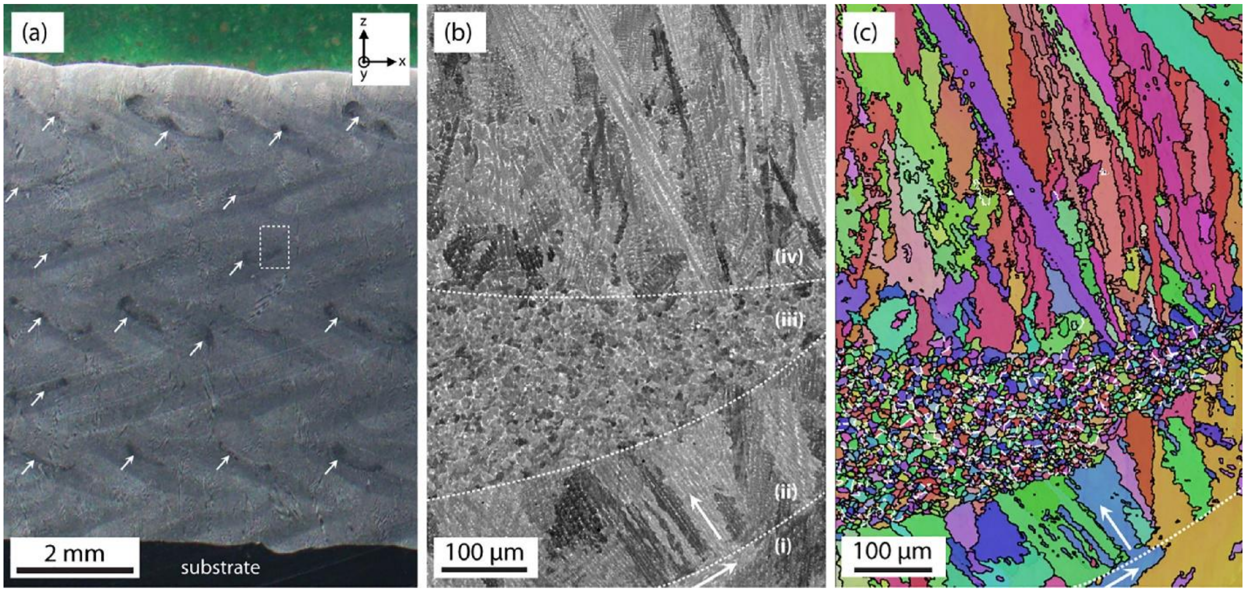

Figure 1.10: *The "abnormal" CET in the Inconel 718 sample fabricated by wire-laser DED [55]. (a) The optical image showing the cross-section of the as-deposited Inconel 718 sample. (b)The SEM image and (c) corresponding EBSD map of a local region marked in (a). The white arrows in (a) indicate the "abnormal" CET regions. The white grain boundaries in (c) represent the twinning relationship between the neighboring grains.*

Following these two cases about the wire DED of Inconel 718 alloy, a few other research teams claimed that the ISRO-involved solidification is also available in the LPBF process even for other FCC metals, such as Al alloys [57,58], 316L stainless steel [59], and commercially pure Ni [60]. The ISRO-involved solidification is igniting a growing interest in the metal AM field. The relevant investigations were conducted primarily through the post-characterization of the "abnormal" CET region. According to the observation of transmission electron microscopy, Buttard *et al.* [57,58] hypothesized three mechanisms that could be responsible for the "abnormal" CET in the LPBF of an Al-Mn-Ni-Cu-Zr alloy: the epitaxial nucleation on the $L1_2$-Al_3Zr primary phase, epitaxial nucleation on the complex $Al_{60}Mn_{11}Ni_4$ phase, and ISRO-mediated nucleation. Monier *et al.* [59] performed LPBF using two batches of 316L SS powders produced by different manufacturers. It was found that one batch of powder led to finer grains and more twinning boundaries than another, though the finer grains still present columnar morphologies. They attributed this phenomenon to the lower content of N and C in the former feedstock, based on the knowledge that N and C have adverse effects on forming ISRO in undercooled Fe and Ni liquid. A similar microstructure was observed in the LPBF of pure Ni powders, as reported by Galera-Rueda *et al.* [60]. There were no secondary phases observed in the as-printed sample. Thus, they stated that the "abnormal" grain refinement and twinning boundaries result from the metastable icosahedral quasicrystals that only exist in the undercooled liquid. Recently, Cazic *et al.* [61] reported their continuing research about the "abnormal" CET in wire-laser DED of Inconel 718. By using 3D EBSD and energy-dispersive spectroscopy (EDS), a TiC particle was characterized around the five-fold symmetry axis of equiaxed grains in the "abnormal" CET region. Therefore, they believed that the refractory TiC particle was surrounded by local Nb-rich liquid in the melt pool, leading to a high concentration of icosahedral cluster around and, consequently, inducing the ISRO-mediated solidification.

There is no doubt that the above investigations provided valuable insights into the "abnormal" CET of metal AM. Their recent emergence further highlighted the significance of this topic to metal AM. However, it also needs to be admitted that most of the existing explanations are still based on several hypotheses. Given the complex solidification behavior involved in metal AM, it is not convincing enough to reveal the underlying mechanisms solely based on post-characterization. For example, the secondary phases observed around the five-fold symmetry axis of equiaxed grains might form due to the element segregation in the later solidification process after the matrix grains had been solidified. In this case, these secondary phases did not contribute to the "abnormal" CET.

1.7 Development of non-classic nucleation theory

As explained in Chapter 1.3, rapid solidification is one of the most critical physical events in wire-laser DED and other relevant metal AM processes. Solidification behavior is directly responsible for the microstructure of as-printed components, consequently determining the performance of final products. The crystallographic texture and "abnormal" CET introduced in two previous subchapters are pertinent to two competing solidification behaviors, i.e., columnar grain growth and grain nucleation. In metal AM, the printing conditions and characteristics of materials play critical roles in the solidification process. As mentioned in Chapter 1.3, efforts are underway to quantify the relationship between thermal conditions and solidification microstructures. Similar to Fig. 1.3, solidification maps have been built for different materials to describe the competence between forming refined equiaxed grains and coarse columnar grains. With the incorporation of phase-filed simulation and multi-physics modeling [62], the microstructures of as-printed samples can be directly simulated. However, these models applied for AM rely on many variables that need to be further calibrated through experiments, which weakens their potential in predicting the solidification process of AM. One primary reason is the lack of a deeper understanding of the solidification mechanisms under AM conditions. The advent of AM techniques has profoundly impacted classic solidification theory due to the involvement of various elements in the solidification process, including the rapid melting of feedstocks, drastic melt flow, and complex thermal conditions. In addition to the benefits of building more reliable models, more comprehensive knowledge is also conducive to the flexible microstructure control in AM. Therefore, the rapid development of metal AM technologies requires a deeper understanding of the corresponding solidification fundamentals.

The traditional recognition of solidification was built based on the classic nucleation theory (CNT). In this theory, the solidification of crystals is assumed to be the phase transformation from disordered liquid to ordered solid. With a certain supercooling, the structural fluctuation of the disordered liquid leads to the generation of atomic nuclei. Atomic nuclei larger than the minimum viable nucleus size, also referred to as the critical nucleus size, are energetically favorable. These stable nuclei can continue to grow through the diffusion of free atoms from the disordered liquid phase to the surface of these nuclei. While many equations have been derived to quantify the solidification process based on the CNT, such predictions are sometimes less valid in the rapid solidification of metal AM. This is because the CNT process ignores the presence of structural orders in the liquid. Rather than fully disordered, atoms in liquid, especially undercooled liquid, are ordered in a short range. Note that the ordered structure of liquid is more random, dynamic, and distorted compared to an atomic cluster in the solid state. Solidification in metal AM processes is subject to fast cooling, resulting in a large undercooling of liquid. For alloys with complex compositions, some solute elements can even induce local covalent bonding, thereby promoting more stable atomic orders in liquid metals. Several structural orders with FCC-like, hexagonal-close-packed-like (HCP-like), and icosahedral-like symmetries have been discovered in liquid metals and investigated by multiple methods, including first-principle calculations [63], molecular dynamics simulations [54,64], atomic electron tomography [65], elastic neutron scattering [66,67], and synchrotron techniques [68,69]. A large undercooling restricts the CNT process based on atomic diffusion, leading to alternative solidification mechanisms where preorders play a more critical role. As introduced in Chapter 1.6, it has been widely believed that the presence of icosahedral short-range ordering (ISRO) in undercooled liquid metal can result in an “abnormal” columnar-to-equiaxed transition (CET) during solidification, and this phenomenon is called ISRO-mediated solidification.

ISRO is a prevalent preorder in the liquid phase of FCC metals [53]. The principle of five-fold symmetrical ISRO in the undercooled liquid was first proposed by Frank in 1952 [70]. A schematic of the ISRO consisting of 13 atoms is shown in Fig. 1.11. This structure includes 20 distorted tetrahedra arranged around the fivefold symmetry axes, the axis linking opposite vertices. The central atom has 12 neighbors, similar to the close-packed structures with a coordination number of 12, such as FCC or HCP. The presence of ISRO is possible because this compact arrangement of 13 atoms reduces the energy (~8.4%) compared to the dense-packed FCC or HCP clusters consisting of the same number of atoms. Fifty years after Frank's hypothesis, Schenk *et al.* [69] and Kelton *et al.* [71] provided experimental evidence of icosahedral short-range order (ISRO) in both stable and deeply undercooled melts through neutron scattering and synchrotron x-ray scattering, respectively. The further development of characterization and simulation tools has facilitated the investigation of preordering in liquid metals and the evolution of preordering during solidification.

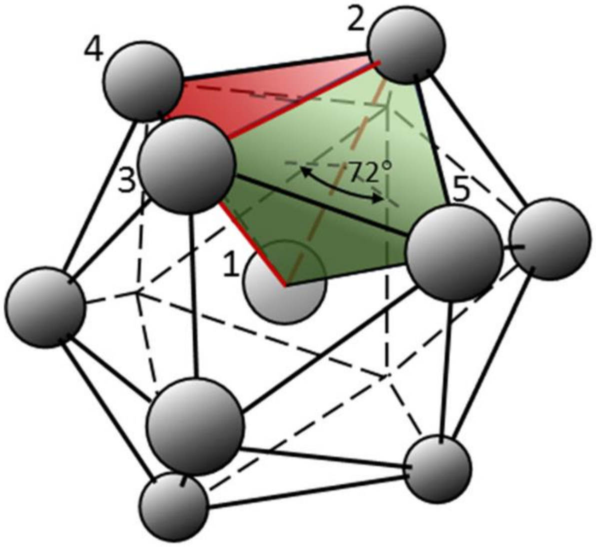

Figure 1.11*: A regular icosahedron constructed by 13 atoms [72]. The central atom and four atoms located on vertices are numbered from 1 to 5. Atoms 1-2-3-5 represents a tetrahedron in this icosahedron. This tetrahedron is slightly distorted compared to the {111} tetrahedra in FCC structures.*

ISRO can influence solidification behavior in several ways. According to the current theory [53], the presence of ISRO in undercooled melt significantly diminishes atomic mobility, restrains grain growth, and results in finer grains, as grain growth depends on atomic attachment at the solid-liquid interface. On the other hand, ISRO clusters provide additional nucleation templates during solidification. As illustrated in Fig. 1.11, ISRO consists of multiple tetrahedra with five-fold symmetry for rotations. These tetrahedra can evolve to the {111} tetrahedra of an FCC structure and lead to the heteroepitaxy growth of multiple twins [55,56]. As a consequence, several grains with specific twinning relationships form around the ISRO core. Additionally, the ISRO, consisting of 13 atoms, can undergo slight growth in the same manner—extending the FCC packing of the 20 distorted tetrahedra and forming additional layers of FCC shell, a phenomenon known as the Mackay growth mode [73]. With abundant twinning boundaries and the presence of five-fold symmetry among neighboring grains, the recent observation of the "abnormal" CET in metal AM was attributed to such an ISRO-mediated solidification.

1.8 Approaches to investigate printing processes and the advantages of o*perando* synchrotron x-ray characterizations.

1.8.1 Sensing methods

Directly characterizing or monitoring the metal AM process is essential for better understanding printing behaviors, including wire melting, melt-pool structure, and rapid solidification. Over the past decades, the AM and welding communities have employed various real-time sensing methods to monitor printing or welding processes. Optical imaging, either in visible light or infrared wavelength, is a representative vision sensor that provides direct and global observation of the printing behavior. Owing to excellent accessibility and strong practicability, this monitoring approach has been widely used to monitor the entire printing process, including melt pool initiation, stable printing period, and wire retreat after printing. During the stable printing process, melt-pool size and surface morphology can be directly measured, which delivers important information to design the printing profile. Most importantly, high-speed optical imaging can capture the generation of several printing defects, e.g., the "dripping" phenomenon induced by excessive energy input (Fig. 1.12). In addition, using infrared thermography and digital image correlation [74] makes it possible to visualize the temperature distribution and measure the evolution of thermal stress during printing. This information is highly significant in guiding processing optimization. However, it should be noted that optical imaging can only provide information about the sample surface and is not available to investigate the structure dynamics within the melt pool.

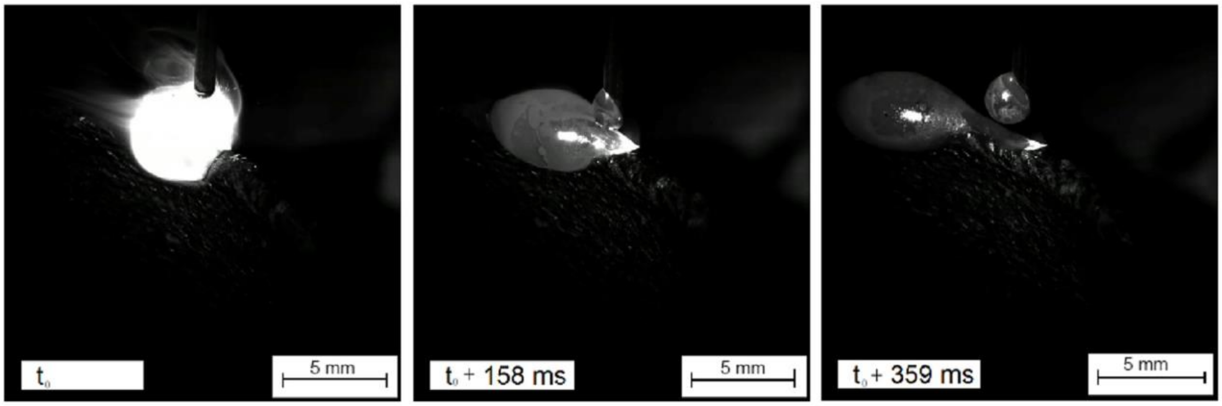

***Figure 1.12**: High-speed optical imaging of the "dripping" phenomenon in wire-laser DED*

induced by excessive energy input [75].

In addition to optical imaging, various sensing methods that monitor light, acoustic, and electric signals have been applied in AM and welding for diverse purposes, particularly for diagnosing the generation of printing defects and monitoring melt-pool dynamics. For instance, studies have reported that the generation of cracks during AM processes would release a specific acoustic signal [76]. By collecting acoustic emissions during the printing process, it becomes possible to evaluate the position of cracks and their propagation directions. The development of machine learning has greatly enhanced the potential of sensing methods in the field of real-time monitoring and diagnosis. However, these methods are less effective at revealing the underlying mechanisms involved in printing.

1.8.2 Multi-physics simulation

Phenomenological modeling is a powerful tool for investigating AM processes and predicting the outcome of AM production. By modeling the fundamental physics related to laser-matter interaction, thermal conduction, and mass transfer, numerical simulations can reveal the fluid dynamics, temperature distribution, and stress field in AM processes [77–79]. High-fidelity models can be used to elucidate the complex physics and reveal the underlying mechanisms involved in AM processes. With an enhanced understanding of the related physics and the advancement of computational capability, increasingly sophisticated models have been developed to investigate highly dynamic phenomena. These models have demonstrated their potential to solve long-standing confusion within the AM community. For instance, high-fidelity simulations were utilized to elucidate the mechanisms of defect generation during printing [80,81]. Moreover, by coupling other modules that account for phase transformation and mechanical deformation, an integrated model can simulate grain morphology and residual stress distribution in as-printed components.

Besides pursuing high-fidelity simulations, developing reliable yet more straightforward models has merit. Such numerical simulations are valuable for gaining unique insights into studying metal AM. For example, the simulation can calculate the three-dimensional temperature field during the printing process, but this information is challenging to measure by experiments directly. Numerical simulations have been employed to investigate the thermal fluid dynamics of the melt pool in the wire-laser DED, as illustrated in Fig. 1.13. However, the main challenges of utilizing numerical modeling remain in the absence of critical thermophysical parameters of feedstock materials, lack of standardization, and limited access.

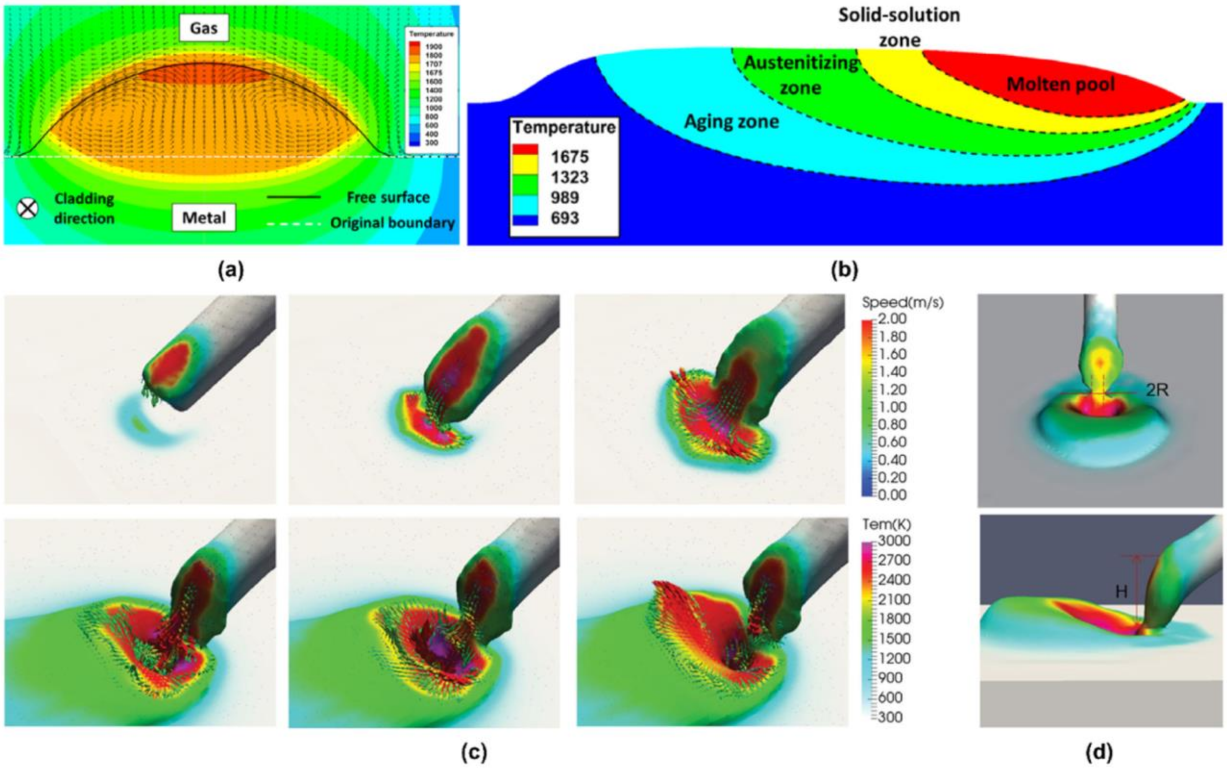

Figure 1.13*: The numerical simulation revealing the thermal fluid dynamics of the melt pool in wire-laser DED [8].*

1.8.3 Dynamic transmission electron microscopy

Advanced characterization technologies open new opportunities to study metal AM processes. So far, *in-situ* and *operando* characterization of AM has been developed based on electron microscopy, neutron techniques, and synchrotron x-ray techniques. Due to the high spatial resolution and fast capture rate, dynamic transmission electron microscopy (TEM) can be implemented to perform in-situ investigation. Mckeown *et al.* [82] investigated the rapid solidification of hypoeutectic Al-Cu and Al-Si thin films by integrating a pulse laser source into the microscope. The microstructure evolution during the rapid solidification can be monitored in microsecond timescales, as shown in Fig. 1.14. Accordingly, the solidification velocity can be measured via the movement of the liquid-solid interface. The investigation of pulsed-laser-induced rapid solidification provided valuable information for understanding the rapid solidification in metal AM processes; however, the sample thickness available for this characterization is limited to hundreds of nanometers. The current in-situ dynamic TEM investigation cannot accomplish the actual AM printing conditions.

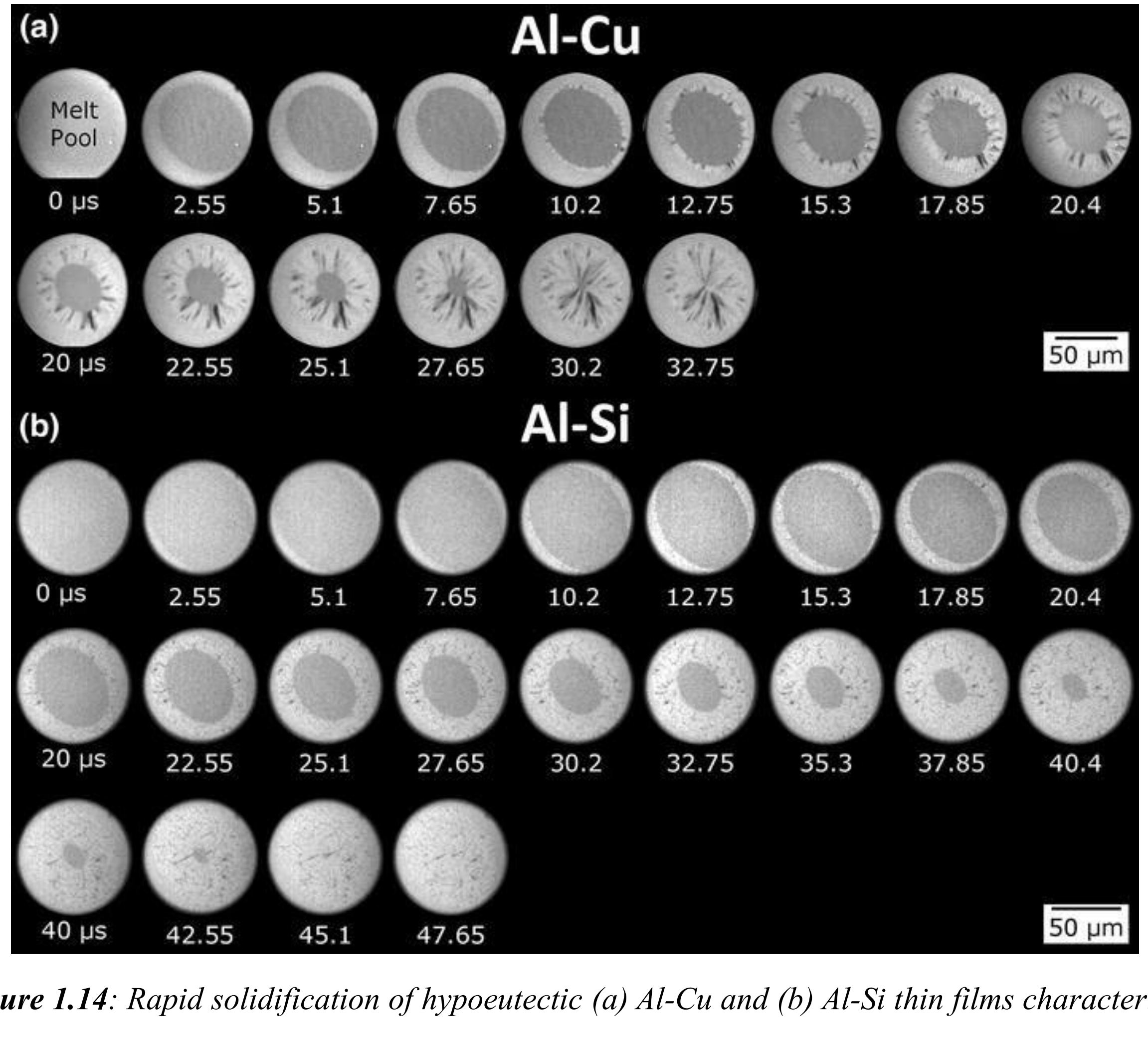

***Figure 1.14**: Rapid solidification of hypoeutectic (a) Al-Cu and (b) Al-Si thin films characterized by in-situ dynamic transmission electron microscopy [82].*

1.8.4 Neutron diffraction

Neutron and synchrotron facilities offer greater freedom to conduct *operando*/*in-situ* experiments for AM processes without the limitation of the small sample chamber in electron microscopes. Compact AM machines could even be placed in the beamline room for *operando* neutron/synchrotron characterization. Neutron scattering is desirable for studying high-deposition-rate AM processes, like wire-laser DED and wire arc additive manufacturing (WAAM). The primary reason is that neutrons have sufficient penetrative capability in thick metal samples. Plotkowski *et al.* [83] performed *operando* neutron diffraction experiments on steel using the WAAM process at the Vulcan beamline of Spallation Neutron Source in Oak Ridge National Laboratory. The *operando* neutron diffraction experiment revealed the effect of the thermal history on transient phase transformation and the evolution of lattice strain. The time-resolved *operando* measurements are displayed in Fig. 1.15. By probing the neutron beam at specific locations in the preceding layers, a series of 1D diffraction line profiles as a function of time can be obtained during the printing process. Simultaneously, multiple detectors are equipped in the Vulcan beamline to collect data from different directions. The time-resolved diffraction maps in Fig. 1.15 were generated by compiling a series of 1D diffraction line profiles. Compared to synchrotron x-rays and high-energy electron beams, the wavelength of the neutron beam is relatively long, which is favorable for more accurate measurements of the lattice strain. However, the relatively low flux of incident neutrons (compared to synchrotron x-ray) limits the temporal resolution of this *operando* characterization technique, consequently affecting its potential to investigate highly dynamic phenomena in AM processes. Additionally, the neutron beams used in such *operando* diffraction experiments typically have large dimensions (5 × 5 mm^2 in Fig. 1.15) to keep a high flux of incident neutrons and to satisfy the need to include a sufficient number of grains within the detection volume. Hence, the spatial resolution should also be a factor to consider in *operando* neutron diffraction experiments of AM.

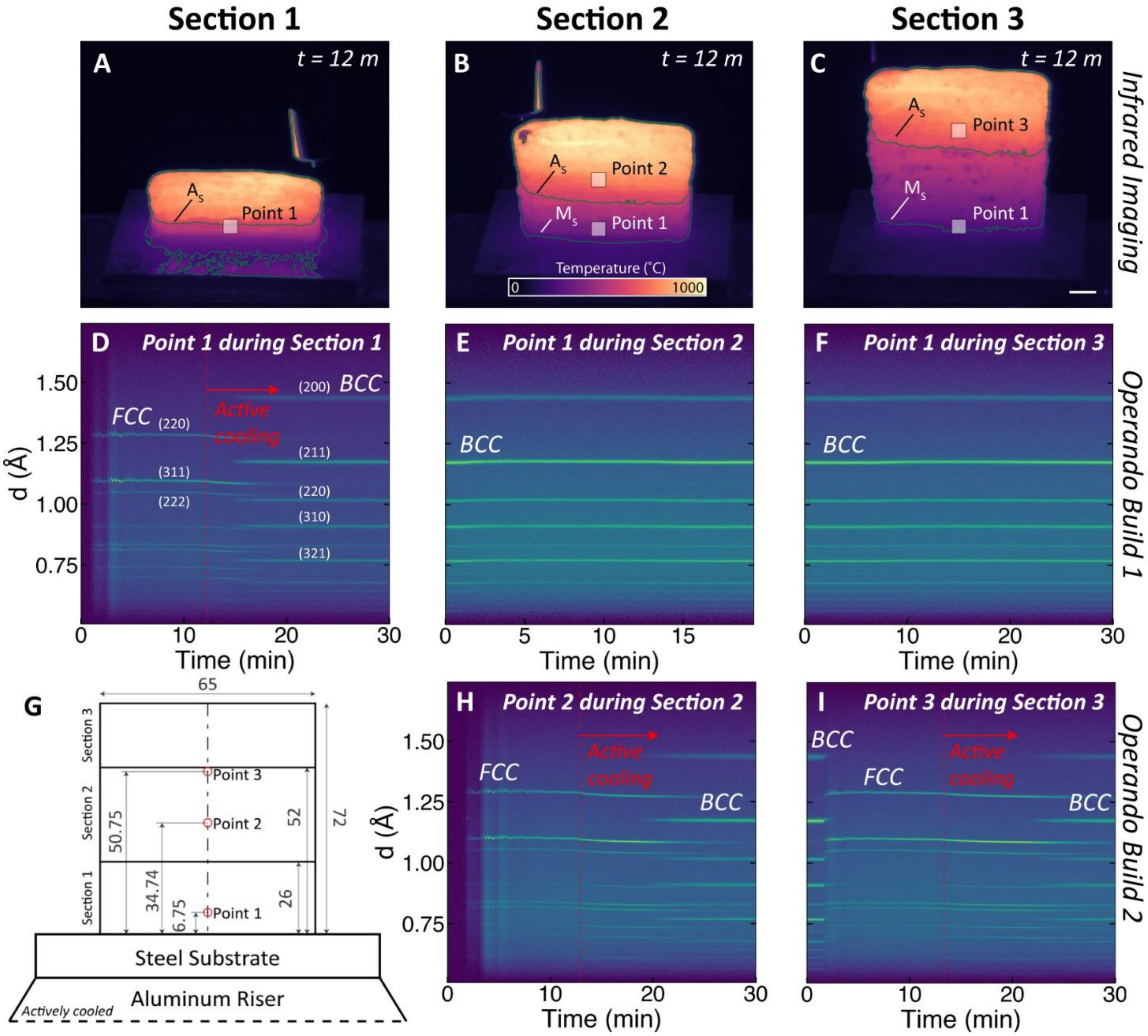

Figure 1.15: *The time-resolved operando measurements of operando neutron diffraction for the WAAM process [83]. (a-c) The temperature distribution of the build during printing was measured*

using infrared thermography. (d-f, h, i) The time-resolved diffraction maps showing the microstructure evolution at different locations of the build during printing. (g) A sketch showing the sample geometry and the location of neutron data collection.

1.8.5 Synchrotron x-ray techniques

Operando synchrotron x-ray techniques provide a unique set of tools for studying metal AM processes. The main advantage of hard x-ray techniques is that the high-energy x-rays can penetrate through a relatively thick build track of high-density materials to acquire information about the melt pool interior. Following the successful demonstration of *operando* synchrotron experiments for laser powder bed fusion (LPBF) [84], synchrotron x-ray imaging and diffraction have been widely adopted by the AM community to study highly dynamic phenomena, such as defects generation [81], powder dynamics [85], melt pool evolution [86], phase transformation [87], thermal stress accumulation [88], in various powder-based AM processes. In contrast, wire-based AM processes have garnered comparatively less attention. One reason could be that the melt pool of wire-based AM is typically large, resulting in a substantial attenuation of x-rays with energies less than 50 keV. Consequently, the density contrast for distinguishing different features in x-ray images is not readily discernible, and the diffraction signal is too weak to achieve adequate temporal resolution.

Elmer *et al.* [89] and Brown *et al.* [90] successfully applied the *in situ* synchrotron x-ray diffraction technique to investigate the solidification behavior of wire arc welding and wire arc AM processes, respectively. The former examined the kinetics of ferrite-to-gamma phase transformation in the 304 stainless steel during solidification and subsequent cooling of a stationary ‘spot’ weld. The latter implemented a substrate wheel to generate linear depositions of 304L stainless steel. The printing system also continuously moved horizontally with respect to the incident x-ray during the *operando* experiment. Therefore, the diffraction data reflecting the microstructure across the entire longitude melt pool was collected. This experimental configuration is sketched in Fig. 1.16. A high-energy x-ray (71 keV) was adopted in the measurement. The main advantage of adopting hard x-ray techniques is that high-energy x-rays can penetrate through a relatively thick build track of high-density materials to acquire information regarding the melt pool interior. The microstructural evolution during the solidification process, including phase fractions, crystallographic textures, and residual stresses, was measured. These two studies demonstrated the unique capability of the high-energy synchrotron x-ray diffraction technique for probing the wire-based AM process. Compared with the *operando* neutron diffraction shown in Fig. 1.15, the x-ray beam size used for *operando* diffraction is typically one order smaller than the neutron beam. Meanwhile, another apparent advantage of adopting high-energy synchrotron x-ray is the high flux of x-ray photons, which is required to investigate highly dynamic phenomena, e.g., the phase transformation kinetics during the rapid solidification of AM processes [87]. High-speed x-ray imaging also broadly impacts the AM community, even though it is mainly applied to the powder-based AM processes. This real-time monitoring technique enables fast characterization with a megahertz frame rate. Many fundamental insights have been gained from this high-speed perspective, greatly promoting the development of metal AM technologies.

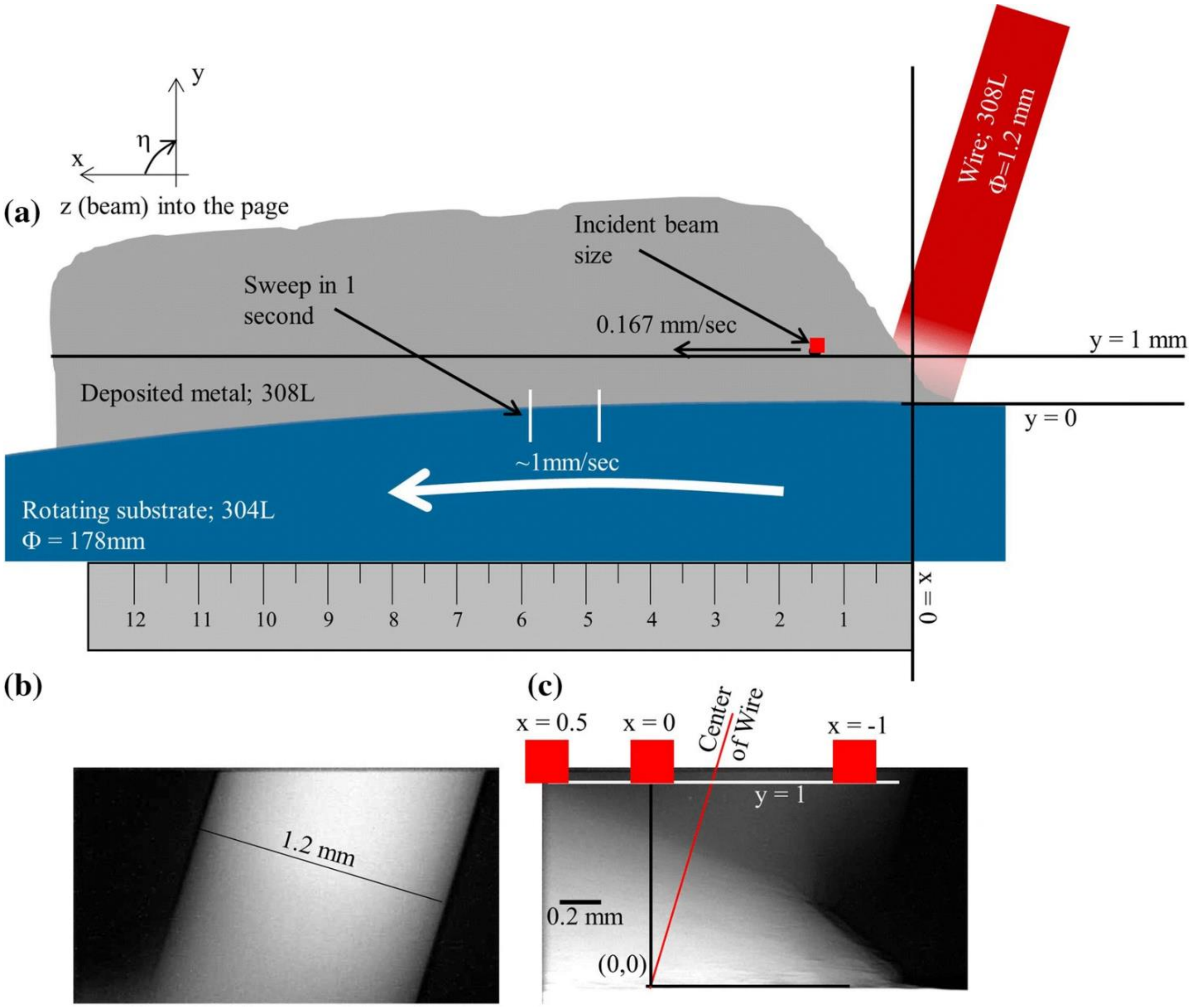

Figure 1.16: *(a) The sketch of operando high-energy x-ray diffraction of WAAM* [90]. *The linear deposition is formed on a rotating wheel substrate, and the position of the incident x-ray beam is marked by red squares. (b) and (c) are x-ray images showing the wire feedstock and melt pool front, respectively.*

1.9 Application of x-ray total scattering in solving atomic structure of liquid metals

The *operando* synchrotron x-ray techniques open new opportunities for investigating the structure of melt pool and rapid solidification under AM conditions, where pair distribution function (PDF) analysis is a desirable method to investigate the structure of amorphous materials including liquid metals. PDF analysis is essentially the Fourier analysis of the total-scattering data (*I(Q)*) that treats both Bragg diffraction and diffuse scattering on an equal basis. Bragg diffraction is primarily attributed to information regarding the perfect lattice, while diffuse scattering is mainly associated with lattice deviations. In liquid metals, the atomic positions are more random and dynamic, significantly contributing to the diffuse scattering of x-rays. The PDF profile has a physical meaning related to the probability of finding an atom at a certain distance from a reference atom, capable of providing statistical information about the liquid structure. The mathematical expression of PDF analysis, from *I(Q)* to *G(r)*, is shown as follows:

$$S(Q) = \frac{I(Q)}{\langle b \rangle^2} \qquad \text{eq. 1.4}$$

where Q, $S(Q)$, and $\langle b \rangle$, represent the wavevector, total-scattering structure function, and compositional average of scattering amplitude of atoms. It should be noted that the *I(Q)* here refers to the total-scattering intensity solely from the sample, which can be obtained via a background correction. The background correction refers to subtracting the background signals, such as the x-ray scattering from the sample container, by the as-collected intensity data. Then, the reduced pair distribution function, *G(r)*, can be readily calculated through the Fourier transformation of *S(Q)*.

$$G(r) = \left(\frac{2}{\pi}\right) \int_0^{\infty} Q[S(Q) - 1]\sin(Qr)dQ \qquad \text{eq. 1.5}$$

It should be noted that *G(r)* is only a correlation function of the pair distribution function, *g(r)*. They can convert into each other through the following equation:

$$G(r) = 4\pi r\rho_0[g(r) - 1] \qquad \text{eq. 1.6}$$

where ρ_0 is the atomic density. These two functions have similar physical meanings when interpreting the atomic distribution. However, *G(r)* is more commonly used owing to the calculation convenience and provides better presentation of data [91].

The development of the rapid acquisition PDF (RAPDF) method simplified the PDF measurement, opening new opportunities for studies on short timescales. This method typically implements a high-energy and monochromatic x-ray beam directly radiating on the sample. A large 2D area detector is required to be placed behind the sample and orthogonal to the incident x-ray beam. This method is particularly valuable in studying liquid metals because of the highly efficient measurement [68,71]. Figure 1.17 illustrates an example of applying RAPDF to solve the structure of supercooled liquids [92]. With the utilization of levitation, the containerless RAPDF was accomplished without contamination from the sample container. A laser was used to melt the sample, allowing studies of the solidification process. It is worth noting that the RAPDF provides the first experimental evidence about the five-fold symmetry of liquid metal and the existence of ISRO [71,93].

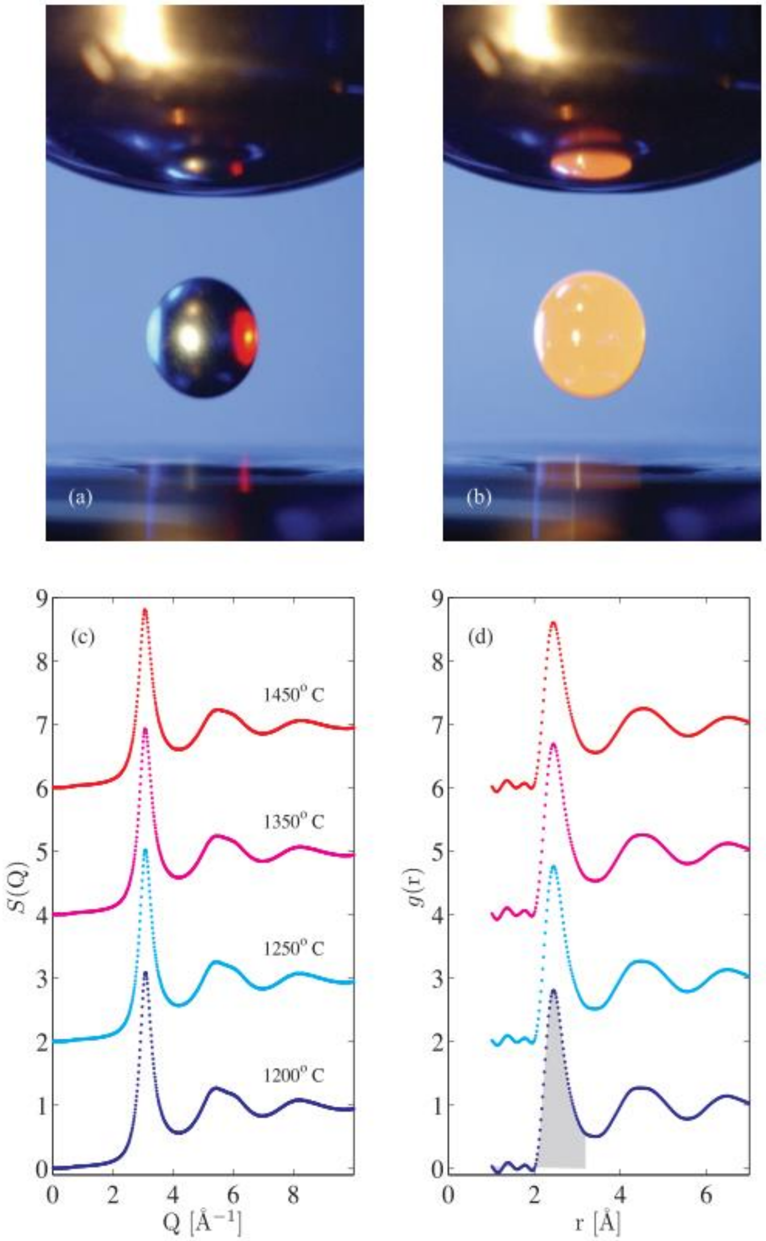

Figure 1.17*: X-ray scattering experiments for liquid metal [92]. The metallic sample is levitated electrostatically and melted by a laser source in an ultra-high vacuum chamber. The S(q) and g(r) can be measured for the supercooled liquid via the RAPDF method.*

1.10 Dissertation overview

This dissertation investigated the wire-laser DED process, particularly by employing *operando* synchrotron x-ray characterization and multi-physics simulation, to reveal the underlying mechanisms and provide novel insights for improving the control of solidification microstructures. Chapter 2 includes a detailed description of the methodologies applied in the research of this dissertation work, followed by three chapters about the detailed investigation. Chapter 3 comprehensively investigates wire-laser DED for Inconel 718 alloy under a specific energy input. This chapter also elaborates on the *operando* synchrotron x-ray characterization of wire-laser DED. In contrast to the focus on printing conditions, Chapter 4 introduces a novel deposition strategy that deliberately induces a certain degree of melt pool instability to control the crystallographic texture and mechanical anisotropy of the as-printed samples. Chapter 5 aims to provide a thorough investigation of the "abnormal" CET in metal AM. The utilization of *operando* synchrotron x-ray characterization is expected to yield direct experimental evidence to unravel the "abnormal" CET in metal AM. The final chapter (Chapter 6) summarizes the critical conclusions made in this dissertation and discusses continuing works and future efforts following the current research.

2. Materials and methods

2.1 Wire-laser DED processes

The printing processes in this dissertation were executed using two commercial DED systems: μPrinter (Additec, USA) and M450 (Meltio, Spain). The photographs of these two DED printers and their deposition heads are shown in Fig. 2.1. The principal components of the DED systems are noted in the photographs, but the external cooling system and gas system are not presented here. The μPrinter is a desktop DED printer, as shown in Fig. 2.1a, and has been modified for *operando* synchrotron x-ray characterization. Its printhead was equipped with three diode lasers arranged centrosymmetrically (Fig. 2.1c). Each laser has a ~1 mm diameter with a near-Gaussian profile at the focal plane. This printer was primarily used to print single-track deposits for fundamental investigations, such as *operando* synchrotron characterization. However, the productive fabrication of bulk samples was carried out using the M450 DED printer with six diode laser sources (Fig. 2.1b). Similar to the μPrinter, each laser beam equipped on M450 also shows a near-Gaussian energy distribution with ~1 mm diameter at the deposition plane. The laser power is evenly distributed over six laser beams. The maximum laser power available for the μPrinter and M450 are 600 W and 1200 W, respectively. During printing, commercial Inconel 718 or 316L wires with a 0.9 mm diameter (Harris, USA) were extruded straight down from the center of the printhead and deposited onto the substrate made of the same materials. Meanwhile, the deposition head was stationary, while the building platform was translated in both lateral and vertical directions. High-purity Ar was blown out of the printhead throughout the printing process as shielding gas.

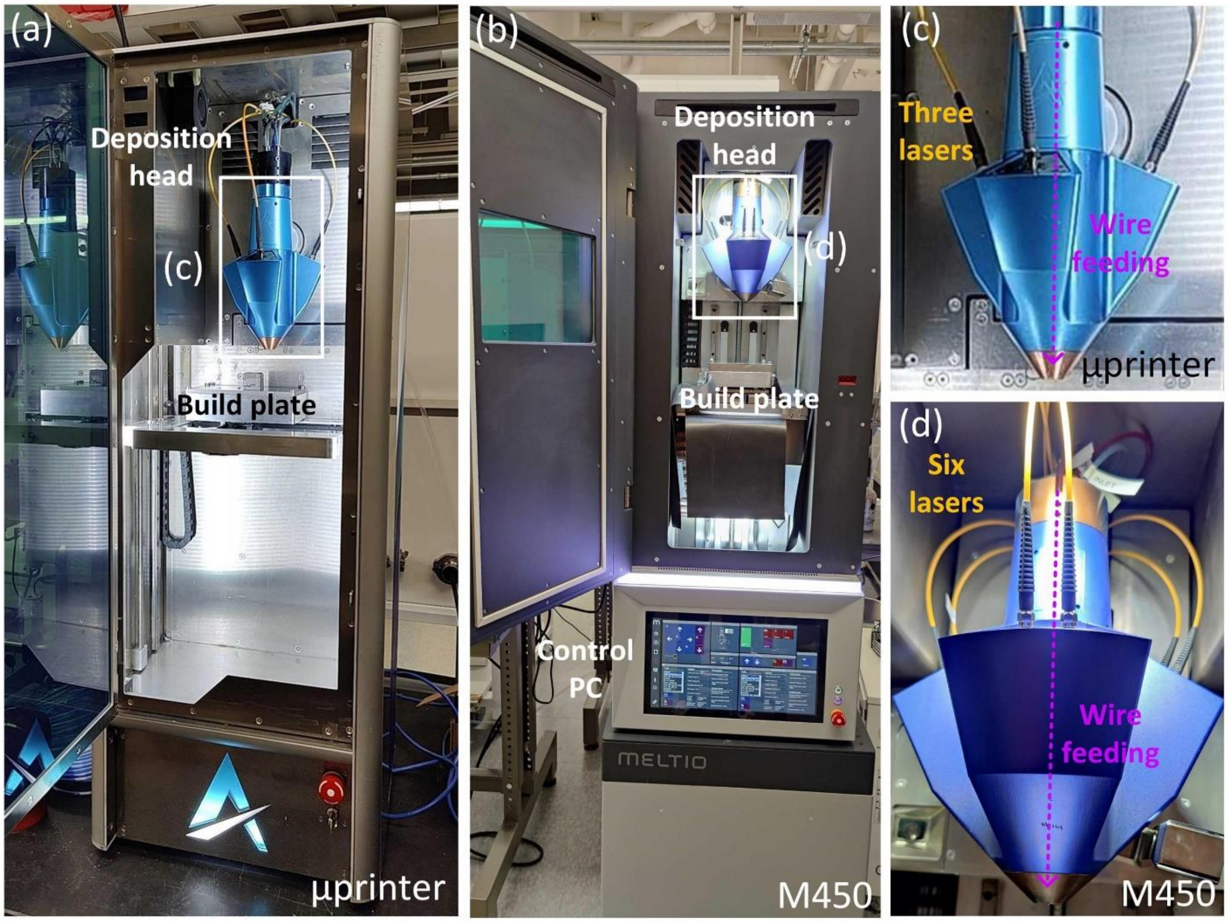

Figure 2.1: *Photographs of the two wire-laser DED systems used in this dissertation. (a) The Additech μprinter and (c) its deposition head equipped with three lasers. (b) The Meltio M450 DED printer and (d) its deposition head equipped with six lasers.*

2.2 Fundamentals of synchrotron x-ray and reasons for *operando* experiments at the 1-ID beamline of the Advanced Photon Source

Operando synchrotron x-ray characterization is an important method used in this work to investigate the printing process. X-rays are essentially electromagnetic waves with short wavelengths, typically in the 0.01 to 10 nanometers range. The energy of x-rays is correlated to their wavelengths and can be quantized into photons. Briefly, x-ray photons interact with matter in two ways: they are either scattered or absorbed by atoms. Since discovered by Wilhelm Conrad Röntgen in 1985, x-rays have become an essential source for microstructure characterization. According to the various characteristics of x-rays and their interaction with matter, many relevant techniques, such as x-ray diffraction, x-ray imaging, and x-ray fluorescence spectroscopy, have been developed for various applications. These techniques have enormously impacted many fields, including environmental monitoring, medicine, energy, scientific research, and security.

The development history of x-ray sources is shown in Fig. 2.2 [92]. So far, x-ray tubes and rotating anodes are still employed in commercial x-ray instruments as x-ray sources. For these lab-based x-ray sources, electrons are produced by a glowing filament and subsequently accelerated toward an anode that is generally made of heavy metals. Characteristic x-rays are emitted from the collision of the incident electron with atoms in the anode. The incident electron may remove the atomic electron from the inner shells, and outer-shell electrons subsequently fill the newly formed vacancy accompanied by the emission of an x-ray photon with a specific energy. However, the lab-based x-ray sources are less efficient in producing x-rays, and the generated x-ray photons have a large energy bandwidth. Thus, lab-based x-ray sources are not ideal for monitoring the highly dynamic microstructure evolution, such as *operando* characterization of AM processes.

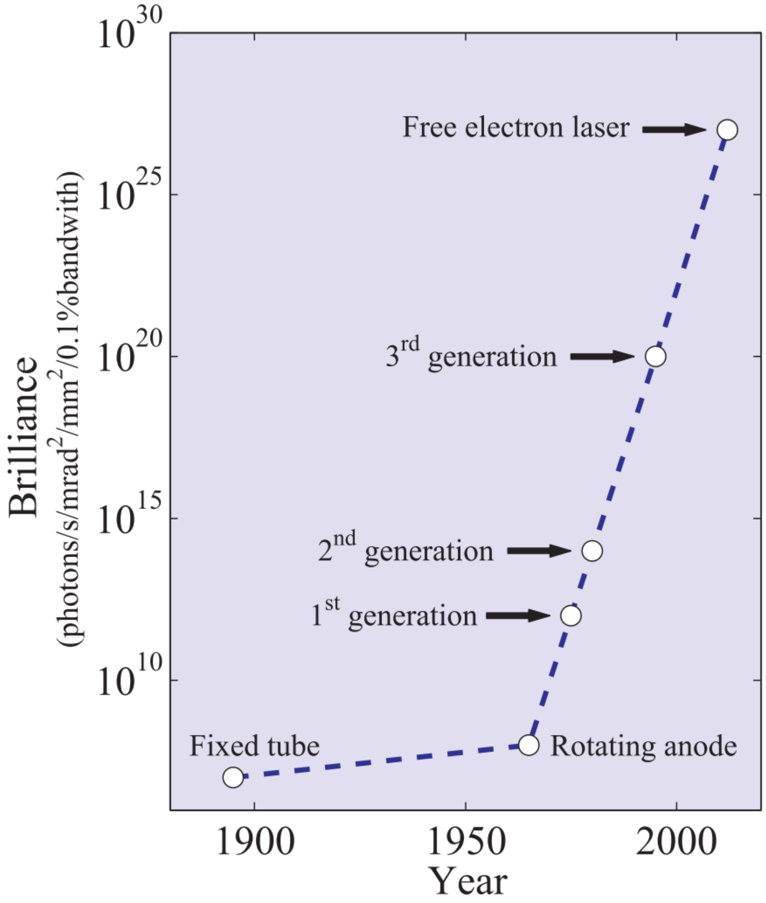

***Figure 2.2**: The development of the x-ray sources and their brilliance [92]. Brilliance is a parameter used to evaluate the quality of the produced x-ray beam. Higher brilliance refers to more photons emitted per second and better collimation of the x-ray beam.*

The advent of synchrotrons has revolutionized x-ray science. Figure 2.3 displays a schematic of the principal components of a third-generation synchrotron facility. The high-energy electrons are accelerated and then stored in a huge storage ring while keeping the constant energy. As the electrons travel along an alternating magnetic field, their small-amplitude oscillations lead to emitting x-rays. The 1-ID beamline at the Advanced Photon Source (APS) of Argonne National

Laboratory (ANL) is especially desirable for the *operando* x-ray diffraction experiments of metal AM processes due to the following advantages. First, the 1-ID beamline at APS was designed to provide brilliant and high-energy x-ray beams. The high-flux monochromatic x-ray ensures both high temporal and spatial resolution of the *operando* characterization. The high-energy x-ray, on the one hand, can reduce the attenuation when transmitting metallic samples. On the other hand, higher energy leads to a larger detection range of the scattering vector (*Q)*, which is required by the pair distribution function analysis. Secondly, this beamline equips advanced optics. The precise collimation and focusing of x-rays can be achieved. Thirdly, an advanced 2D diffraction detector is available in the 1-ID beamline, which is beneficial for monitoring the dynamic microstructure evolution during the AM process. This sensitive detector provides a high signal-to-noise ratio, critical for quantitatively analyzing the scattering data. Additionally, this sector is versatile enough to perform various measurements. Compact instruments, like the desktop DED system μprinter, can be mounted into the beamline for *operando* characterization.

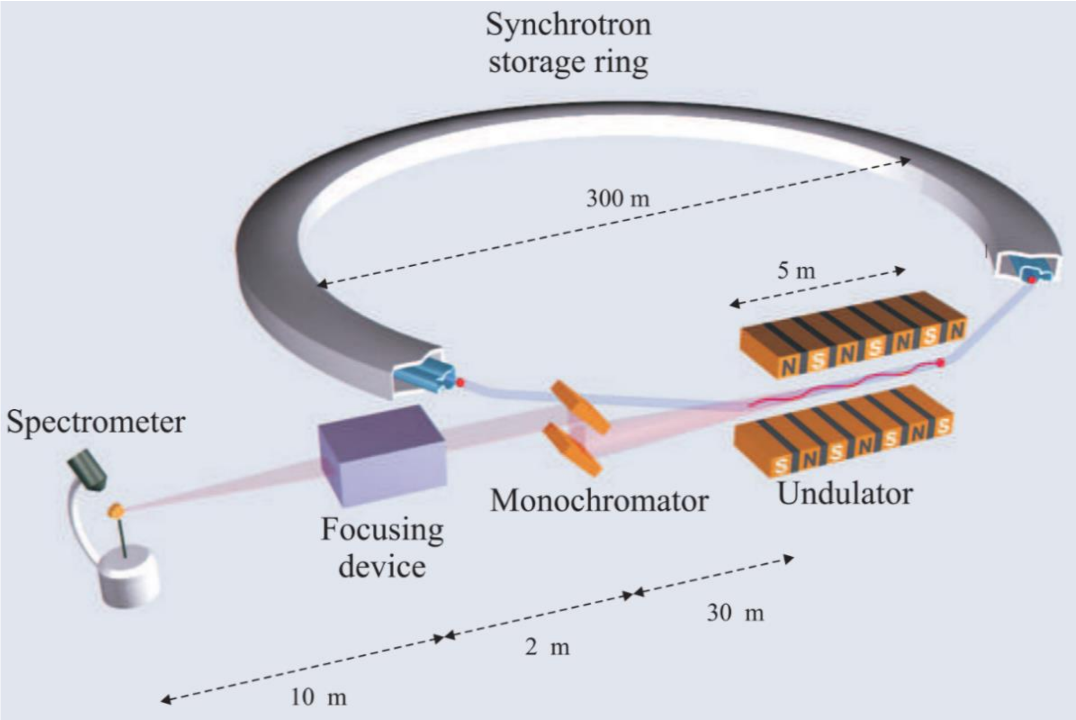

Figure 2.3*: A schematic of a beamline at a third-generation synchrotron x-ray source [92]. The key components and their approximate sizes are marked.*

2.3 *Operando* synchrotron x-ray imaging and diffraction

Operando synchrotron experiments in this work were conducted at the 1-ID-E beamline of the APS at ANL. Both x-ray imaging and diffraction experiments were carried out using a monochromatic beam with an energy of 100.0 keV generated by a superconducting undulator. Full-field x-ray imaging was applied to observe the printing process directly. The imaging detector consisted of a Pointgrey GS3-U3-23S6M-C CMOS camera, a 5× objective lens, and a 25 μm thick LuAG:Ce scintillator, which offered a pixel resolution of 1.172 μm and a frame rate of 80 Hz. Time-resolved two-dimensional (2D) diffraction patterns were collected using a PILATUS3X-2M

CdTe detector (DECTRIS, Switzerland) with a 250 Hz frame rate and an exposure time of 3 ms. In the diffraction mode, the high-flux monochromatic x-ray beam was focused vertically first using a series of saw tooth lenses and then collimated into a 100 μm (Horizontal) × 30 μm (Vertical) or 50 μm (H) × 30 μm (V) rectangular shape using slits [94].

The setup of the *operando* synchrotron experiment is illustrated in Fig. 2.4a, and a photograph of the experimental setup in the beamline is shown in Fig. 2.4b. The x-ray entrance and exit windows on both sides of the printing chamber were covered with acrylic-based laser protection glass (Kentek, USA). In the experiment, the laser printhead was stationary, whereas the build platform moved 15 mm horizontally in a plane perpendicular to the x-ray incidence (Fig. 2.4a)., where SD, BD, and TD refer to the scanning, building, and transverse directions, respectively. Through this setup, it was able to collect time-series diffraction data in hybrid mode. At the beginning and end of the single-track printing process, when the build platform was stationary, the detector captured the dynamic structural changes from the same locations in the sample. This is essentially the “movie” mode *in situ* experiment. During the stable printing process, while the platform was moved, the x-ray beam position was fixed with respect to the printhead, which allowed the characterization of material structures under identical process conditions over a relatively long time (i.e., 1-2 s). This is the data collection mode similar to a “pump-probe” type experiment, in which the time-resolved data series are obtained by piecing together the data collected with the x-ray beam set at different positions relative to the lasers. The reproducibility and stability of the *operando* experiments were assessed using four *operando* imaging and diffraction trials. The data collected during the scanning process contained several hundred diffraction patterns, which provided good statistics.

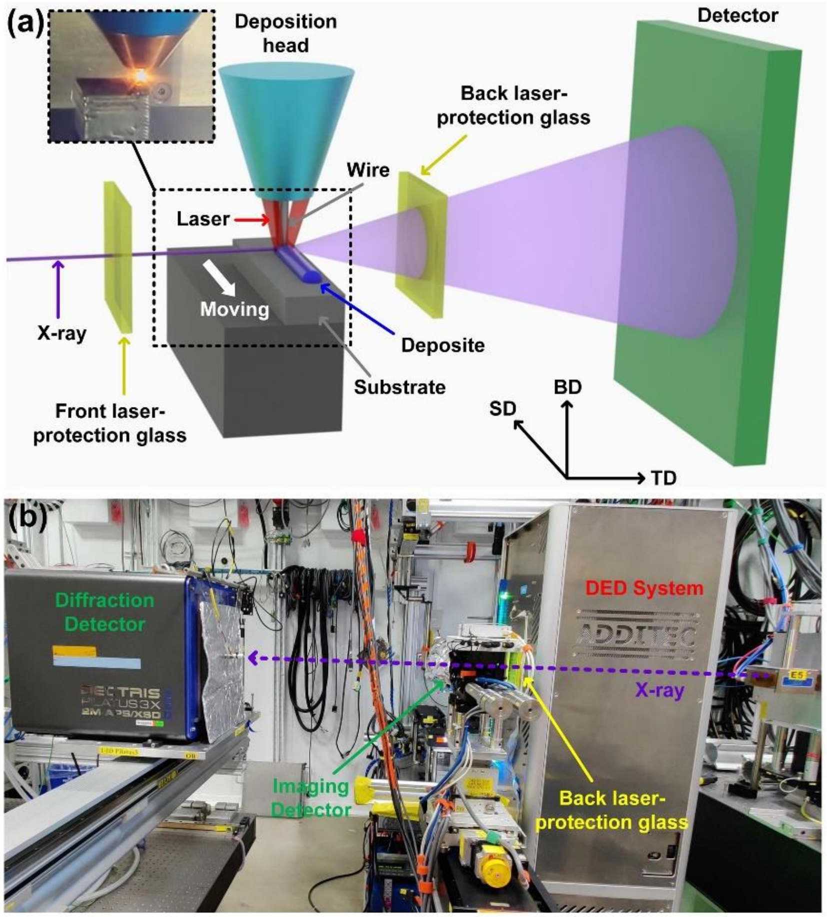

Figure 2.4: *The (a) schematic and (b) photograph of the operando synchrotron x-ray experiments on wire-laser DED process of Inconel 718 and 316L SS. The μprinter was used for the operando synchrotron x-ray characterization.*

The contrast and quality of the x-ray images were enhanced using *ImageJ* software [95]. A series of x-ray images were collected before printing to optimize the background of the raw imaging data. The raw diffraction patterns were radially integrated using *GSAS II* software [96]. The instrumental parameters, such as detector distance, were extracted from the diffraction data of the standard samples. The dead pixels on the diffraction patterns had been masked out before the integration.

2.4 Post-characterization of as-printed samples

The optical imaging of as-deposited microstructures was conducted using a Hirox Digital Light Microscope. The samples were polished first by a series of sandpapers and then electropolished in an oxalic acid solution (10 wt.%) at room temperature with a potential of 3V. Electron backscatter diffraction (EBSD) was conducted to characterize the microstructure of the as-printed samples using a Helios UC G4 dual beam scanning electron microscope or FEI Quanta 650 scanning electron microscope equipped with Oxford EBSD detectors. The sample was sectioned at the center of printed tracks or bulk samples using wire electrical discharge machining. The obtained cross-section was gradually ground using sandpapers with grit sizes ranging from 120 to 1200 and was then sequentially polished with diamond solutions and a silica suspension. The EBSD maps were post-processed using *Aztec Crystal* software.

2.5 Multi-physics simulation of wire-laser DED

Multiphysics simulations of the wire-laser DED processes were performed using the commercial software *Flow 3D* (Flow Science Inc., USA). This numerical model utilizes the finite volume method to solve the governing equations for the coupled fields of velocity and pressure, energy conservation, momentum conservation, mass conservation, and Volume of Fluid advection. Multiple physics involved in the wire-laser DED process were considered in the simulation, including wire feeding, laser absorption, incompressible flow, thermal conduction, surface tension, gravity, liquid-solid phase transformation, and viscosity. The governing equations and principal calculations for the laser-based AM module are available in [97,98]. A description of the numerical model developed to simulate the wire-laser DED process is also provided as follows.

In the simulation, the mass continuity, momentum, and energy conservations are governed by the following equations:

$$\nabla \cdot \vec{V} = 0; \qquad \text{eq. 2.1}$$

$$\frac{\partial \vec{V}}{\partial t} + (\vec{V} \cdot \nabla)\, \vec{V} = -\frac{1}{\rho} \nabla\, \vec{P} + \mu \nabla^2 \vec{V} + \vec{g}[1 - \alpha(T - T_m)]; \qquad \text{eq. 2.2}$$

$$\text{and } \frac{\partial h}{\partial t} + \left(\vec{V} \cdot \nabla\right) h = \frac{1}{\rho} (\nabla \cdot k \nabla T); \qquad \text{eq.2.3}$$

where $\vec{V}$, $\vec{P}$, μ, $\vec{g}$, α, ρ, h, and k are velocity vector, pressure, viscosity, gravity vector, thermal expansion coefficient, density, specific enthalpy, and thermal conductivity, respectively. The Maragoni and capillary effects are two major forces driving the flow dynamics, which are calculated through the following equations: $\tau_{Marangoni} = \gamma\left[\vec{\nabla} T - \vec{n}\left(\vec{\nabla} T \cdot \vec{n}\right)\right]$, and $P_{capillary} = [\sigma_0 + \gamma(T - T_m)]\kappa$, where γ, $\vec{n}$, σ_0, and κ are thermocapillary coefficients, unit vector outward normal to the surface, surface tension at T_m, and the curvature of the surface. The numerical model and geometry configuration in the multi-physics simulation of the wire-laser DED process are presented in Fig. 2.5. The material feeding and stable deposition are managed by applying two phantom components, denoted as “Phantom wire feeder” and “Horizontal phantom”, for the wire and the deposited part (including the substrate). The phantom component can assign a specific moving velocity for the solid phase within the region to achieve dynamic wire feeding and relative movement of the substrate. The phantom velocities of these two components were set based on the feeding rate of the wire and the traveling speed of the substrate applied in experiments. The coaxial wire-laser configuration, including the positions and convergence/tilting angle of three or six laser beams relevant to the wire, is set up in the model to reflect the actual geometry of the deposition heads. Based on the laser specs and measurements provided by the manufacturer, each laser beam in the simulation was modeled as a spot with a 1 mm diameter at the deposition plane and a near-Gaussian energy distribution. The irradiation of the laser beams is applied to the free surface of the material. This simulation employs the adiabatic boundary condition with constant pressure. Laser absorptivity and working distance are two major parameters input to calibrate the simulation. The laser absorptivity was assumed to be constant because the incident angle of the laser beam is nearly constant under a stable DED printing.

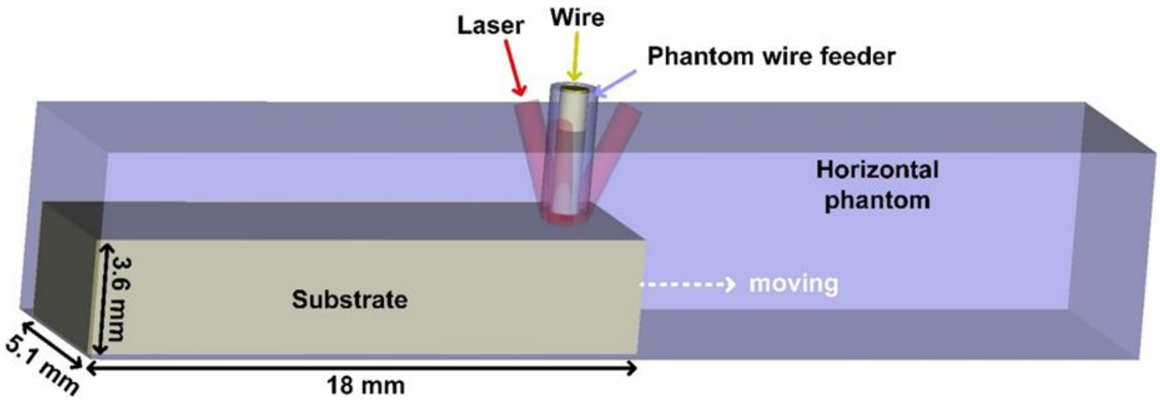

***Figure 2.5**: Numerical model and geometry configuration in the multi-physics simulation of wire-laser DED process.*

After a series of tests with different mesh sizes, a mesh size of 0.15 mm was utilized to balance the simulation accuracy and computational efficiency. Temperature-dependent parameters of Inconel 718 and 316L SS were obtained from the database built in *Flow 3D*. The material parameters at specific temperatures are listed in Tables 2.1 and 2.2. Given that the incident angles of lasers are relatively stable in the wire DED process and there is no server vapor depression in the melt pool, the laser absorptivity was assumed to be constant and calibrated based on experiment data.

***Table 2.1**: Thermophysical parameters used for simulating the wire-laser DED process of Inconel 718 alloy.*

Properties & units	**Inconel 718 alloy**
Density (kg/m^3)	8190, $T = 298$ K 7160, $T = 1873$ K
Heat capacity (J/kg/K)	435, $T = 298$ K
Thermal conductivity (W/m/K)	8.9, $T = 298$ K
Solidus temperature (K)	1533
Liquidus temperature (K)	1609

Latent heat of melting (J/kg)	2.4×10^5
Laser absorptivity	0.42
Surface tension (N/m)	1.827, $T = 1628$ K
Thermocapillary coefficient (N/m/K)	-4.43×10^{-4}
Viscosity (Pa·S)	4.42×10^{-3}, $T = 1630$ K

Table 2.2*: Thermophysical parameters of 316L SS used for simulating the wire-laser DED process.*

Properties & units	**316L SS**
Density (kg/m^3)	7950, T < 1697.15 K
	6881, T ≥ 1697.15 K
Heat capacity of liquid (J/kg/K)	830
Thermal conductivity of liquid (W/m/K)	30.5
Solidus temperature (K)	1674.15
Liquidus temperature (K)	1697.15
Latent heat of melting (J/kg)	2.6×10^5
Laser absorption	0.33
Surface tension (N/m)	1.87
Thermocapillary coefficient (N/m/K)	-4.5×10^{-4}
Viscosity (Pa·S)	8×10^{-3}

3. *Operando* high-energy synchrotron x-ray characterization of wire-laser directed energy deposition of Inconel 718

Directed energy deposition (DED) with a coaxial wire-laser configuration has gained significant attention in recent years for producing large-scale metallic components because of its low directional dependence, fast deposition rate, high feedstock efficiency, and low manufacturing cost. The work in this chapter synergistically applies operando high-energy synchrotron x-ray characterization and multi-physics modeling to study the coaxial wire-laser DED process of Inconel 718 alloy under a stable deposition condition with a low input volumetric energy density (55.48 J/mm^3*). The unique microstructure heterogeneity observed under this condition is explained based on operando x-ray diffraction and numerical simulation results. This work highlights the potential for tailoring solidification microstructure by controlling the melting state of the feedstock wire, in addition to factors such as thermal gradient and solidification velocity. Furthermore, as the first research chapter, this section elaborates on the capability of both operando synchrotron x-ray characterization and multi-physics simulation in studying the wire-laser DED process. The work presented in this chapter has been published in International Journal of Machine Tools and Manufacture 194 (2024) 104089.*

3.1 Introduction

Coaxial wire-laser DED is an emerging AM technique that has sparked a growing interest in academia and industry. As introduced in Chapter 1.2, the coaxial wire-laser configuration has multiple advantages against the lateral wire feeding system in improving the quality of printed components. Achieving consistent and high-quality products in wire DED requires a thorough understanding of wire melting, melt pool structure, and solidification processes. These behaviors are directly affected by the energy input. A good balance between the energy input and wire feeding rate is required to yield a stable printing process and reduce defects. Nonetheless, even within a stable processing window, knowledge regarding the feedstock wire behavior in the melt pool and its effects on solidification is required, particularly under printing conditions of relatively low energy input per unit volume of the deposited material (i.e., high feeding rate, low laser power, or high scanning speed). For instance, Bambach *et al.* recently investigated the coaxial wire-laser DED process of the Inconel 718 alloy. They speculated that the wire did not melt completely within the melt pool throughout the deposition process under the studied conditions [10]. The prevailing consensus is that incomplete melting of the feedstock wire hinders melt flow and induces wire oscillation, thereby resulting in increased printing imperfections, such as little pits, in the builds [99,100]. Without a more profound understanding provided by in situ experiments, an apparent solution to the problem caused by partial wire melting is increasing the input volumetric energy density (VED).

As introduced in Chapter 1.8.5, Elmer *et al.* [89] and Brown *et al.* [90] performed the *in situ* synchrotron x-ray diffraction for the wire arc welding and wire arc AM process, respectively. These studies demonstrated the unique capability of the high-energy synchrotron x-ray diffraction technique for probing the wire-based AM process. However, the electric arc created extremely intense heat around the melt pool in their wire arc processes, thereby fully melting the feedstock wire. Therefore, Elmer and Brown did not intend to reveal the temperature variations in the wires, as the wire feedstocks were deposited into the melt pool, but focused primarily on characterizing the solidification process. In contrast, for the coaxial wire-laser DED process studied here, the laser energy was uniformly distributed around the wire and absorbed only by the wire tip and melt pool surfaces. Thus, the melting state of the wire is more sensitive to the processing parameters, potentially having a greater influence on the material microstructure. However, there have not been any *operando* synchrotron experiments on the wire-laser DED process.

Operando high-energy x-ray imaging and diffraction experiments on the wire-laser DED of the Inconel 718 alloy were conducted to address the knowledge gap concerning the wire melting behavior within the melt pool. In the present DED process, a specific printing condition was tailored to establish a stable melt pool while concurrently modifying the wire melting by fine-tuning the VED. In the *operando* experiment, x-ray imaging was used to obtain real-space information on the morphological changes in the metal wire and melt pool induced by laser heating. Subsequently, a high-energy x-ray beam was focused at various locations of the melt pool to reveal the structural evolution inside the melt pool using transmission-mode diffraction. The experimental data provided valuable insights into the transient and dynamic phenomena during the printing process. In complement to these experimental efforts, multi-physics simulations were conducted to extract the difficult-to-measure structural attributes, thereby enhancing the understanding of the coaxial wire-laser DED process. This study also offers an in-depth understanding of the formation mechanism of a unique microstructure in the sample processed under a specific VED.

3.2 Methods

3.2.1 Wire-laser DED process

Printing was executed using the modified commercial DED system, µPrinter (Additec, USA). A printing condition, referred to as condition 1 herein, is designed to provide a relatively high feeding rate (F = 17 mm/s) and low energy input (laser power P = 600 W, traveling speed V = 10 mm/s) while maintaining a stable deposition process. Hence, the linear energy density can be calculated as P/V to be 60 J/mm, while the VED can be calculated as $P/A/F$ to be 55.5 J/mm^3, where A corresponds to the cross-sectional area of the feedstock wire. For comparison, two other samples were printed using different processing parameters. The conditions and sample structures are presented in the corresponding section of this chapter. High-purity Ar was blown out of the printhead throughout the printing process as shielding gas.

3.2.2 *Operando* synchrotron characterization and data analysis

Operando synchrotron experiments in this work were conducted at the 1-ID-E beamline of the Advanced Photon Source (APS) at Argonne National Laboratory. For the diffraction experiment, the x-ray beam on the sample was focused to 100 µm (Horizontal) × 30 µm (Vertical). A more detailed description of the experimental setup is included in Chapter 2.3.

The temperature evolution of the sample at the end of the printed track after solidification was determined from the measured lattice parameter and the known coefficient of thermal expansion (CTE). The detailed calculation method and temperature-dependent CTE of Inconel 718 can be found in literature [101,102]. Strong $\{111\}_\gamma$, $\{311\}_\gamma$, and $\{222\}_\gamma$ diffraction peaks were fitted using the pseudo-Voigt function to quantify the lattice parameters. A linear variation of the CTE with temperature was assumed, and the diffraction data of a printed track after complete cooling served as the reference d_0 at room temperature. Error bars represent the standard deviation from the three measurements of different diffraction peaks.

3.2.3 Multi-physics simulation and Scheil solidification simulation

Multi-physics simulations of the wire-laser DED process were performed using the commercial software *Flow 3D* (Flow Science Inc., USA). The numerical model is explained in Chapter 2.5. The exact laser configuration and substrate size in the experiments were implemented in the model. The wire feeding rate, laser power, and scanning speed are direct input variables in the simulation for different printing conditions. The cross-section of the printed track, melt pool size, and cooling rate were measured from in situ/ex situ experiments and used to validate the simulation.

3.3 Results

3.3.1 *Operando* synchrotron x-ray imaging

To better understand the printing processes under different volumetric energy density (VED) inputs, particularly a low VED of 55.5 J/mm^3 (condition 1), *operando* synchrotron experiments were performed at the Advanced Photon Source (APS). The x-ray imaging results of the single-track wire-laser DED of Inconel 718 under condition 1 are shown in Fig. 3.1. Note that the horizontal bright and dark stripes on each x-ray image are artifacts caused by the optics-induced intensity variation in the x-ray beam. The attempt to remove the background using a white-field image was not satisfactory, owing to the beam instability. The printing process of wire-laser DED consists of a few steps. Initially, the wire was pulled up and separated from the substrate by a small distance (Fig. 3.1a). The wire then started to move downward until it contacted the substrate (Fig. 3.1b). The laser was then activated and focused on the wire tip, creating a liquid droplet attached to the substrate (Fig. 3.1c). The base plate began to move horizontally to the right as the wire continued to feed into the melt pool (Fig. 3.1d). After hundreds of microseconds, a stable melt pool formed, which remained unchanged for approximately 2 s (Fig. 3.1e). Once the set printing length was completed, the wire was extracted from the melt pool (Fig. 3.1f), and all the lasers were turned off. The final melt pool (Fig. 3.1g) at the end of the printed line experienced the fastest cooling and significant thermal stress developed, which induced microcracking after solidification, marked by a red arrow in Fig. 3.1h. It is important to note that the x-ray images shown here do not reveal the melt pool boundary because the high x-ray energy used in this experiment generates no discernable contrast between the solid and liquid phases.

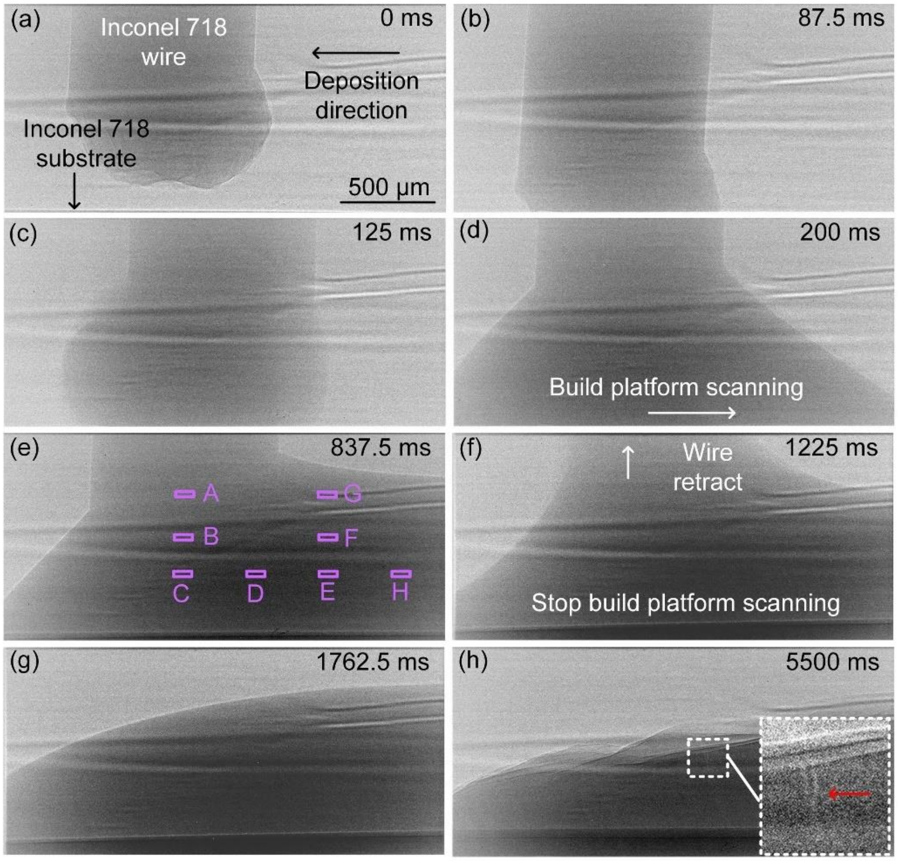

Figure 3.1: *X-ray imaging sequence revealing the wire-laser DED process of Inconel 718 with input VED of 55.5 J/mm*^{3}*. (a) Before printing; (b) start of wire feeding; (c) activating laser; (d) initial printing period; (e) stable printing period; end of the process (f) with wire retracting, (g) before solidification, and (h) after solidification. Purple rectangles in Figure (e) illustrate the regions probed by operando focused-beam x-ray diffraction with results to be shown in Fig. 3.3. Note the horizontal bright and dark stripes on each image are artifacts caused by the optics-induced intensity variation in the x-ray beam.*

3.3.2 *Operando* synchrotron x-ray diffraction in temporal and spatial aspects

Operando synchrotron x-ray diffraction is critical for measuring the cooling rate and characterizing the phase evolution during wire-laser DED. Figure 3.2a shows the waterfall diffraction intensity map as a function of time and the scattering vector (Q), which was constructed by piling all 1D diffraction spectra extracted from the time-resolved 2D diffraction patterns. For this dataset, the incident x-ray beam was placed at the spot E shown in Fig. 3.1e. In the first 800 ms (i.e., the region under the bottom white dashed line in Fig. 3.2a), the x-ray beam was not on either the metal wire or the melt pool; thus, no diffraction intensity was observed. Note that the diffraction data collection was initiated first, and the printing process was triggered manually slightly thereafter. Therefore, the period before the sample moved into the x-ray beam (800 ms in this case) varied slightly between samples. Fig. 3.2b shows a representative diffraction pattern collected during this period, which reveals no diffraction signal from the sample. Subsequently, the liquid tip of the metal wire touched the base plate, resulting in the development of the melt pool, which was then scanned by the x-ray beam. Fig. 3.2c shows a representative diffraction pattern collected from the melt pool, which exhibits typical liquid-metal scattering characteristics. In Fig. 3.2a, diffuse diffraction peaks are observed between the two dashed lines during this period. At the end of the printing track, after the wire was retracted and the laser was turned off, the sample began to experience rapid solidification and cooling. In the diffraction patterns Fig. 3.2d, the diffuse scattering peaks were replaced by strong diffraction spots. The phase evolution during and after solidification is reflected in the data region above the top dashed line in Fig. 3.2a. By indexing the diffraction peaks, it was found that solidification started with a liquid-to-gamma phase transformation. The Laves, MC-carbide, and delta phases were generated after a very short period (~80 ms), with the delta phase being the last phase to appear. During the entire data collection process, the relative location between the incident x-ray beam and the wire (or printhead) did not change, as illustrated in Fig. 3.2a.

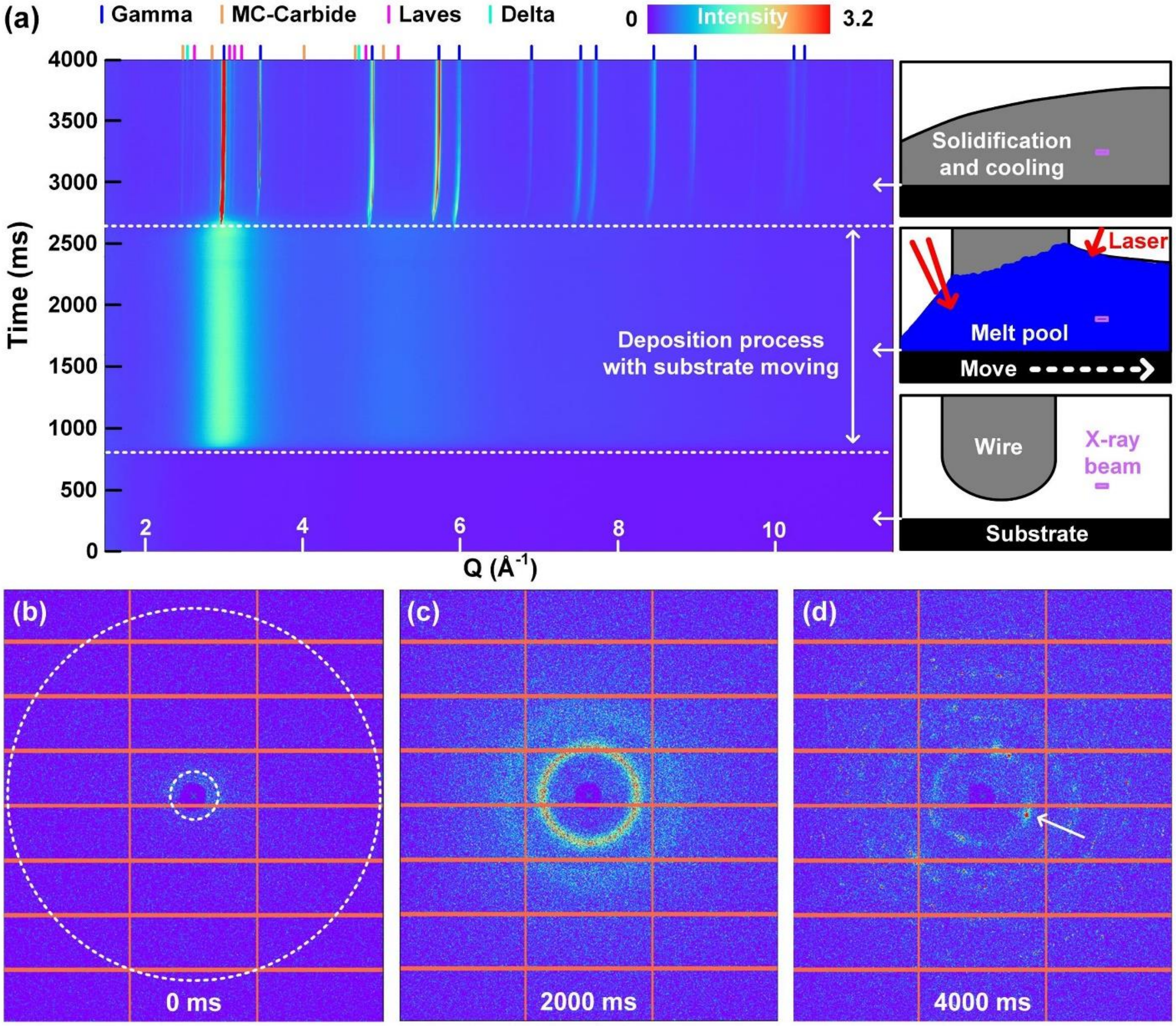

Figure 3.2: *(a) The time-resolved diffraction intensity map shows the microstructure evolution during the entire deposition process when the incident x-ray is fixed at a certain location. Representative diffraction patterns (b) before, (c) under, and (d) after deposition.*

The structural dynamics of Inconel 718 during the printing process were investigated in both the spatial and temporal domains by repeating the same experiment and setting the x-ray beam at different locations with respect to the printhead. Fig. 3.3 shows the integrated 2D diffraction patterns and the corresponding 1D spectra obtained from regions A, B, C, D, E, and H, marked in Fig. 3.1e. Each diffraction pattern results from summing 250 frames, all collected in the course of the stable printing period, which equates to one second of total exposure time. Figs. 3.3a-3.3c reveal the structure of the melt-pool region underneath the printhead. Region A was closer to the feedstock wire. Because only the surface of the wire was melted by the laser at this position, the diffraction rings from the solid Inconel 718 wire were dominant and the texture structure of the wire was observed. In regions B and C, as the wire was further extruded and melted by the laser, the x-ray scattering pattern from the liquid Inconel 718 became increasingly visible, while textured diffraction rings were still present (Figs. 3.3b and 3.3c). This indicates that under the applied processing condition, the wire was still partially melted at a location only ~300 μm above the substrate. Another important observation is that recrystallization did not occur in the unmelted part of the wire. In regions D and E, no obvious crystal diffraction peaks were observed (Figs. 3.3d and 3.3e), suggesting that the wire was almost fully melted by the surrounding hot liquid via heat conduction. In region H, well-defined diffraction peaks began to appear again on top of the liquid scattering profile (Fig. 3.3f), indicating the development of a mushy zone.

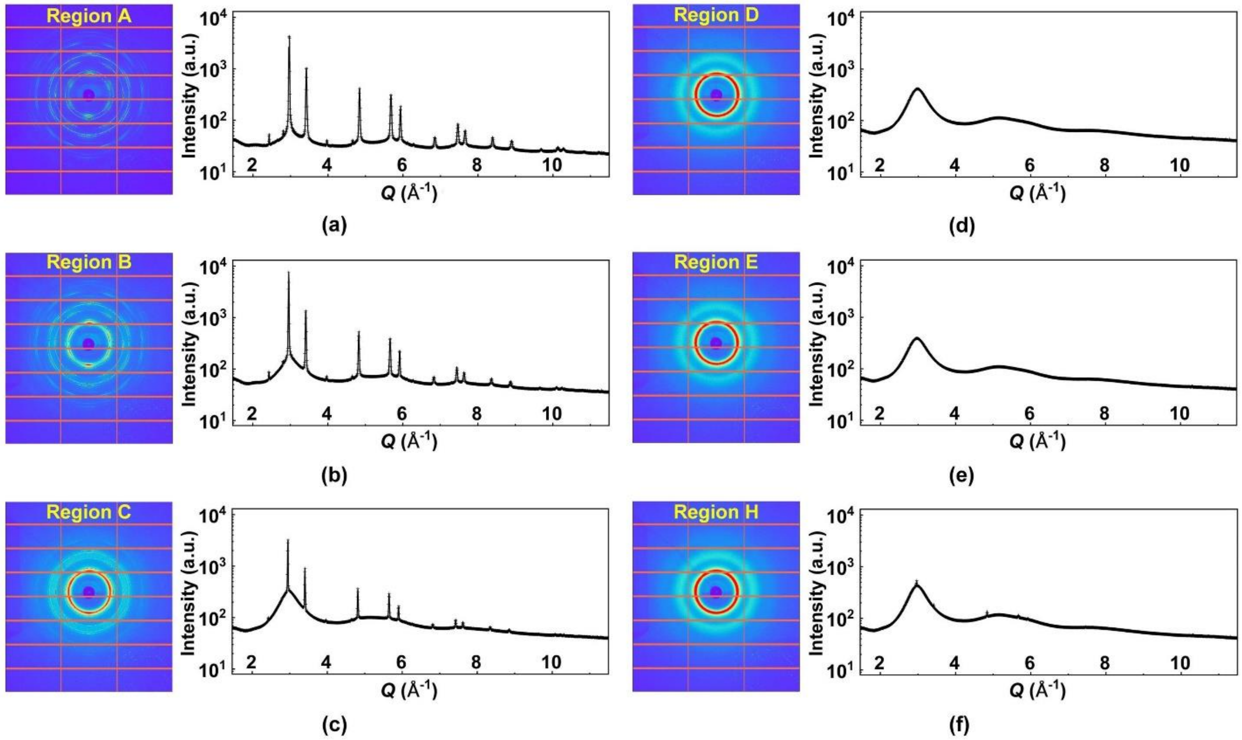

***Figure 3.3**: Local microstructures of the melt pool revealed by operando x-ray diffraction. Integrated x-ray diffraction patterns (left in each panel) and corresponding intensity spectra (right in each panel) collected during the stable printing periods by positioning the x-ray beam at the regions A-H, marked in Fig. 3.1e. Each diffraction pattern shown here is the summation of 250 frames collected during the stable printing period, equivalent to 1 sec total exposure time.*

3.3.3 Remaining solid particles inside the melt pool

Although no clear evidence of the solid phase is shown in the integrated 1D intensity spectra in Figs. 3.3d and 3.3e, solid crystal diffraction spots were still observed in a small set of data by frame-by-frame examination. The most commonly observed diffraction pattern is shown in Fig. 3.4a, only consisting of the diffusive scattering from the liquid phase. Figure 3.4b displays a representative diffraction pattern showing the appearance of the diffraction spots of MC-carbide. In addition to the carbide phase, other solid phases including Gamma, Laves, Delta, and Sigma were also found (Figs. 3.4b-3.4f). The lattice structures of these solid phases are introduced in Chapter 1.4. In Fig. 3.4g, the experimental (black) and simulated (red) diffraction profiles of the MC-carbide phase are compared. The experimental diffraction profile was obtained by summing multiple diffraction frames, which included diffraction spots from MC-carbide, and the background associated with diffusive scattering from liquid was removed. The peak positions matched those in the simulated reference diffraction profile, confirming the presence of MC carbide in certain melt pool regions during stable printing. Lattice expansion was considered in the calculation, and the peak positions at elevated temperatures were calibrated using the experiment results. The number of diffraction spots appearing in regions D, E, and F during the stable deposition process was counted and statistically analyzed. Because of the low symmetry of their crystal structures, the Laves and Sigma phases had more complex diffraction peaks than the other phases. Distinguishing the diffraction spots from these two phases becomes challenging within a specific Q range. Thus, the statistical results of Laves and Sigma phases are combined into one group as the "Laves/Sigma phase". As shown in Fig. 3.4h, more diffraction spots from solid particles are found in region D (further from the solidification front) than in region E (closer to the solidification front), and almost no solid particles were detected in region F (closer to the heating laser). In regions D and E, the MC-carbide appeared more frequently than the other solid phases, including the matrix phase (Gamma). This statistical analysis counted over 500 effective diffraction patterns in each region. The total number of diffraction spots reflects the frequency of detecting a solid particle satisfying Bragg's diffraction criterion and thereby correlates qualitatively with the phase content. However, this work did not intend to quantify the number density or volume fraction of the solid particles within the melt pool.

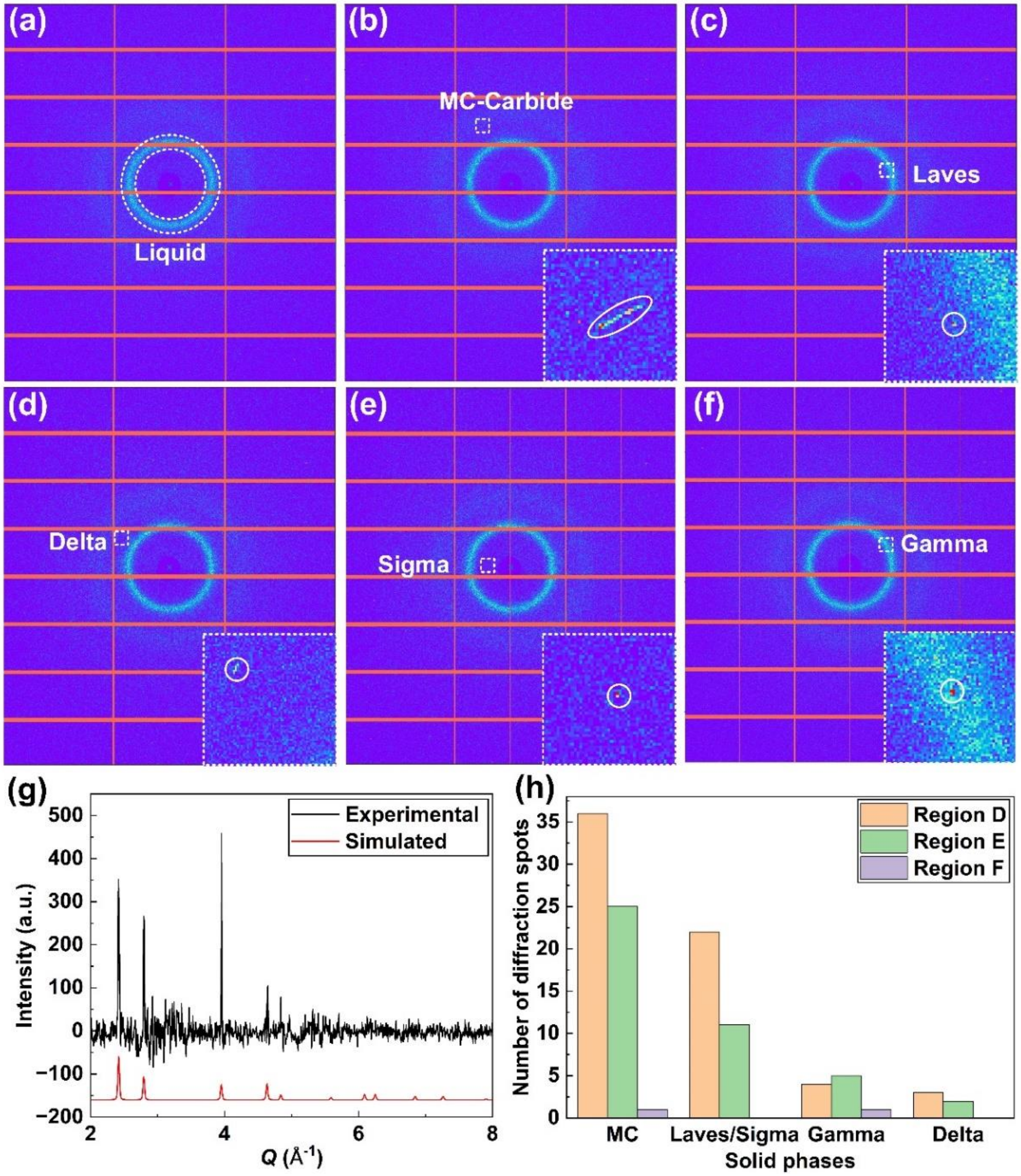

Figure 3.4*: Presence of unmelted solid particles within the melt pool. (a) A representative x-ray*

diffraction pattern; and (b) the extracted 1D diffraction intensity profile indicating the existence of MC-carbide particles in the melt pool. The result in (b) was obtained by summing and integrating multiple diffraction frames which include diffraction spots of MC-carbide at various Q values. The peak positions agree with the corresponding calculation based on the crystal structure of MC-carbide. (c) The statistical result of the remaining solid particles at different regions of the melt pool. Each set of data for a specific phase was obtained by counting the total number of diffraction spots present in the diffraction pattern sequence. More diffraction spots are found in region D than in other regions, with MC-carbide appearing more frequently than other solid phases.

Meanwhile, the shallow diffraction peaks shown in the intensity spectra in Figs. 3.3a-3.3c confirmed the presence of these secondary solid phases in the wire feedstock. Therefore, it is reasonable to believe that the solid particles in the melt pool ahead of the solidification line mainly resulted from the incomplete melting of the feedstock wire rather than from broken dendrites from the mushy zone. This claim is supported by the diffraction results from regions F and G, where no obvious diffraction spots from the solid phases were observed in region G and only trace amounts in region F. The temperatures in these two regions were higher than those in region E because of their proximity to the direct laser exposure. Thus, no solid particles were present in these melt-pool regions.

3.3.4 Multi-physics simulation

The single-track printing of Inconel 718 was simulated using a multi-physics model, as shown in Fig. 3.5a. The simulation results were calibrated and validated against the *operando* x-ray imaging result (Fig. 3.1) and the scanning electron microscopy (SEM) image of the build track cross section (inset of Fig. 3.5a). The 2D temperature distribution (colored shade) and melt flow (black vectors) at the center plane (TD view) and cross-section (SD view) during the stable deposition period are presented in Figs. 3.5b and 3.5c, respectively. In the printing process using the deposition head with three laser beams, the melting behavior of the wire was influenced more by the two front laser beams. Under condition 1, the temperature of the region underneath the feeding wire was higher than the solidus temperature but lower than the liquidus temperature, and the wire was only partially melted owing to insufficient heating. In the center plane (Fig. 3.5b), the front and rear sides of the melt pool contained two different melt flow patterns that were physically separated by the partially melted wire. The melt flow at the rear side was primarily affected by the rear laser beam radiating from the upper melt-pool surface. The recoil pressure and thermocapillary force drove the molten metal to flow away from the hot region on the melt-pool surface. In the front melt pool region, the two front laser beams induced two melt flow vortices distributed symmetrically around the center of the melt pool (Fig. 3.5c). The constant downward feeding of the unmelted wire drove the surrounding melt to the bottom of the melt pool, resulting in opposite flow directions of these two vortices.

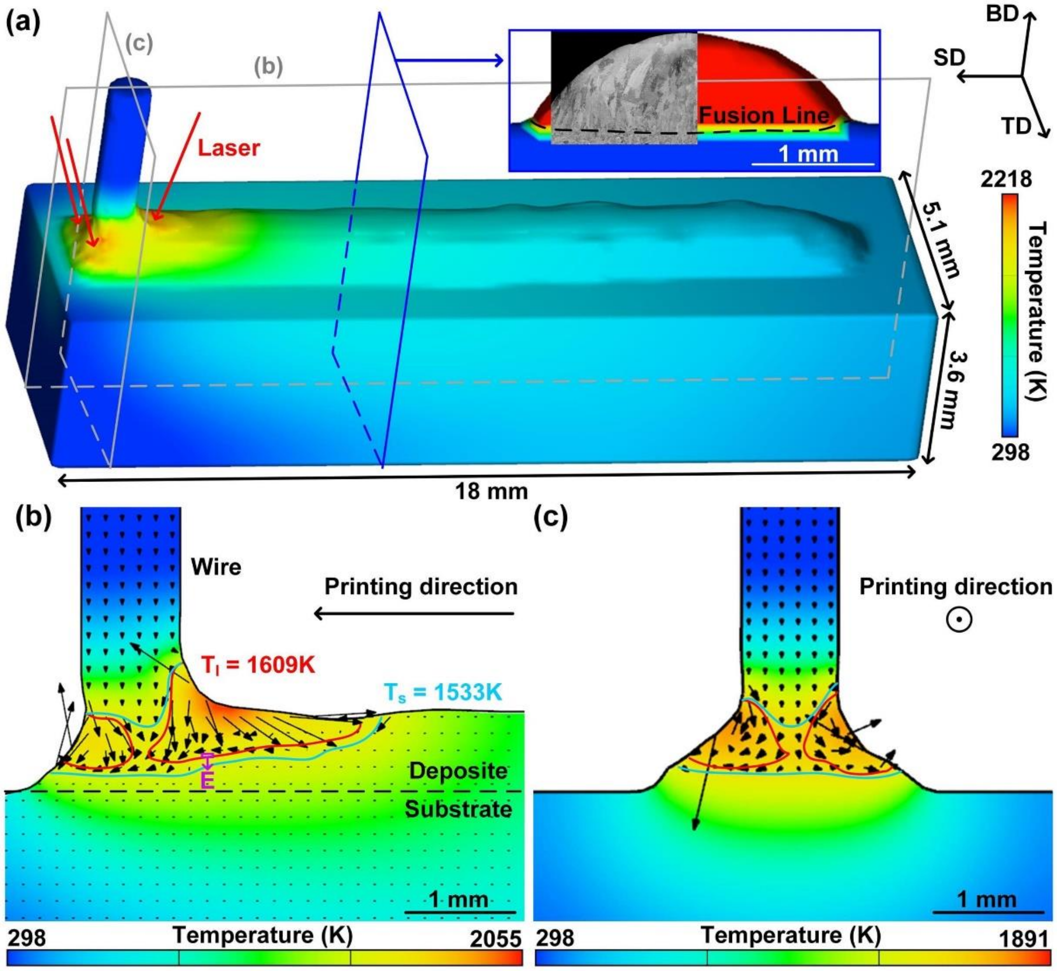

***Figure 3.5**: Multi-physics simulation of the wire DED process of Inconel 718 with input VED of 55.5 J/mm^3. (a) 3D view of the simulation. The 2D slices of (b) the center plane on the lateral view and (c) the cross-section on the front view are indicated using grey boxes. The inset of (a) depicts a comparison between the experimental and simulated build track cross-section, showing a good agreement in morphology. In the simulated cross-section, blue and red colors correspond to unmelted and fully melted regions, respectively. In (b) and (c), the color map and black arrows within the melt pool display the temperature distribution and flow dynamics. With this specific input VED (condition 1), the wire is only partially melted.*

The temperature evolution during the solidification process of the melt track (the end region after the lasers were turned off) was quantified via *operando* x-ray diffraction and multi-physics simulations. In the time-resolved diffraction intensity map (Fig. 3.2a), the shift of the diffraction peaks to a higher scattering vector (Q) corresponds to cooling-induced lattice contraction. The temperature evolution of the sample after solidification was calculated using the measured lattice parameters and the known coefficient of thermal expansion (CTE) of Inconel 718. This calculation assumes (i) no chemistry or stress-induced lattice strain and (ii) that the variation of the CTE with temperature is linear. Because the x-ray diffraction was in the transmission geometry, the measured lattice parameter (black dots in Fig. 3.6) reflected the average sample structure within an x-ray interaction volume along the TD. The average, maximum, and minimum temperatures of the sample region, which was within the x-ray interaction volume, were extracted from the simulation results. Their changes as a function of cooling time are plotted in Fig. 3.6 using blue, red, and green lines. During the initial cooling stage (1500-1250 K), the temperature dropped rapidly at a rate of approximately 3800 K/s. The cooling rate gradually decreases to approximately 80 K/s during the final stage of the measured cooling data. Simulation results also revealed that the temperature variation within the x-ray interaction volume was approximately 180 K during the initial cooling state. As the sample continued to cool, the temperature difference between the side surfaces and the center of the melt track decreased. In general, the simulation result matches the experimental measurement very well in the initial cooling stage yet deviates slightly in the low-temperature region. This may have been caused by the appearance of secondary phases (e.g., the delta phase) and the development of residual stress. The temperature evolution of the wire DED process measured using *operando* x-ray diffraction was comparable to that of the powder DED process measured using a pyrometer [103].

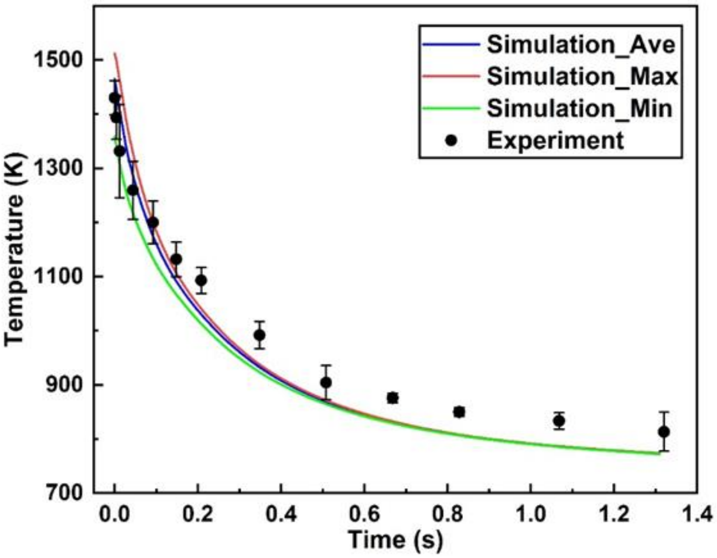

Figure 3.6*: Temperature evolution in the solid phase at the end of the print track after the wire was retracted and the laser was turned off. The black dots represent temperatures calculated via the thermal expansion of the crystal lattice, as measured by the operando x-ray diffraction experiment. Error bars represent ±1 standard deviation from the mean value from three measurements of different diffraction peaks. The blue, red, and green curves represent the average, maximum, and minimum temperatures extracted from a certain region in the simulation.*

3.3.5 Solidification microstructure under the low volumetric energy density of 55.5 J/mm^3 (condition 1)

The microstructure of single-line samples printed under condition 1 was characterized using

EBSD. Figs. 3.7a and 3.7b display the inverse pole figure (IPF) maps of the cross section in the SD and the center plane in the TD, where the fusion boundary between the printed line and the substrate is marked by a white line. As shown in Fig. 3.7a, the fusion into the substrate under condition 1 was very shallow owing to the high deposition rate and low energy input. The shallow fusion area also refers to a low dilution ratio (the ratio of the penetration depth into the substrate to the total melt pool height), a parameter widely used in the cladding community. In this sample, columnar grains are roughly aligned with BD, and the growth of columnar grains at the central bottom region (outlined by a black dashed circle in Fig. 3.7a) is suppressed compared to the outer region.

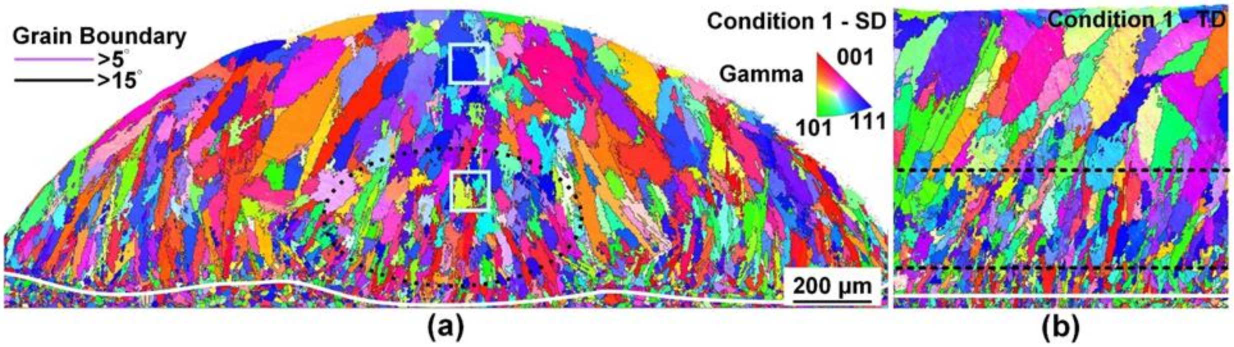

***Figure 3.7**: EBSD characterization of the printed Inconel 718 line with an input VED of 55.5 J/mm^3. (a) SD and (b) TD view of the sample. The step size of EBSD mapping is 1.5 μm. The scale bar in (a) is applicable to (b). The white lines in (a) and (b) define the fusion boundary. The two solid boxes in (a) mark the specific areas for magnified EBSD characterization shown in Fig. 3.9. The black dashed circle in (a) and black dashed lines in (b) define the interested region with suppressed columnar grain growth.*

3.4 Discussion

3.4.1 The printing behavior under the specific printing condition

The wire-laser DED process and the quality of the printed components are strongly dependent on the melting behavior of the feedstock wire. In general, a good balance between wire feeding and energy input is crucial for achieving a stable deposition process. Insufficient wire melting can lead to structural defects, such as stubbing. In this study, the wire-laser DED printing process under a specific condition (condition 1) is investigated, which happens to lie between complete wire melting and stubbing. The feedstock wire did not melt fully, as revealed by *operando* x-ray diffraction and simulation; however, stable printing was sustained without generating defects.

In the coaxial wire-laser DED process, the melting of the Inconel 718 wire starts from the surface by directly absorbing the laser energy. Under condition 1, the wire was only partially melted when it entered the melt pool. Because of the relatively low energy input, the partially melted wire can reach the bottom of the melt pool, which is characterized by lower temperatures. Upon continuous heating by the surrounding liquid, most of the feedstock wire inside the melt pool eventually melts to maintain a stable deposition. However, residual solid particles, mainly MC carbides, are present in the melt pool and affect solidification. The remaining particles were mainly distributed in the bottom region of the melt pool because the surface of the melt pool directly absorbed laser energy and was hotter. As shown in Fig. 3.4h, more carbide particles were found in the melt pool compared with other phases. The liquidus temperature of the NbC phase (1603 K) is almost the same as that of the Inconel 718 alloy (1609 K) matrix (i.e., γ phase), but the latent heat of fusion is quite different (435 kJ/kg for NbC vs. 295 kJ/kg for γ) [104]. Therefore, under the rapid heating conditions involved in the DED process, the carbide phase could experience only partial melting, whereas the Gamma phase is fully melted. Melt flow is another factor that delays the melting of carbide phases. As revealed by the multi-physics simulation (Figs. 3.5b and 3.5c), the melt flow at the rear melt pool moved downward at the center, which made it difficult for the solid particles to drift upwards and quickly melt by the lasers.

3.4.2 The variation in solidification microstructure with increasing volumetric energy density

To better understand the impact of printing conditions on the resultant microstructure, particularly the input VED, samples were printed under two additional conditions (conditions 2 and 3) with larger VEDs. The detailed parameters of all three printing conditions are listed in Table 3.1. Compared to condition 1, condition 2 had the same energy input (linear energy density) but a lower wire feeding rate. Condition 3 reduced the deposition rate and increased energy density by decreasing the traveling speed. The EBSD characterization was performed on these two samples with higher input VEDs (conditions 2 and 3), as shown in Figs. 3.8a-3.8d. In the SD view, coarse columnar grains are dominant in these two samples, which is similar to Sample 1. Such a microstructure is common for DED and wire-arc AM samples because of the high temperature gradient (G) and low solidification rate (R) involved in the solidification process [105,106]. However, in contrast to the low dilution ratio in Sample 1, conditions 2 and 3 result in greater melt penetration depths in the substrate (Figs. 3.8a and 3.8c). More importantly, condition 1 produces smaller grains exhibiting reduced elongation in morphology within the central bottom region of the printed track, in comparison to the other two samples which possess microstructures typical to laser DED and wire arc AM (WAAM) samples. A quantitative comparison was conducted for grains at the central bottom region of samples printed under all three conditions, as depicted in Figs. 3.8e and 3.8f. The grain area and the fitted ellipse aspect ratio (FEAR) were measured to present the grain size and morphology. As shown in Figs. 3.8e and 3.8f, the average grain areas at the marked region of these three samples are 701.1, 820.2, and 1188.0 μm^2, respectively. The average FEAR values are 3.1, 4.9, and 2.6. This result suggests that condition 1 led to smaller grains in that region. In comparison, conditions 2 and 3 generated longer grains in shape and larger grains in size. The constrained VED is responsible for the special microstructure heterogeneity in Sample 1. The possible mechanisms will be analyzed and illustrated in the following discussion through two aspects, i.e., the unmelted solid particles inside the melt pool and G-R conditions of solidification.

Table 3.1: *All three printing parameters applied for the wire-laser DED process of Inconel 718. The detailed printing parameters of conditions 1, 2, and 3 are summarized. Conditions 2 and 3 present larger VED than Condition 1.*

Conditions	***P*** **(W)**	***V*** **(mm/s)**	***F*** **(mm/s)**	***LED*** **(J/mm)**	***VED*** **(J/mm^3)**
1	600.0	10.0	17.0	60.0	55.5
2	600.0	10.0	14.0	60.0	67.4
3	600.0	6.7	11.4	89.6	82.7

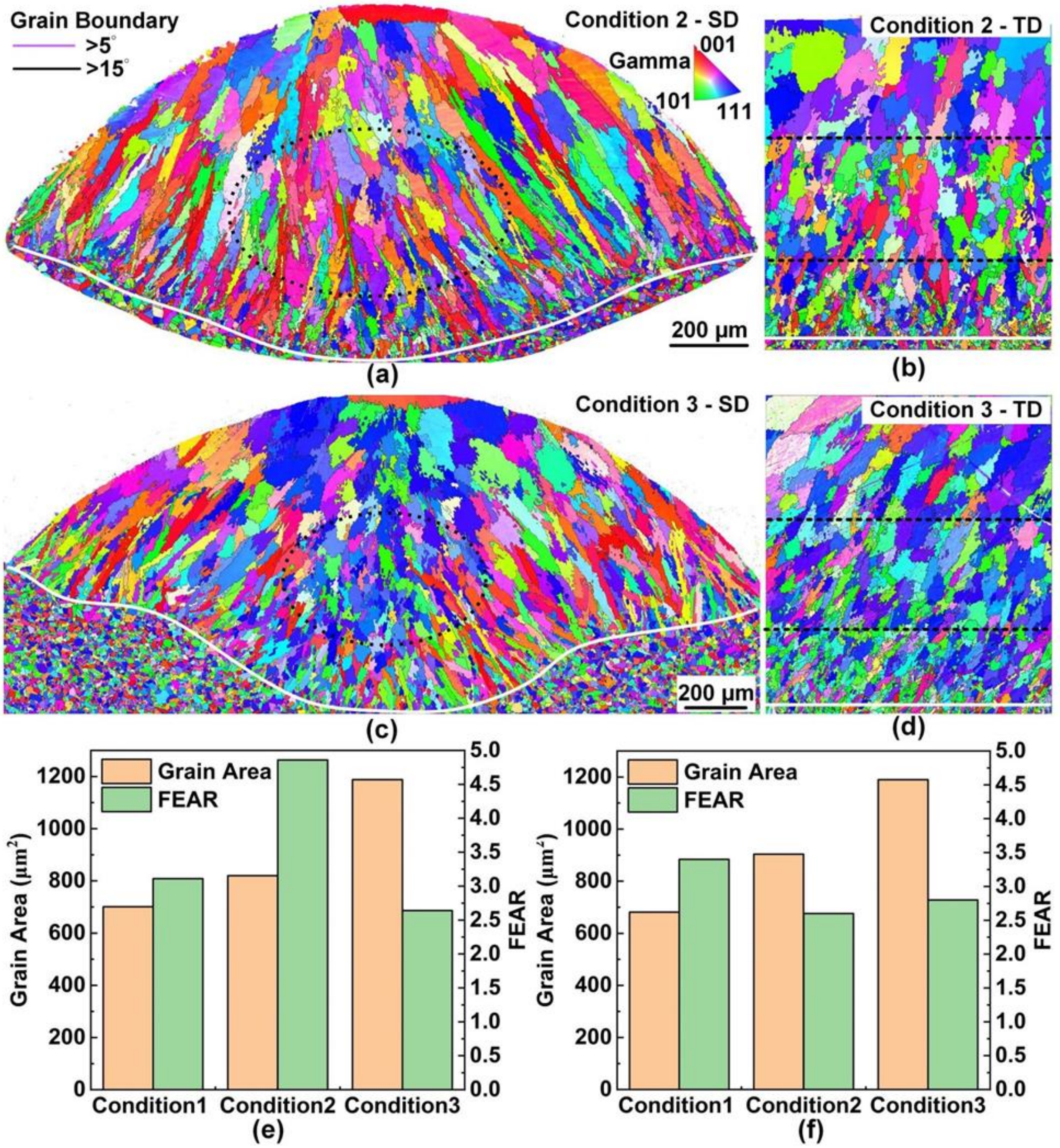

Figure 3.8: *EBSD characterization of the printed Inconel 718 line under conditions 2 and 3. (a) SD and (b) TD view of Sample; (c) SD and (d) TD view of Sample 3. The step size of EBSD mapping is 1.5 μm. The scale bar in (a) and (c) is applied for its TD view (b) and (d). The white straight/curved lines mark the fusion boundary. The black dashed circle and black dashed lines in (a-d) define the center bottom region mentioned in the main text. Average grain area and Fitted ellipse aspect ratio (FEAR) were measured from the specific regions on the SD (e) and TD (f)*

EBSD maps in Figs. 3.7 and 3.8. A low FEAR value and smaller grain area indicate the production of less elongated and smaller grains produced under printing condition 1.

3.4.3 The effect of unmelted carbides on solidification microstructure

The presence of small solid particles near the mushy zone front can affect the solidification behavior in two ways: (i) promoting heterogeneous nucleation and (ii) impeding grain coarsening. In sample 1, small grains with a relatively spherical geometry were only observed in the bottom center region, which agrees with the distribution of solid particles inside the melt pool (Fig. 3.4h). The distribution of the carbide phase in the printed sample supports this reasoning. The corresponding EBSD phase maps of sample 1 are shown in Fig. 3.9. In the bottom region of the sample (Fig. 3.9b), carbides were randomly distributed on the grain boundaries, likely owing to unmelted carbide particles pinning on the primarily solidified grain during the initial solidification. However, the continuous distribution of carbides along the grain boundaries in the top region of the sample indicated element segregation at the grain boundaries formed at a later cooling stage (Fig. 3.9c), which is typical in a DED sample.

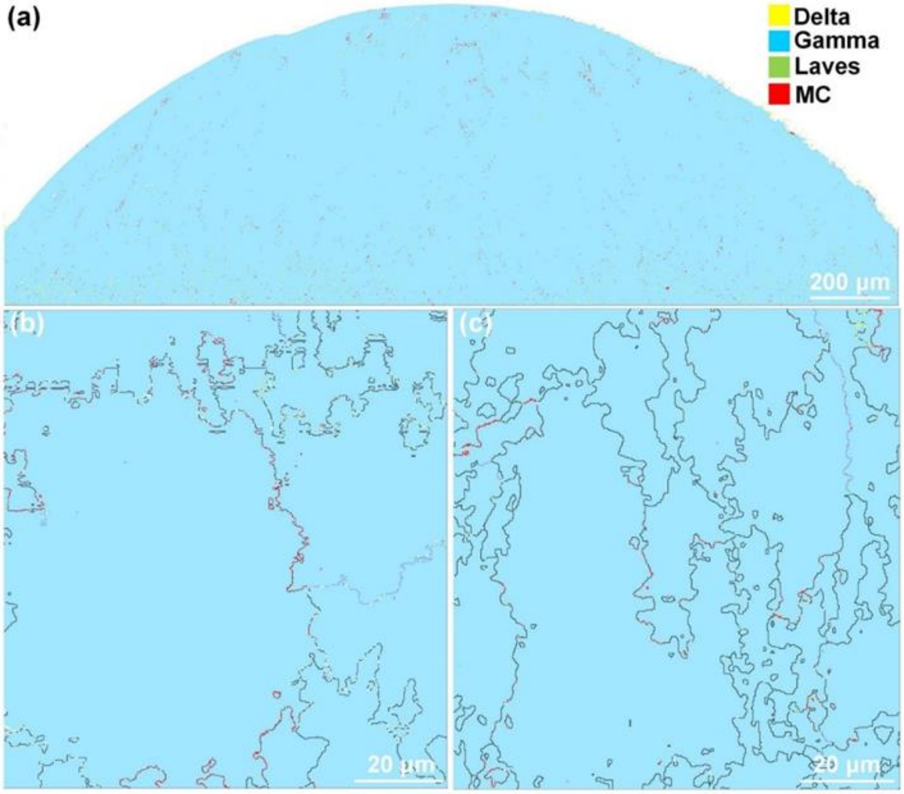

Figure 3.9: *(a) The corresponding phase map of Figure 3.7a. High-resolution phase maps of the (b) top and (c) bottom rectangular regions marked in Figure 3.7a. The high-angle and low-angle grain boundaries are represented by black and purple colors, respectively.*

Although the magnified EBSD maps shown in Fig. 3.9 applied the small step size of 0.25 µm, the signal of each carbide along grain boundaries is only represented as a few pixels. To further compare the morphology and distribution of carbides in different regions of the as-printed track, high-resolution scanning electron microscopy was performed on the central bottom and top regions. Figs. 3.10a, 3.10c, and 3.10d show the microstructure at the central bottom region of the printed track, and Fig. 3.10b shows the energy-dispersive spectroscopy (EDS) mapping of the carbides in the marked region of Fig. 3.10a. In this region, isolated Nb-rich carbide particles (darker contrast) were randomly distributed on the grain boundaries and in interdendritic regions, as indicated by the white arrows. These carbide particles had irregular shapes and were typically smaller than 0.5 μm in size. The carbides in the top region of the as-printed track are shown in Figs. 3.10e and 3.10f. In contrast, the carbides in this region exhibited strip-like shapes and were formed along the grain boundaries and interdendritic regions. This difference also suggests distinct carbide formation mechanisms in these two regions. The irregular and isolated carbides observed in the central bottom region resulted from unmelted particles in the melt pool, whereas the strip-like carbides formed during solidification owing to element segregation. This observation is consistent with the features of the EBSD phase maps characterized by the different regions.

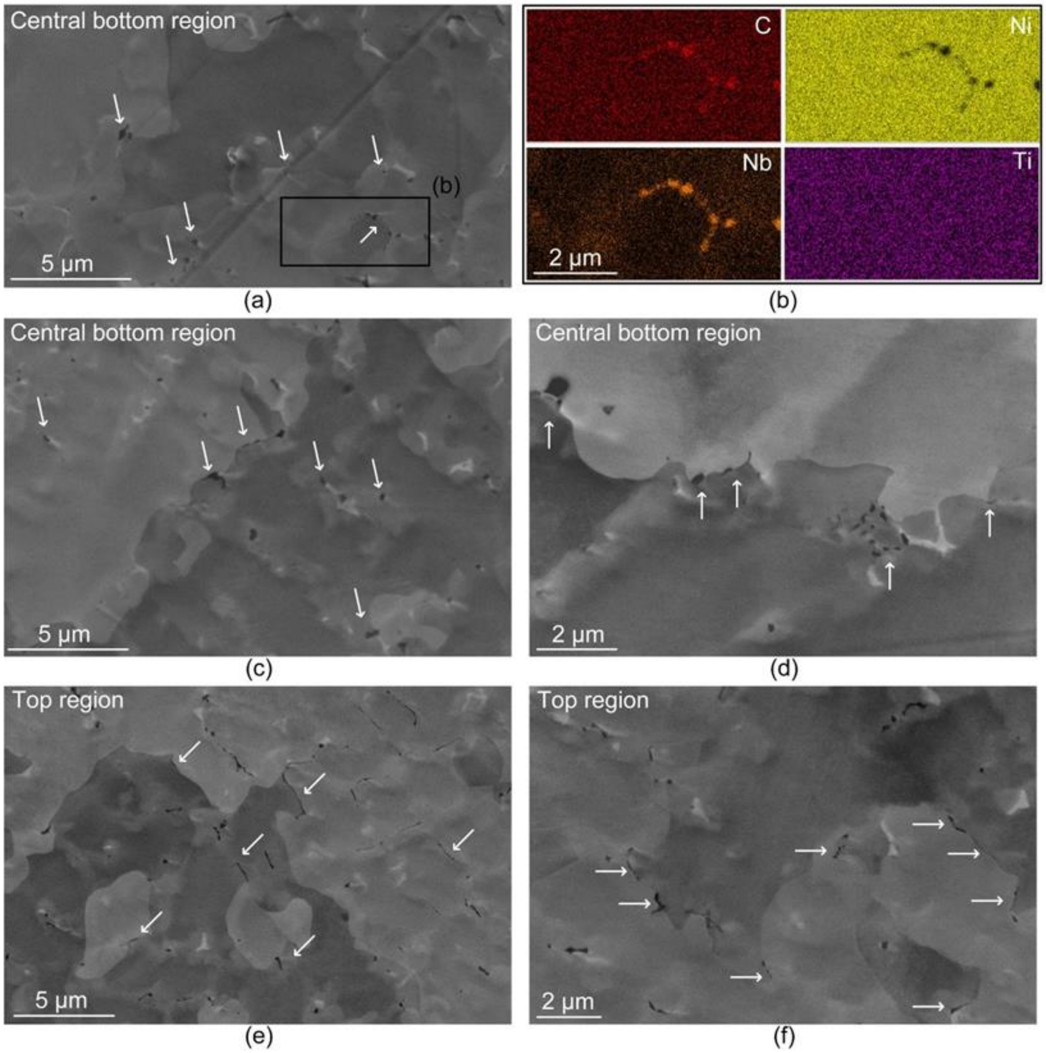

Figure 3. 10: *Scanning electron microscopy (SEM) of the printed Inconel 718 line with a low input volumetric energy density of 55.5 J/mm^3 (condition 1). The SEM images display the distribution and morphology of carbides in the (a, c, d) central bottom region and (e, f) top region of the printed track. Figure (b) is the energy disperse spectroscopy mapping of the carbides in the marked region of Figure (a). The concentration of carbon and niobium confirms that these particles are Nb-rich carbides. White arrows in the SEM images point out the carbides for improved visualization. In the central bottom region, these carbides appear as isolated particles on grain boundaries, indicating the influence of unmelted carbides on solidification. In the top region of the printed*

track, carbides exhibit strip-like morphologies distributed along grain boundaries and interdendritic regions, attributed to the solidification of carbides due to element segregation.

The large dilution ratios and large melting depths of the substrates (Fig. 3.8) indicate that under conditions 2 and 3, the bottom melt-pool regions possessed relatively high temperatures. Figure 3.11 compares the *operando* x-ray diffraction results from region C in Samples 1 and 3. Feedstock wire in the printing process under condition 3 was fully melted. The thermal conditions governing solidification were also analyzed through multi-physics simulations. The results reveal that the wire could be fully melted at the bottom of the melt pool for conditions 2 and 3.

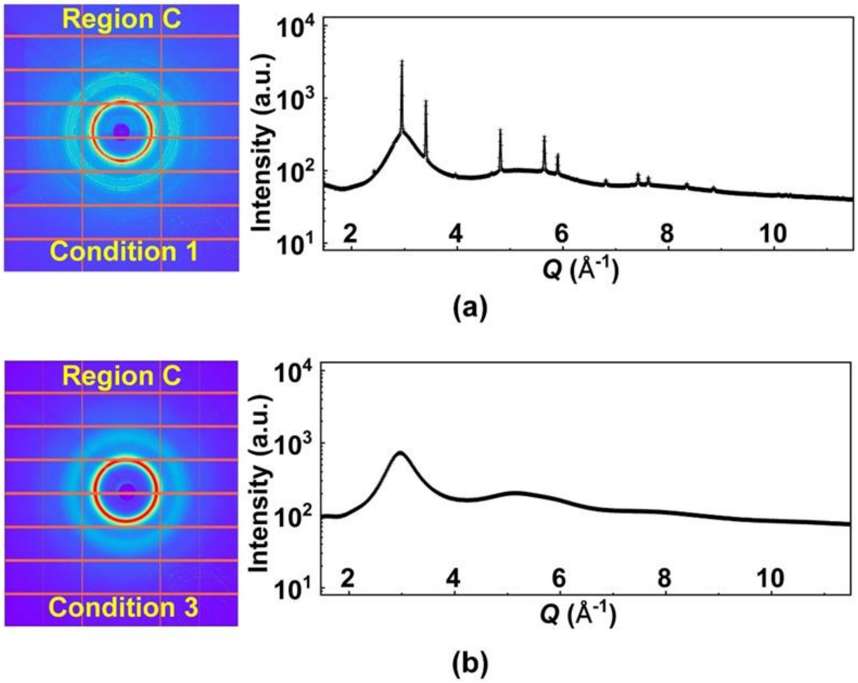

Figure 3.11: *The comparison of the wire melting under between condition 1 and condition 3 at the equivalent region "Region C". Figure (a) is a copy of Fig. 3.3c, and Figure (b) is the counterpart*

of operando diffraction data corresponding to the printing condition 3.

3.4.4 The effect of thermal conditions on solidification microstructure

Three directional components of the temperature gradient, G_{SD}, G_{TD}, and G_{BD} were extracted from the simulations for all three printing conditions. Figure 3.12 shows the top view of the temperature gradient distribution near the solidification front of the mushy zone. Visualization employed an isosurface defined by a solidification fraction of 0.1. White and black dashed curves outline the lower and upper regions of the iso-surface. As revealed by the temperature gradient distribution, the thermal gradient at the bottom melt pool region was dominated by the G_{BD} across all three printing processes. In regions close to the sample surface, the G_{BD} decreased, whereas the G_{SD} increased to the same level as the G_{BD}. Regarding G_{TD}, its magnitude increased with the distance from the melt pool center. The temperature gradient distribution agreed with the grain morphology of the as-printed samples. Under conditions 1 and 2, the solidification progressed primarily from the bottom to the top of the melt pool, as reflected by the coarse columnar grains aligned along BD. Condition 3 had a lower deposition rate but higher energy density than the other two conditions, thereby creating a wider melt pool. In this scenario, the G_{TD} plays a more important role in solidification. Therefore, solidification tends to start from the outer region of the melt pool and ends at the center. Thus, the large columnar grains grew symmetrically toward the centerline of the melt pool in Sample 3.

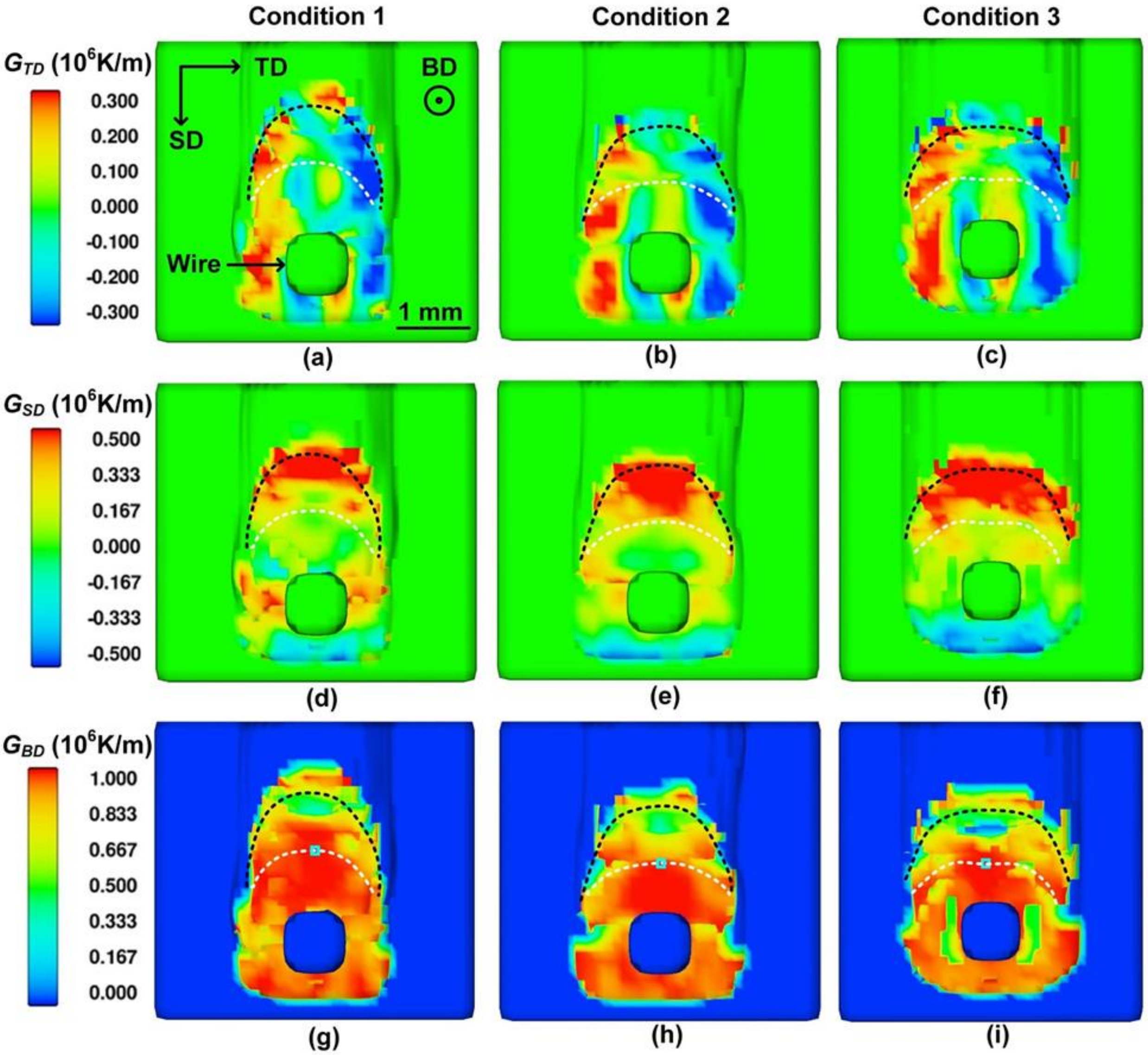

Figure 3.12: *The simulation results show the distribution of temperature gradient in the printing processes under conditions 1, 2, and 3. (a-c)* G_{TD}*, (d-f)* G_{SD}*, and (g-i)* G_{BD} *distributions on the iso-surface with a solid fraction of 0.1 within the melt pool. White and black dashed curves outline the lower and upper regions of the iso-surface.*

The specific solidification conditions (G and R) at the center-bottom region of the melt pool were extracted for conditions 1, 2, and 3 and are marked in an established solidification map of Inconel 718 in Fig. 3.13 [107]. The solidification conditions of all three samples are located in the zone corresponding to columnar grains. The G-R for conditions 1 and 2 exhibited notable similarity; however, a finer microstructure is only observed in Sample 1. Therefore, this work argues that the unique solidification structure in Sample 1 that developed under this specific printing condition was caused by the presence of the remaining solid particles in the melt pool.

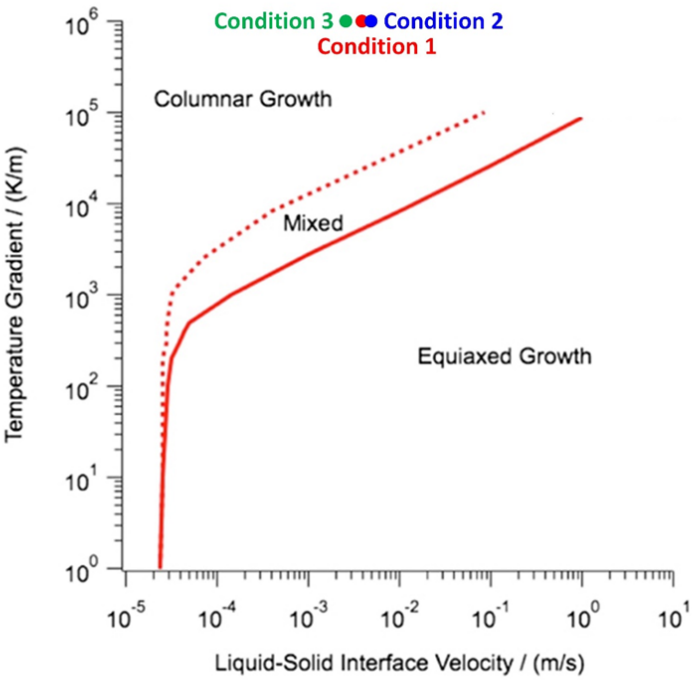

Figure 3.13*: Solidification conditions of different printing parameters with reference to a solidification map of Inconel 718 [107]. The comparison was conducted for the regions marked by solid boxes in Figs. 3.12g-3.12i. The temperature gradient G on the plot refers to the directional maximum G computed by G_{SD}, G_{TD}, and G_{BD}. For all three printing conditions, the solidification*

conditions at the center bottom region of the melt pool are located in the zone corresponding to columnar grains.

Notably, the grain-refinement mechanism discussed herein may not produce fully equiaxed and randomly oriented grains. Achieving a fully equiaxed microstructure is extremely difficult in AM processes involving large melt pools such as laser DED and WAAM. This is because solidification in these processes is dominated by a large temperature gradient. In the case of this work, the solid particles induced by the incomplete melting of the feedstock wire exhibited effects similar to those of refractory particles intentionally added to the feedstock in previous studies on WAAM [51]. Instead of yielding fully equiaxed grains, the presence of these solid particles in the melt pool led to the formation of shorter columnar grains during WAAM. Although heterogeneous nucleation can reduce the energy barrier for forming stable nuclei, the columnar growth of grains remains more favorable in the DED and WAAM processes owing to the steep temperature gradient. Adequate undercooling is a prerequisite for heterogeneous nucleation. In addition, the influence of solid particles on heterogeneous nucleation depends on several factors, including particle size, distribution, number density, and local thermal conditions. In the present scenario, unmelted particles may not be sufficiently abundant to induce the formation of tiny equiaxed grains or change the crystallographic texture.

3.5 Conclusion

This work investigated the coaxial wire-laser DED process of an Inconel 718. Unique microstructure heterogeneity was observed in samples processed under specific VED conditions. An in-depth mechanistic study was conducted using *operando* high-energy synchrotron x-ray techniques and multi-physics simulations. It was found that, by tuning the volumetric energy density, the feedstock wire could only be partially melted as it entered the melt pool. Although the wire continues to be heated and melted by the surrounding melt pool, some solid particles, such as MC-carbide, remain in the bottom region close to the mushy zone. These small particles promote heterogeneous nucleation and impede grain coarsening, resulting in small grains in the region where they are present.

This finding suggests a new method for tailoring the structure and properties of wire-laser DED materials by controlling the melting state of the feedstock wire. Traditionally, for any AM process of an alloy, a process map is established with zones that correspond to built structures exhibiting different levels and types of defects (e.g., porosity and balling). Within the "good" process window, the microstructure control is generally guided by G and R. Yet, this study demonstrated that in wire-laser DED process, another "knob", manipulating the melting state of the feedstock wire, can be used to further tailor the microstructure. The specific condition studied here represents a relatively low VED within the "good" process window. Therefore, when considering industrial production, advocating for such printing conditions could promote more economically efficient manufacturing practices.

This work further demonstrates the applicability of synchrotron x-ray techniques for *operando* studies of metal AM processes. Full-field x-ray imaging provided an overview of the printing process and guided the positioning of the focused x-ray beam for the diffraction experiment. X-ray diffraction was used to characterize wire melting, melt pool development, and solidification behavior. By fixing the printhead while scanning the build platform, the time delay in the dynamic diffraction data was translated into the spatial separation between the x-ray beam and printhead. Thus, a longer probing time can be used to obtain high-quality diffraction data, even in the liquid phase. This work highlights the potential of future *operando* synchrotron experiments on wire-laser DED process to deepen our understanding of this emerging metal AM technique, while also providing critical data for calibrating, validating, and informing numerical models.

4. Tailoring material microstructure and property in wire-laser directed energy deposition through a wiggle deposition strategy

Developing effective strategies for directly controlling material microstructure, properties, and anisotropy is an active research area in metal additive manufacturing. Chapter 3 illustrates a strong correlation between the wire melting and solidification microstructures. In contrast to the focus on energy input in Chapter 3, the present chapter explores novel and practical printing strategies for flexible control of microstructure in wire-laser DED. In this effort, a wiggle deposition pattern is developed for wire-laser directed energy deposition (DED) of 316L stainless steel (SS) to modify the crystallographic texture, especially in the building direction, in as-deposited bulk samples. Various characterization approaches and modeling methods have been applied to identify the underlying mechanism relevant to the specific texture generation and examine the effect of crystallographic textures on mechanical anisotropy. The work presented in this chapter has been published in Additive Manufacturing 77 (2023) 103801.

4.1 Introduction

As explained in Chapter 1.5, wire-based DED tends to generate a strongly textured microstructure due to the directional solidification and relatively slow cooling rate (compared with laser powder bed fusion) [32]. The crystallographic texture is an important concern in metal AM because it significantly affects the mechanical anisotropy and other properties of as-printed samples. Therefore, the flexible control of texture is of great significance for fabricating components with superior performance and tailoring structures adapted to complex serving environments.

This work developed a facile wiggle deposition strategy for wire-laser DED of 316L stainless steel (SS), which periodically alternates the scanning direction in every single track to yield a constantly wobbling melt pool. The microstructure of as-deposited samples was characterized using optical imaging, scanning electron microscopy (SEM), and synchrotron x-ray micro-computed tomography (μXCT). To unravel the solidification mechanism of the wiggle deposition, this work investigated the melt flow and thermal conditions involved in the DED process using *operando* high-speed near-infrared (NIR) imaging, multi-physics simulation, and *operando* synchrotron x-ray diffraction synergistically. The deformation behavior was investigated experimentally and numerically using electron backscattering diffraction (EBSD) and crystal plasticity simulations, respectively. Tensile loading was performed to measure the strength and ductility in samples cut along different directions in order to assess the heterogeneity in mechanical properties. According to the comprehensive investigation, this work offers a unique approach for tailoring local properties by controlling melt pool instability by applying different tool paths.

4.2 Methods

4.2.1 Sample preparation

Bulk 316L SS samples were fabricated using the commercial DED printer Meltio M450 with six diode laser sources (Fig. 4.1a). These six laser beams provide a uniform energy distribution at the deposition plane, as sketched in Fig. 4.1b. The total laser power used in this experiment was

800 W, which was evenly distributed over six laser beams. The travel speed and deposition rate were 7.00 mm/s and 16.31 mm^3/s, respectively. The deposition head was stationary during the printing process while the building platform was translated in both lateral and vertical directions. Two scanning paths, bi-directional (Bi) and wiggle (Wig), were applied to deposit each layer, as illustrated in Figs. 4.1c and 4.1d, respectively. In the Wig deposition pattern, the scanning turns 90° every 1 mm back and forth, creating an effective track width of ~1.4 mm. The Wig deposition constantly provides a transverse deposition displacement slightly shorter than the melt pool width, yielding a dynamic melt pool rather than simply changing the deposition direction. Meanwhile, the 90° rotation angle was selected for the alternating scanning directions to balance the deposition components in both scanning and transverse directions. The software *Simplify3D*® was used to create the codes controlling the scanning patterns. Simple bulk samples with the dimension of 30 (L) × 15 (W) × 42 (H) mm^3 were printed on 316L SS build plates. The build chamber was filled with Ar (99.999% purity) protection gas to prevent oxidation. The Ar shielding gas was also activated during the deposition process.

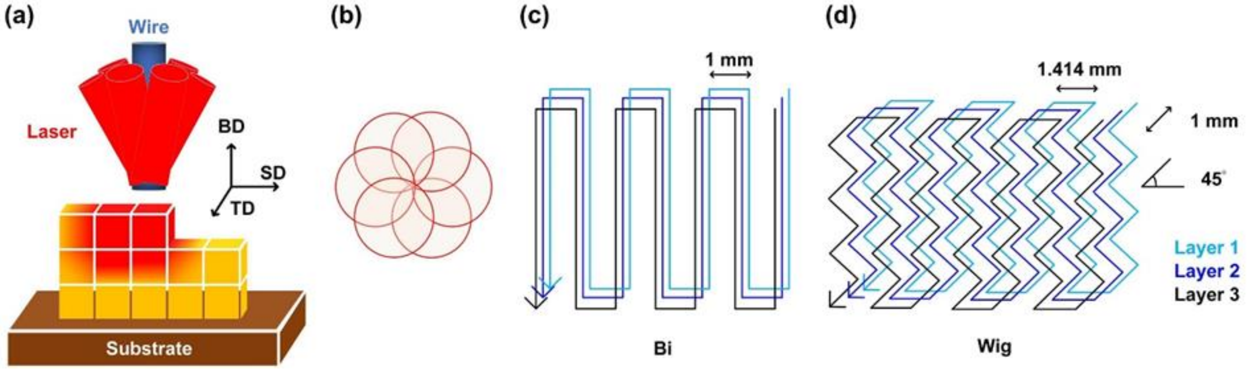

Figure 4.1: *Schematic illustration of (a) the deposition head, (b) laser positions at the deposition*

plane, (c) the conventional Bi deposition pattern, and (d) the newly developed Wig deposition pattern.

4.2.2 Microstructure characterization

The microstructure of as-printed samples characterized using scanning electron microscopy (SEM) and optical imaging is explained in Chapter 2.4. The SEM samples were cut from the center region of the as-deposited bulks. μXCT characterization of as-deposited samples was conducted at the 2-BM beamline of the Advanced Photon Source (APS) at Argonne National Laboratory. A white beam filtered with a 3 mm copper plate for suppressing low-energy photons was used in the μXCT experiment to guarantee penetration of x-rays through samples with the image contrast level suitable for further data analysis and segmentation procedures. Tomographic projections were collected in an on-the-fly scan mode while the sample was continuously rotated over 180° at 2.4° per second, which yielded 75 seconds for each 180°-scan of 1500 projection angles. FLIR Oryx ORX-10G-51S5M camera with 2448 × 2048 pixels (pixel size 3.45 μm × 3.45 μm) recorded projections from a 100 μm-thick LuAG:Ce single-crystal scintillator and with 5× lens magnification yielding a resulting isometric voxel size of 0.69 μm. The data processing, reconstruction, and visualization were performed using the Python package *Tomopy* [108] and the *Dragonfly* software (Object Research Systems), respectively.

4.2.3 Mechanical property measurement

To investigate the effect of the deposition strategies on the mechanical properties, uniaxial tensile tests along the building direction (BD), transverse direction (TD), and scanning direction (SD) were performed for both Bi and Wig samples. The flat tensile specimens were cut from the center region of the DED bulk samples by electrical discharge machining, and the sample surface was mechanically polished before loading. The gauge region of the tensile samples had a dimension of 8 (L) × 3 (W) × 1.5 (T) mm^3. Uniaxial loading was applied at room temperature using a loading frame (Model C43.304, MTS Systems) with a strain rate of 1×10^{-3} s^{-1}, and an extensometer measured the strain. Some specimens were tested until failure and used for fractography, while some tests were interrupted after 30% true strain to perform post-deformation microstructure characterization using EBSD. Hardness tests were performed using the Tinius Olsen FH-14 hardness testing instrument with 0.5 kgf force and 15 s dwell time. Each hardness measurement was repeated five times to obtain the average value and standard deviation.

4.2.4 Multi-physics modeling

The wire-laser DED processes using Bi and Wig deposition strategies were simulated using the commercial software *Flow-3D* (Flow Science Inc). This software solves the governing equations, including the coupled fields of velocity and pressure, energy conservation, and Volume of Fluid advection via the Finite Volume Method. The Volume of Fluid method was used to track the free surfaces. The physics of incompressible melt flow, laser energy absorption, thermal conduction, surface tension, gravity, phase transformation, and viscosity were considered. A detailed description of the modeling configuration can be found in Chapter 2.5. The actual laser distribution was incorporated into the simulation. In the simulation of the Wig deposition processes, a dynamic velocity was applied in the transverse direction based on the set wiggle deposition path.

4.2.5 *Operando* synchrotron characterization

The *operando* high-energy synchrotron x-ray diffraction of the wire-laser DED process was conducted at the 1-ID-E beamline of the APS. Another DED system (Additec µPrinter) was used to execute the deposition process. Single-track straight and wiggle depositions were performed with 360 W laser power, 7 mm/s traveling speed, and 18.7 mm^3/s deposition rate. The deposition was realized by moving the build platform (substrate) while the deposition head was always stationary. For diffraction experiments, the x-ray beam on the sample was 100 µm (H) × 30 µm (V). The x-ray beam was aimed at the mushy zone of the melt pool to monitor the structure fluctuation during the deposition process. The dynamic diffraction patterns were analyzed using the software *GSAS II* [96].

The *operando* optical imaging of the DED process was carried out in the lab using a high-speed camera (Photron FASTCAM Nova S9) with a NIR lens (Navitar Resolv4K). The pixel resolution of NIR images was 10 µm, and the frame rate was 1 kHz. The software *ImageJ* [95] was used to process the images.

4.2.6 Crystal plasticity simulation

In order to explore the effect of texture evolution on the distinct plastic flow behavior in samples cut along BD, the elastic-viscoplastic self-consistent (EVPSC) model was employed. It was initially developed by Molinari *et al*. [109,110] and recently extended by Wang *et al*. [111] to account for large strain deformation and arbitrary crystal structures. The EVPSC model employed in the present work was initially coded by Christopher Calhoun [112] and further developed by Jishnu Bhattacharyya to incorporate the dislocation density based on the hardening law introduced by Beyerlein and Tome in 2008 [113]. The overall strain rate was additively decomposed into an elastic and a viscoplastic component. The elastic response was modeled using Hooke's law, while the viscoplastic response was described by a slip system-level viscoplastic flow rule: $\dot{\gamma}^{\alpha} = \dot{\gamma}_0 \left|\frac{\tau^{\alpha}}{\tau_c^{\alpha}}\right|^n sgn(\tau^{\alpha})$ [114]. The stress exponent, *n*, was set to 20, to overcome the "ambiguity problem" of slip system selection [115,116]. The reference strain rate $\dot{\gamma}_0$ was set equal to the global straining rate enforced in the experimental tests (1×10^{-3} s^{-1}), which eliminated the effect of this rather high stress exponent on the overall flow stress, as suggested by [117].

The plastic deformation of FCC 316L SS was accommodated by the octahedral slip mode, {111} <110>. The extended Voce empirical hardening rule was used to describe the evolution of critical resolved shear stress (CRSS) of the slip systems of this mode, τ_c^{α} : $\tau_c^{\alpha} = \tau_0^{\alpha} + (\tau_1^{\alpha} + \theta_1^{\alpha}\Gamma)\left(1 - exp\left(-\Gamma\frac{\theta_0^{\alpha}}{\tau_1^{\alpha}}\right)\right)$, where $\Gamma = \sum_{\alpha}\gamma^{\alpha}$ is the accumulated shear strain in a grain; τ_0^{α} is the initial threshold stress; $\tau_0^{\alpha} + \tau_1^{\alpha}$ is the saturation stress; and θ_0^{α} and θ_1^{α} are the initial and final strain hardening rates, respectively. The strength increment due to strain hardening occurred via a hardening matrix, $h^{\alpha\beta}$, according to $\Delta\tau^{\alpha} = \frac{\partial\tau_c^{\alpha}}{\partial\Gamma}\sum_{\beta} h^{\alpha\beta}\Delta\gamma^{\beta}$, where $\partial\Gamma = \sum_{\beta}\Delta\gamma^{\beta}$. A latent hardening coefficient of 1.0 was employed since there was not sufficient experimental evidence to justify employing a more complex description for the present case. Several interaction schemes such as Secant, Affine, Tangent and the n^{eff} interaction (where, $1< n^{eff} < n$, the viscoplastic power law exponent) have been used to linearize the single-crystal viscoplastic constitutive rule in order to control the stiffness of the grain-matrix interaction [118–120]. The Secant and the Tangent result in the stiffest and the most compliant interactions, respectively, while the Affine and the n^{eff} interaction leads to intermediate grain-matrix interaction, where, for the latter, smaller values promote stiffer interaction [121]. In this work, $n^{eff} = 10$ was used.

In order to simulate the constitutive response of the Bi and the Wig sample, the polycrystal was represented as a collection of 2000 orientations with volume fractions representing the experimentally measured initial texture of the two materials. Uniaxial tension along the build direction was simulated by imposing straining increments of 5×10^{-4} parallel to the loading direction at a rate consistent with the experimental testing rate of 1×10^{-3} s^{-1}, while the shear strains were set to zero. The normal stresses along the two directions perpendicular to the loading axis were also set to zero. The initial CRSS τ_0^α and the hardening parameters θ_0^α, θ_1^α and τ_1^α of the octahedral slip mode were fitted to the experimental BD tensile flow curve of the Bi sample. The best-fit values are shown in Table 4.1. These same parameters were used to predict the stress-strain response of the Wig sample. The predicted flow curves were then compared to the experimental stress-strain data.

Table 4.1: *Best-fit Voce parameters for BD tension of the Bi sample. All values are in MPa.*

Slip mode	$\boldsymbol{\tau_0^\alpha}$	$\boldsymbol{\theta_0^\alpha}$	$\boldsymbol{\tau_1^\alpha}$	$\boldsymbol{\theta_1^\alpha}$

{111} <110>	120	400	120	100

4.3 Results

4.3.1 Microstructure of as-deposited samples

Figures 4.2a-4.2d show optical images of Bi and Wig samples along SD and TD, respectively. On the SD cross-sectional view (Figs. 4.2a and 4.2c), the melting tracks in both samples show a crescent shape owing to the large overlapping between adjacent tracks. Inset figures in Figs. 4.2b and 4.2d are optical images showing magnified features on the top surface of Bi and Wig samples, respectively. While the Wig deposition strategy did induce waved boundaries between adjacent tracks, it did not significantly elevate the degree of surface roughness. Coarse columnar grains were observed in both Bi and Wig samples, common to DED 316L because of the relatively large melt pool and directional solidification. The inset of Fig. 4.2a offers a closer look at a single-track cross-section, with fusion boundaries highlighted by blues lines. Also marked are three representative positions where the Vickers hardness tests were performed, i.e., the track interior (A), lateral fusion boundary (B), and bottom fusion boundary (C). The Bi and Wig samples exhibit only a small difference in hardness measured at these locations (Table 4.2), which indicates the similarity between the matrix structures of the two samples. The energy-dispersive spectroscopy (EDS) results indicate an elevated concentration of Ni and Cr at the dendritic subgrains and interdendritic boundaries in both samples (Figs. 4.2e and 4.2f). The densities of Bi and Wig samples were measured based on Archimedes' principle, and the results (Table 4.2) indicate a low level of porosity in both Bi and Wig samples and no significant difference between them. The 3D morphologies of representative pores were characterized using the synchrotron μXCT (Figs. 4.2g and 4.2i). Together with the optical microscopy (Figs. 4.2h and 4.2j), the results show that the Bi sample contains lack-of-fusion pores with irregular shapes, commonly observed in DED samples [122,123], whereas the pores observed in the Wig sample are mostly spherical. The present work was unable to perform statistical analysis on the morphology of pores over a large number of pores owing to the high density of these samples.

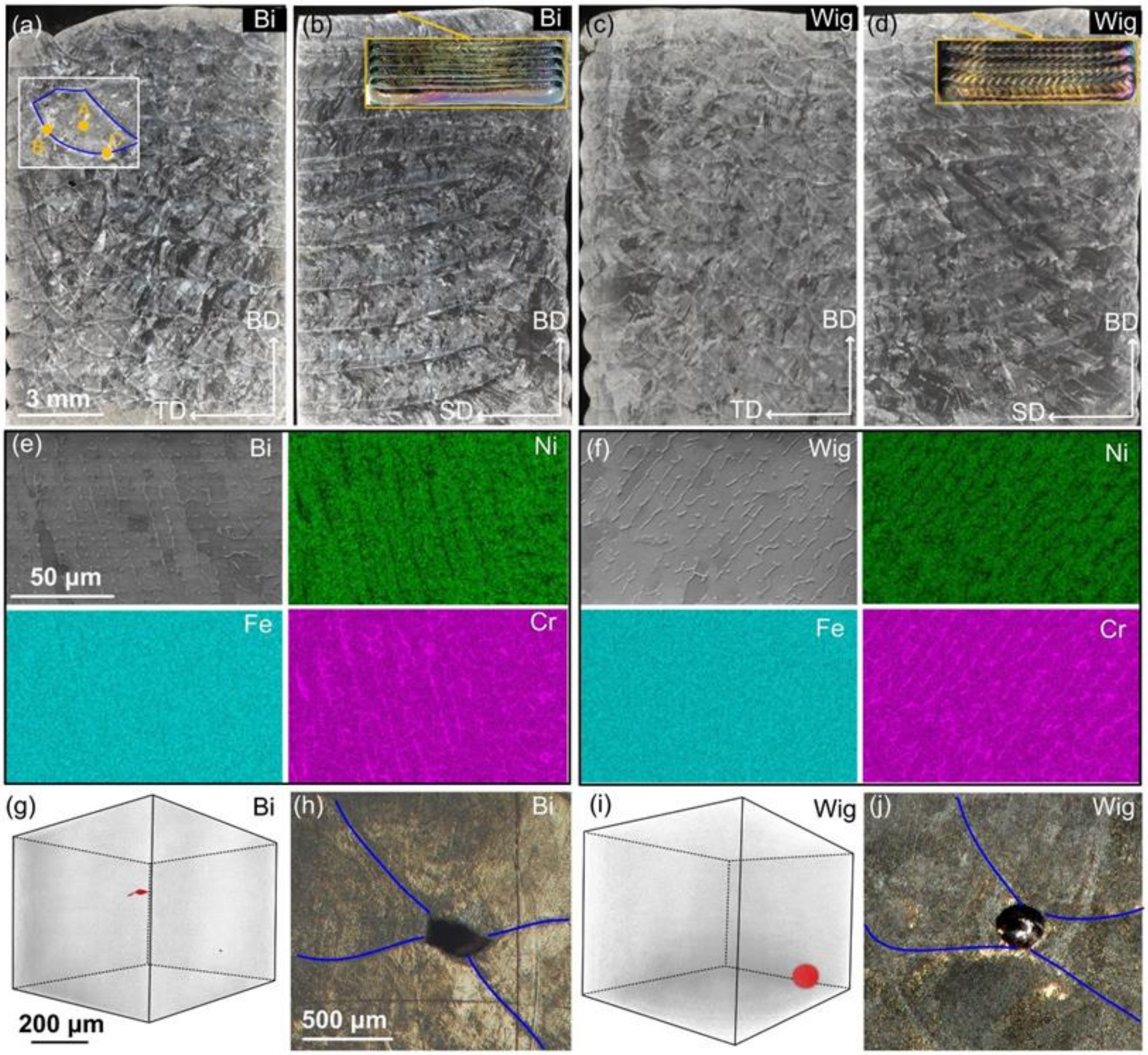

Figure 4.2*: (a-d) Optical microscopy images showing coarse columnar grains on SD and TD planes of Bi and Wig samples. The inset images in (b) and (d) consist of corresponding optical images showing the surface of as-deposited samples. (e, f) SEM and EDS of as-deposited samples revealing element segregation at subgrain boundaries. (g, i) Synchrotron µXCT with a perspective view and (h, j) optical microscopy characterizing pore defects in as-deposited samples. The fusion boundaries are marked in blue lines in optical images. Scale bars in (a), (e), (g), and (h) are applied for the Bi and Wig samples.*

***Table 4.2**: Hardness and density of the as-deposited Bi and Wig samples.*

Strategies	**Data**	**Micro Vickers Hardness (Hv)**			**Density (%)**
		A position	**B position**	**C position**	
Bi	Average	192.44	188.98	195.46	99.26
	Standard deviation	3.76	2.76	7.11	0.11
Wig	Average	194.68	190.14	196.64	99.29
	Standard deviation	1.70	3.74	4.56	0.10

The grain morphology and texture at the central locations in Bi and Wig samples were analyzed using SEM-EBSD. Figure 4.3a shows an inverse pole figure (IPF) map for the SD plane of the Bi sample. The approximate positions of interlayer and lateral fusion boundaries are marked by yellow and white dashed lines, respectively. Large columnar grains on a millimeter scale appear in each deposition layer, roughly aligned with the building direction and perpendicular to the lateral fusion boundary. The epitaxial growth of columnar grains can be observed on the interlayer and lateral fusion boundaries. The corresponding kernel average misorientation (KAM) map (Fig. 4.3b) indicates subgrain boundaries with small misorientation angles in coarse columnar grains, and these boundaries are arbitrarily distributed throughout the entire sample. The inverse pole figures (IPFs), pole figures (PFs), and orientation distribution function (ODF) sections of the Bi sample are presented in Figs. 4.3c-4.3e. The as-deposited Bi sample exhibits a strong cube texture with a significant volume fraction of material having <100> crystal directions parallel to the three sample directions, i.e., SD, TD, and BD, in the deposition coordinates.

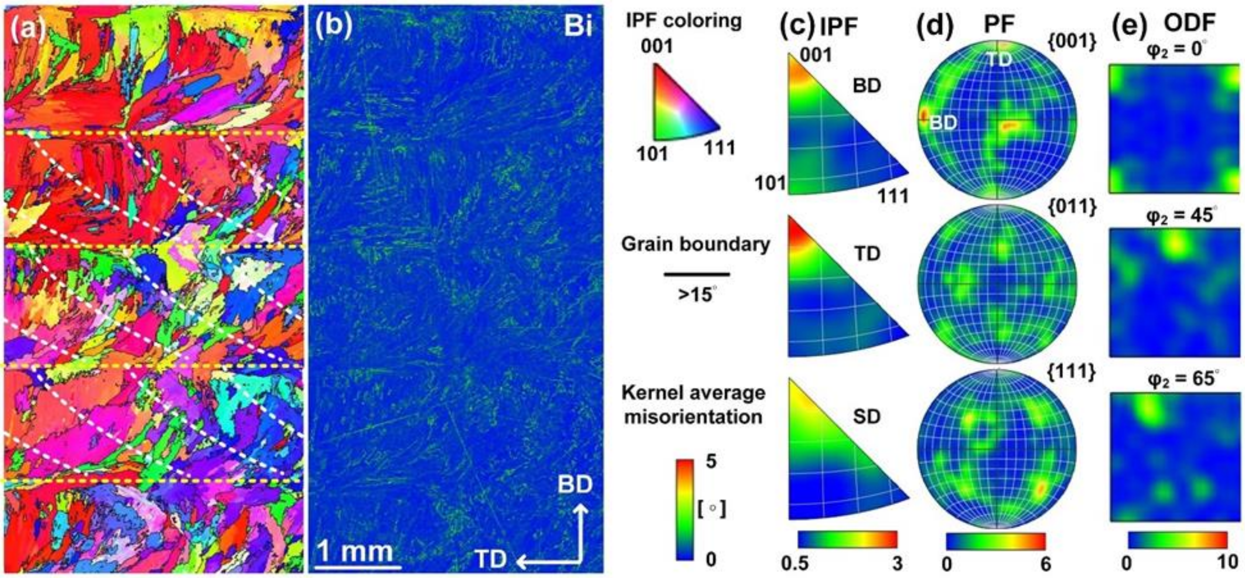

***Figure 4.3**: EBSD (a) IPF and (b) KAM maps on the SD plane of the as-deposited Bi sample and corresponding (c) IPF, (d) PF, and (e) ODF analyses.*

The EBSD maps for the SD plane of the as-deposited Wig sample are shown in Fig. 4.4. The Wig sample exhibits grain size and morphology similar to the Bi sample. The coarse, columnar grains with preferred orientation and the substructure within some grains are also observed in the Wig sample. Epitaxial growth occurs across layers and between adjacent deposition tracks. Figure 4.4b is the corresponding KAM map that depicts subgrain boundaries within coarse grains. The IPF, PF, and ODF sections are shown in Figs. 4.4c-4.4e, respectively. Different from the cube texture in the Bi sample, strong <111> alignment occurs along the scanning direction, and there is also a somewhat lower tendency for a near-TD orientation of a related <111> fiber. (Note that <111> directions are 70.53 degrees away from each other.)

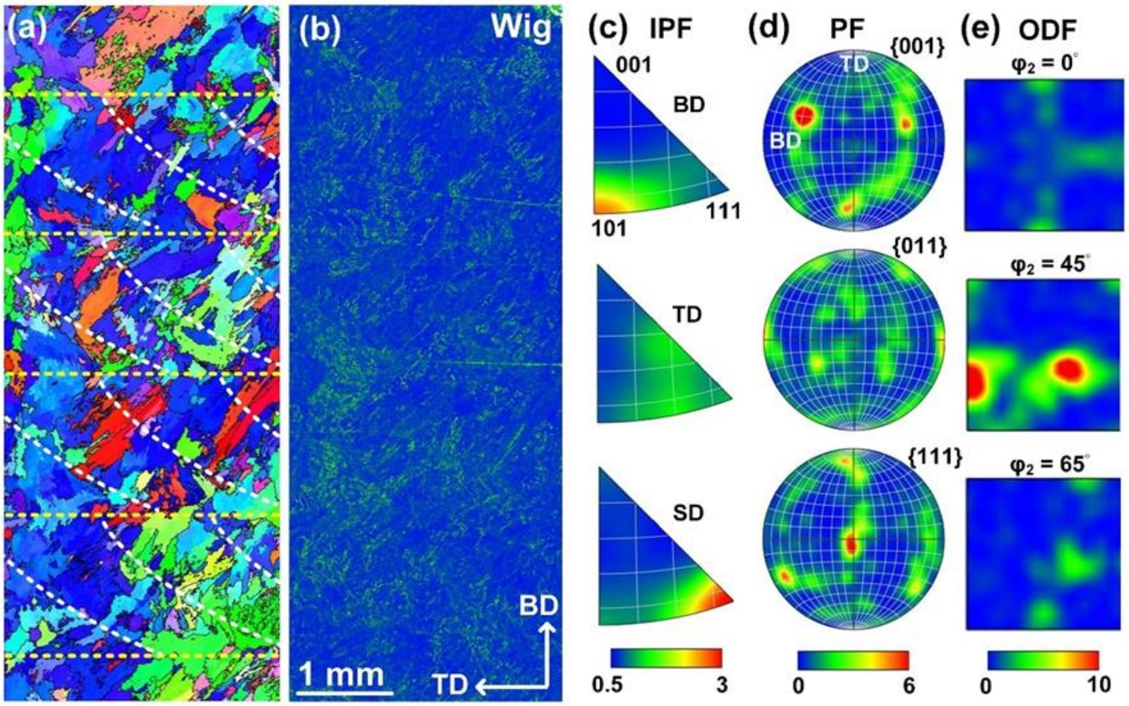

Figure 4.4*: EBSD (a) IPF and (b) KAM maps on the SD plane of the as-deposited Wig sample and corresponding (c) IPF, (d) PF, and (e) ODF figures.*

4.3.2 Investigation of the DED process

To unravel the formation mechanism of the unique texture in the Wig sample, an *operando* high-speed NIR imaging experiment was carried out during the Bi and Wig single-track deposition processes along both SD and TD directions. The positions and angles of laser beams (marked in

Fig. 4.5a) can be identified by the hot spots on the melt pool surface and by the vapor plume scattering of the emitted light. When applying the Bi scanning strategy, the melt pool is relatively stable during deposition. Viewed relative to SD, the melt flows outward from the gap between two front hot spots, as depicted by the yellow arrows in Fig. 4.5a. A similar flow pattern can be observed along TD (Fig. 4.5e), though the melt stream flowing towards the front of the melt pool constantly impacts the back-flowing stream. By contrast, the melt pool in the Wig deposition process appears asymmetric and more dynamic, and the melt flow becomes unstable due to the small transverse displacement during scanning. The Wig deposition track does not present a zig-zag shape but appears to be a continuous line. Constantly changing scanning direction causes the melt pool to wobble around the laser beams. This wobbling could alter laser absorption as the incidence angle influences laser reflectance. Keeping the deposition track as a straight line while inducing melt pool wobbling is the main reason for applying the specific wiggle pattern illustrated in Fig. 4.1d.

Based on the relative position between the feeding wire and laser exposure, the Wig deposition has three dynamic states occurring periodically (Figs. 4.5b-4.5d). The surface melt flow direction oscillates if viewed against SD. Note that the melt flow was tracked based on the moving trajectories of features on the melt pool surface, e.g., small pieces of impurity phases. Viewed along TD, on the weak laser absorption side (Fig. 4.5f), the melt surface flows primarily from the front to the rear along the melt pool boundary, while on the strong absorption side (Fig. 4.5h), the melt surface flows radially from the hottest spot on the side. At the transient moment when the melt pool is not deflected (Figs. 4.5c and 4.5g), both TD and SD views reveal the same melt flow patterns as those in the stable melt pool under the Bi deposition process.

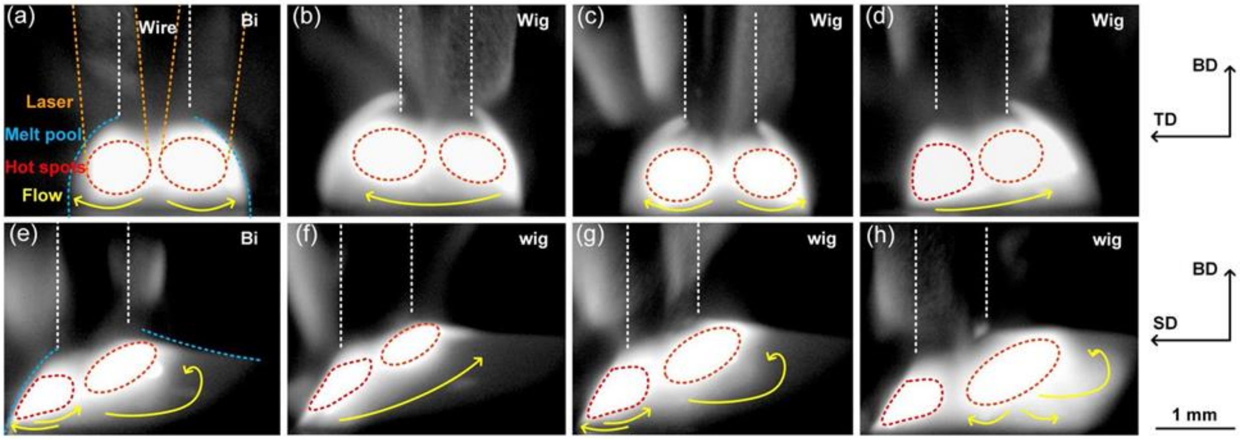

Figure 4.5*: Operando high-speed NIR imaging of the Bi and Wig deposition processes. The scanning-direction (SD) view of the (a) Bi and (b-d) Wig deposition process. The transverse-direction (TD) view of the (e) Bi and (f-h) Wig deposition process. The Bi scanning condition yields a stable melt pool, while the Wig scanning condition results in an oscillating melt pool.*

A multi-physics model was developed to study the laser absorption further and melt pool characteristics for simulating the single-track deposition. The simulations were calibrated and validated against the *operando* NIR imaging result (Fig. 4.5) and the post-characterization of the build track cross-section (insets of Figs. 4.6a and Fig. 4.6a). Figures 4.6a and 4.6b show the temperature distribution on the center plane of the Bi and Wig deposition tracks. Yellow dashed lines mark the liquidus temperature, and the white arrows indicate the melt flow. Figure 4.6c illustrates the history of transverse thermal gradient (G_{TD}) extracted from a specific location close to the liquidus line, as marked with black and blue squares in Figs. 4.6a and 4.6b, respectively. For the Wig process, the location of the analyzed region on the TD is fixed to the center of the printed track. Noticeably, the Wig deposition periodically varies the transverse temperature gradient near the solidification front, which agrees with the melt pool oscillation observed by the high-speed NIR imaging (Figs. 4.5b-4.5d and 4.5f-4.5h). By contrast, the G_{TD} in the Bi deposition process is negligible and only fluctuates weakly. The melt pool boundary was extracted from the simulation data, and the locations of the solidification front at the melt pool surface from 7 frames (with a time interval of 0.02 s) are displayed in Figs. 4.6d and 4.6e. The black, yellow, and blue lines represent the outline of the deposition track, liquidus, and solidus lines, respectively. The positions of the solidus and liquidus lines, relative to the feeding wire location, in the Wig deposition show a more significant fluctuation, indicating a dynamic variation of thermal conditions along the SD during the deposition. In the Wig deposition process, the liquidus and solidus lines at the melt pool surface are still perpendicular to SD.

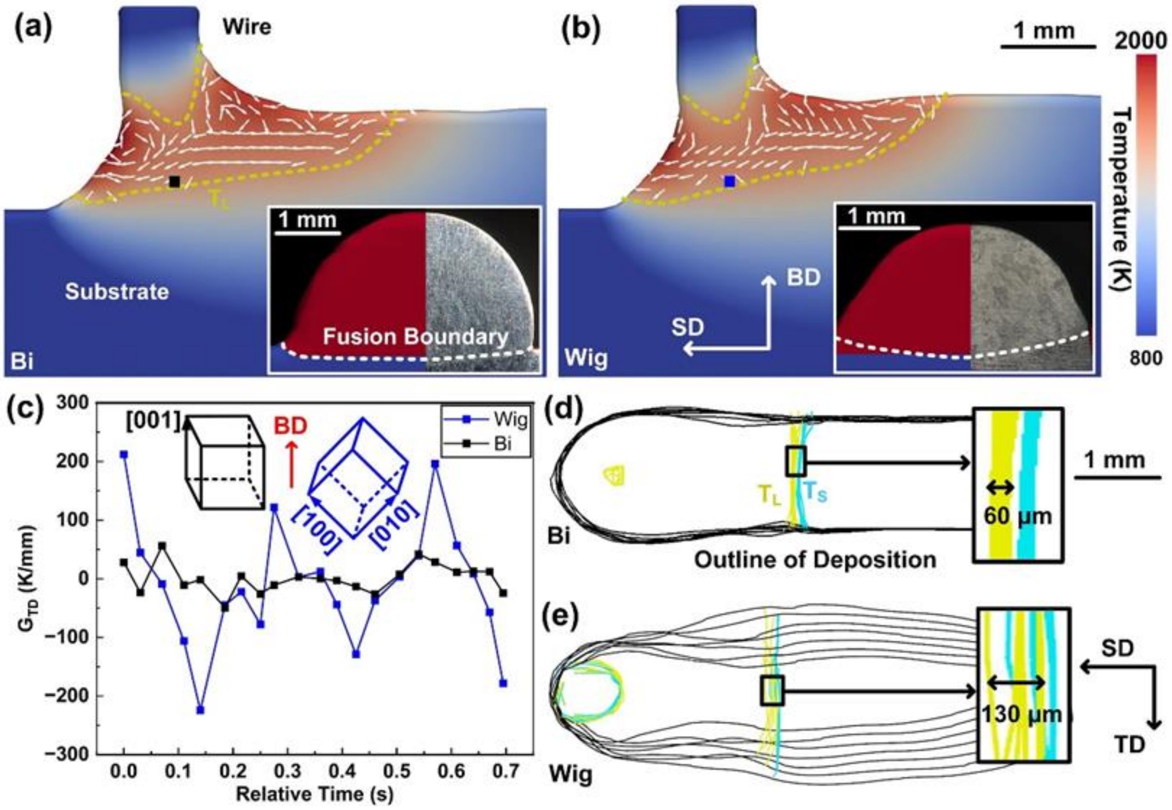

Figure 4.6: *(a-b) Simulations showing the temperature distribution and melt flow at the center plane during the (a) Bi and (b) Wig deposition processes. The inset of (a) shows the comparison between simulated and experimental cross-sections of single-track deposited under the Bi deposition condition. (c) History of thermal gradient* G_{TD} *extracted at the specific positions marked using squares in (a) and (b). (d-e) Position fluctuation of the melt pool extracted from 7 frames with a time interval of 0.02 s. The black, yellow, and blue lines mark the deposition track, liquidus boundary, and solidus boundary, respectively.*

The solidification behavior of 316L SS in Bi and Wig deposition was further investigated via *operando* synchrotron experiment. Figure 4.7a is a representative x-ray image showing the wire-laser DED process. Note the horizontal dark-bright stripes are artifacts induced by imperfect x-ray optics. Since these optical components at the beamline vibrated constantly, flat-field background correction for this x-ray image was not successful. In this experiment, the deposition head was stationary during the entire deposition process. In other words, the position of the melt pool, with respect to the incidence x-ray beam, was fixed. Thus, the stability of solidification behavior could be monitored by the time-resolved diffraction with the x-ray beam probing the mushy zone. The diffraction pattern presented in Fig. 4.7b is a representative frame in a sequence, which presents both diffraction spots from solidified coarse grains and diffusive scattering from the liquid phase. Figures 4.7c and 4.7d are the time-resolved diffraction intensity maps radially integrated from 2D diffraction patterns of Bi and Wig deposition processes, respectively. The discernable diffraction spots from solid phases were masked during the integration; therefore, the broad peak at the Q value of 2.87 Å-1 in the intensity maps primarily corresponds to the liquid phase. The stable melt pool and mushy zone in the Bi deposition process are manifested by the constant peak intensity over time in Fig. 4.7c. By contrast, the fluctuating diffraction peak intensity in Fig. 4.7d suggests a changing volume fraction of solid crystals in the fixed detection volume during the Wig deposition, i.e., the mushy zone moves back and forth along the scanning direction. This fluctuation is consistent with the simulation results shown in Figs. 4.6d and 4.6e. A variation in the melt pool shape typically accompanies such a shift in the rear mushy zone. Thus, except for along the TD, the thermal conditions and solidification behavior along the SD change dynamically during the Wig deposition process.

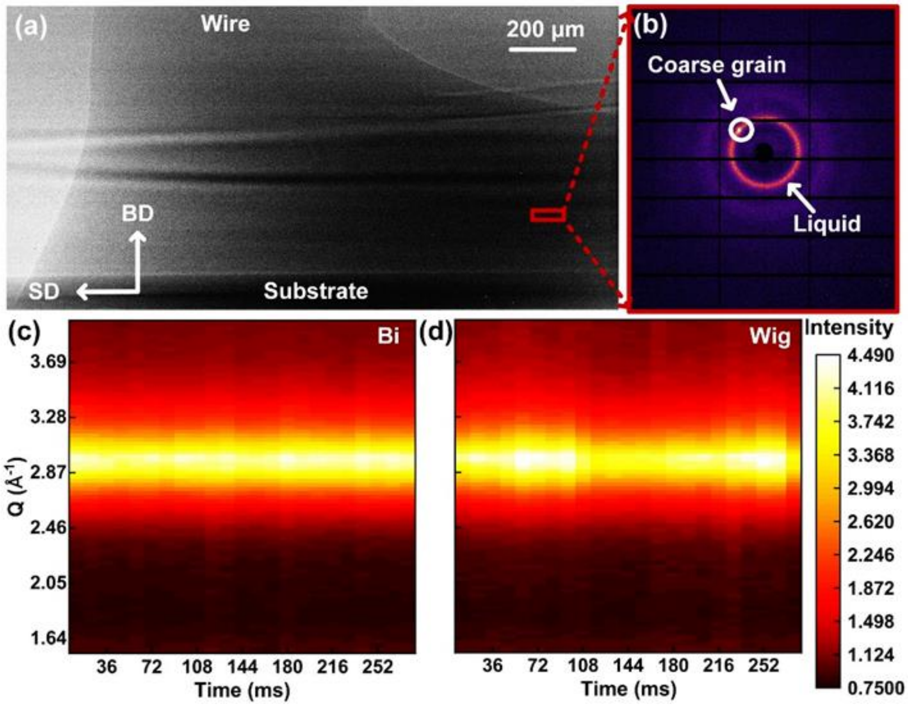

Figure 4.7*: Representative dynamic (a) x-ray image and (b) diffraction pattern of the Bi deposition process. The horizontal dark-bright stripes in (a) are artifacts induced by imperfect x-ray optics. The time-resolved x-ray diffraction intensity maps reveal the variation of the mushy zone constitution in (c) Bi and (d) Wig deposition processes.*

4.3.3 Tensile property and deformed microstructure

Representative tensile curves of Bi and Wig samples loaded along BD are shown in Fig. 4.8a. Notably, the Wig sample exhibits significantly higher ductility than the Bi sample and surpasses most of the reported AM 316L SS samples [124–129] with no compromise in strength. The ultimate tensile strength (UTS) and elongation of samples loaded along different directions are summarized in Fig. 4.8b. The Bi samples yield significant anisotropy in strength and ductility, and the better property was achieved from tensile samples cut parallel to the SD and TD than the BD. This anisotropy is common in DED metals because the structure defects and residual stress affect the mechanical properties more in BD than in other directions [28,34,130]. While the Wig samples still show anisotropy in ductility, the difference in strength along different directions is substantially reduced. Fractography of Bi and Wig tensile samples loaded along BD are shown in Figs. 4.8c-4.8d. The uniformly distributed dimples on the fracture surface indicate a ductile fracture of both samples.

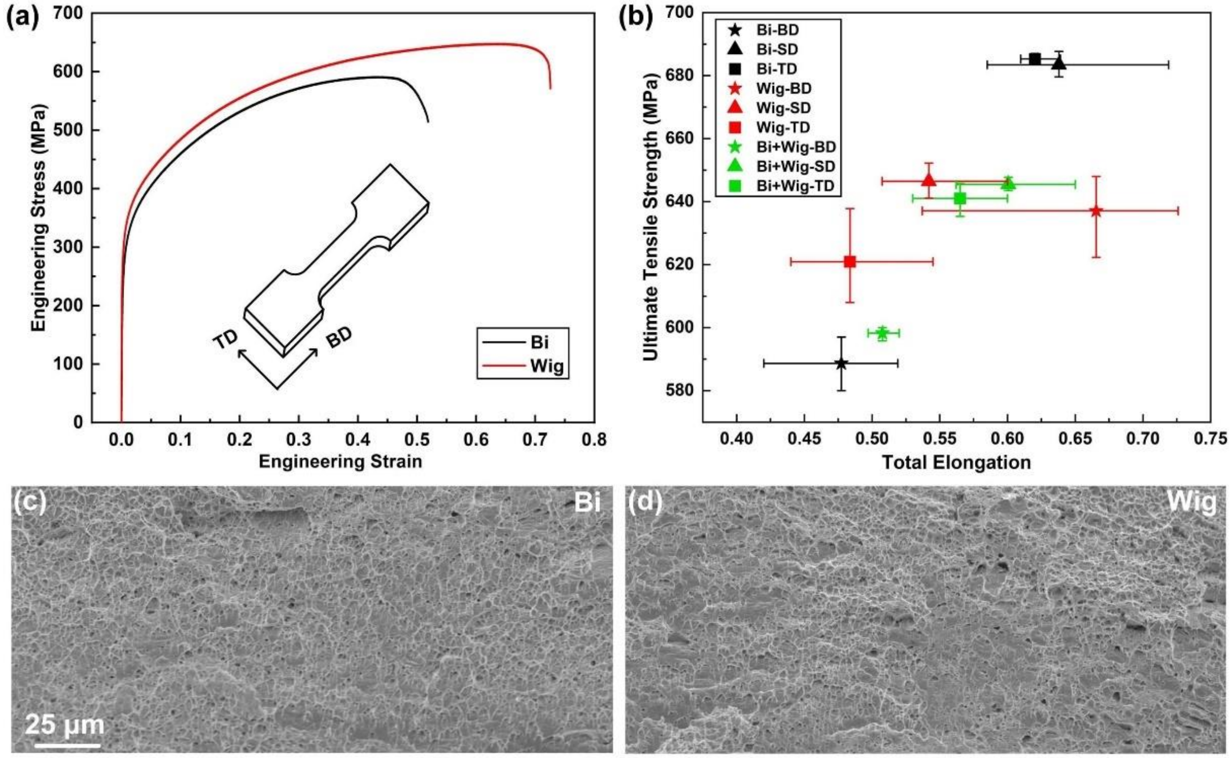

Figure 4.8: *(a) Stress-strain curves of the Bi and Wig samples loaded along the BD. (b) Comparison of tensile properties of Wig and Bi samples cut along three directions. Fractography of the (c) Bi and (d) Wig tensile samples loaded along the BD.*

To further investigate the deformation behavior, the Bi and Wig samples were loaded along BD up to 30% strain, and then the microstructures were characterized by EBSD. Figures 4.9a and 4.9c are representative IPF maps showing the grain morphology in deformed Bi and Wig samples. In both samples, columnar grains tend to further align with the BD since that is parallel to the loading direction. Meanwhile, mechanical twinning is observed in coarse grains. Furthermore, the corresponding KAM maps (Figs. 4.9b and 4.9d) display considerable local misorientation in grains. Higher local misorientation concentrates on the region consisting of smaller grains. The geometry necessary dislocation (GND) density in as-deposited and deformed samples can be calculated from their corresponding KAM maps. Curves in Fig. 4.9e show the distribution function of GND density with an unimodal feature in all samples. The as-deposited Bi (black solid line) sample presents a sharp peak at a low-density level, which mainly results from the boundaries between subgrains within coarse grains (Fig. 4.3b). Due to the inhomogeneous deformation, the GND distribution profile of the deformed Bi sample yields a flatter peak at a high-density level (black dashed line). Moreover, there is no obvious statistical difference in GND between Wig (red lines) and Bi samples.

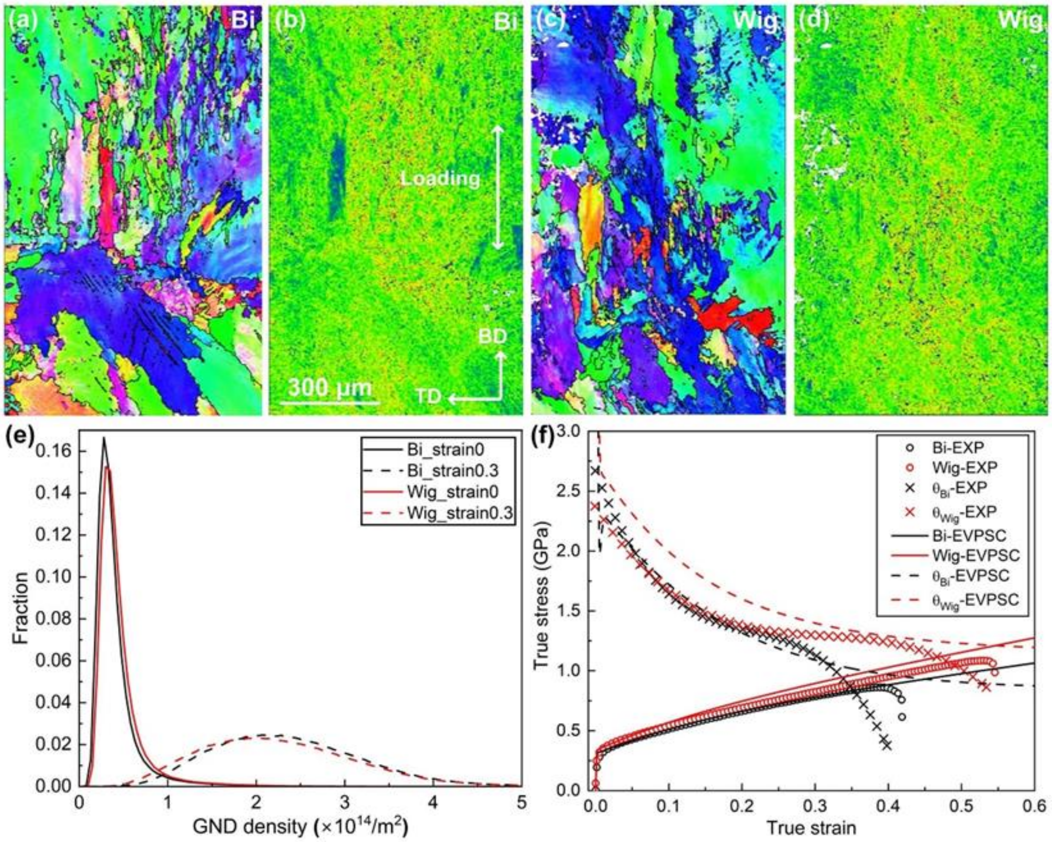

***Figure 4.9**: EBSD IPF maps of deformed (a) Bi and (c) Wig samples and (b, d) corresponding KAM maps. (e) Statistical GNDs of as-deposited and deformed Bi and Wig samples. (f) Experimental and simulated true stress-strain curves and work hardening curves for Bi and Wig samples. EXP and EVPSC refer to experimental and simulated results, respectively.*

Crystal plasticity simulations were performed for the Bi and Wig samples to quantify the effect of texture on the constitutive response. The slip system strain hardening response of the material was fit to describe the Bi sample flow curve using the appropriate initial texture for that sample as an input. Then, the tensile flow curve of the Wig sample was predicted using the same slip system level behavior but beginning with the initial texture that results from the Wig scan strategy. The experimental true stress-strain curves and work hardening rates (θ) obtained from the tensile tests parallel to the build direction (BD) and from the corresponding EVPSC simulations are shown in Fig. 4.9f. There is a good qualitative agreement between the experiment and the simulation. The Wig sample exhibits a higher flow stress and work hardening rate than the Bi sample, and the simulation result captures this trend. The higher strain hardening rate of the Wig sample contributes to delaying plastic instability (when $\theta = \sigma$, according to the Considère criterion). This correlation aligns with the experimentally observed higher uniform elongation in that sample. Although other factors, such as deformation twinning, may influence the stress-strain response, the effect of the initial texture appears to be the dominant factor responsible for the observed differences in tensile strength and ductility between the Bi and Wig samples in BD.

4.4 Discussion

4.4.1 Formation mechanism of fiber texture under the Wig deposition process

In accordance with solidification theories, the temperature gradient (G) and cooling rate (R) play critical roles in defining the nucleation and grain growth behaviors of metals. Owing to the intrinsically high G/R ratio, the growth of coarse columnar grains with preferred crystallographic orientations, rather than the nucleation of refined grains, dominates in the liquid-to-solid phase transformation in the DED process [18,51,131]. The specific type of solidification textures depends on both the surface energy anisotropy of the material system and the maximum temperature gradient during solidification [46,132]. In the deposition process with traditional deposition strategies, such as the unidirectional line scans, the melt flow and temperature gradient inside the melt pool remain relatively stable. In principle, the temperature gradient is mirror-symmetric around the vertical central plane of the melt pool. Owing to the intense heat input and relatively slow printing velocity in DED processing, G_{BD} is higher than the components in SD and TD, making it the controlling factor for solidification. For FCC and BCC crystals, <100> is the preferred crystal growth direction [133]. Therefore, the formation of the cube texture with <100>//BD is most favorable, as observed in the Bi 316L sample and other FCC metals [134].

However, the present Wig deposition strategy introduces an oscillating transversal motion of the melt pool that is believed to alter the preferred growth direction. The *operando* high-speed NIR imaging (Fig. 4.5) and multi-physics modeling (Fig. 4.6) of the Wig deposition indicate a significant instability of melt flow and solidification conditions caused by the dynamic and asymmetric laser absorption. When the melt pool is significantly deflected (Figs. 4.5b, 4.5d, 4.5f, and 4.5h), the G_{TD} increases dramatically and becomes asymmetric around the vertical central plane of the melt pool. Therefore, the preferable growth direction shifts to one side under the SD view. As G_{TD} fluctuates periodically (Fig. 4.6c), the maximum temperature gradient constantly oscillates from one side to another during the deposition. As a result, the growth of a coarse columnar grain/subgrain colony is subject to different temperature gradients. Despite the temperature gradient changing smoothly and continuously, solidification during the deposition process is still constrained by the crystal orientation of primary/precursor solidified grains. The solidification growth front, therefore, cannot follow the variation of the temperature gradient, which is reflected by the absence of orderly distributed misorientation in columnar grains (Fig. 4.4). To reach a balance/compromise between the deposition geometry and energetically favorable growth direction, the 316L system may activate the preferential growth along two perpendicular <100> crystal orientations by turns, as sketched in Fig. 4.6c. In this case, coarse columnar grains are still formed and roughly aligned along the building direction but yield a fiber texture with <110>//BD because the subgrain colonies with <110>//BD are always more active than those in other orientations. Pauza et al. simulated such grain growth behavior using Monte Carlo Potts modeling and demonstrated the high sensitivity of texture structure to local thermal gradient and melt pool morphology [47]. In addition, the dynamic thermal conditions in the SD direction, as suggested by the *operando* x-ray diffraction in Figs. 4.7c and 4.7d, can induce fluctuation of the rear mushy zone and slightly tilt the favorable growth direction on the TD plane (in the SD). As a consequence, a nearby <111> orientation tends to develop along the SD direction in the as-deposited Wig samples (Fig. 4.4c).

4.4.2 Effects of crystallographic texture on mechanical properties and anisotropy

As-deposited DED samples are subject to significant anisotropy of mechanical properties, which intrinsically results from the elongated grain morphology, oriented defects, crystallographic texture, and microstructure heterogeneity [34]. As supported by the crystal plasticity simulation (Fig. 4.9f), the texture in Wig samples is beneficial in increasing the work hardening rate when deformed along the BD, thereby enhancing the strength and ductility. For the Bi samples, the cube crystallographic texture exerts a minimum influence on mechanical anisotropy due to the similarity in preferred crystal orientations along the three loading directions (SD, TD, and BD). The enhanced mechanical properties observed in the SD and TD can be attributed to microstructural heterogeneities, e.g., heterogeneous grain size distribution. The observed level of mechanical anisotropy is very common in DED 316L SS samples. However, the presence of a fiber texture results in a distinct mechanical anisotropy in Wig samples. As a result, Wig samples present better mechanical properties (both UTS and elongation) than Bi samples when loading along the BD. In both the SD and TD, conversely, Bi samples present higher ultimate tensile strength and better elongation compared to the Wig samples. Previous research reported the positive effects of fiber texture on improving the strength and ductility of 316L SS [135]. A similar mechanical anisotropy in the AM 316L SS featuring fiber texture has been observed. In addition, because of the similar grain morphology, micro-hardness, and GND accumulation in Bi and Wig samples, it can be concluded that the specific crystallographic texture is the key factor responsible for their distinct mechanical anisotropy. Given the easy adoption and reliable effects, the Wig deposition strategy opens a new opportunity to design and customize complex large-scale structural components, e.g., alternatively applying Bi and Wig deposition across layers or at different locations of the part. To further examine this possibility, another batch of DED samples was fabricated with alternative Bi and Wig deposition layer by layer, named “Bi+Wig.” As summarized in Fig. 3.9b, the Bi+Wig deposition yielded better homogeneity (particularly for ductility) in samples cut along three directions without much compromise in overall properties, if compared with Bi and Wig samples. This effect is attributed to pitting the distinct anisotropies of the Bi and Wig layers against one another.

4.4.3 Advantages of wiggle deposition

The Wig deposition can generate a unique solidification texture in 316L SS. Since in-plane texture (i.e., SD and TD direction) can be readily controlled by changing the scanning direction during the build process, the capability of modifying the BD texture, enabled here by the Wig deposition, becomes significant. The present work confirms the feasibility of altering the solidification texture and mechanical anisotropy in the wire-laser DED of 316L SS by controlling the stability of the melt pool. As demonstrated above, a certain degree of melt pool instability can be induced by alternating the transversal component of scanning. This Wig deposition strategy is expected to open up many exciting opportunities for programming the microstructure and properties of as-printed materials. For example, by changing the frequency (or characteristic length scale) of wiggling, a variety of texture structures could be obtained. Also, synergistically and alternatively applying the Bi and Wig depositions at different positions of the build can achieve a single part with locally varied structures and properties.

Compared with reported approaches for changing solidification texture and mechanical property, the additional overhead for implementing the Wig deposition strategy in current commercial DED systems is very low. It involves only small modifications of the control system and computer code for deposition. Applying the wiggle strategy may slightly reduce the effective SD traveling velocity and the cooling rate during printing. However, neither larger grains nor more secondary phases were observed in the as-printed Wig sample, compared with the Bi sample. A higher scanning velocity can be set when adopting the Wig strategy for materials whose grain structures are sensitive to cooling rate. Therefore, the Wig deposition is promising to be widely applied in the wire-laser DED process for customizing large-scale components.

In addition to the solidification texture, the Wig deposition strategy may also modify the morphology of lack of fusion (LOF) pores. In a wire DED process, LOF pores, formed between melt tracks, typically have irregular shapes (Figs. 4.2g and 4.2h). However, the LOF pores in the Wig sample are mostly spherical (Figs. 4.2i and 4.2j). It is speculated that the melt pool wobbling and dynamic melt flow might manage to remelt the LOF pores generated in the previous track and allow the surface tension to work the pores into spherical shapes. In the present work, the impact of pore shape on the tensile properties of Bi and Wig samples is not evident, as both samples exhibit low porosity. Additionally, the gauge regions of all tensile samples were inspected using an optical microscope before loading to ensure they were defect-free at the sample surface. Moreover, the fractography of both samples did not reveal any structural features associated with defect-induced cracking. For dense samples, the spherical-shaped pores are less detrimental to other mechanical performance, such as fatigue, since the stress can easily concentrate around irregular-shaped pores and lead to an early failure of materials [136].

The Wig deposition strategy introduced here demonstrated not only the benefits of direction independence in coaxial wire feeding but also the tremendous potential of the dynamic melt pool to control the microstructure and performances of DED samples. Even though this work only presents the results of the wire-laser DED process, no fundamental limitations would impede the implementation of the same operation in other wire-based AM processes, such as wire arc AM and wire-feed electron beam melting. The thermal conditions and solidification behaviors of these AM processes are not drastically different from the wire-laser DED. In terms of alloy systems, because their melt flow dynamics and solidification behaviors can be very different, specific processing conditions for producing specific crystallographic textures in particular materials need to be explored. Lastly, to better understand the mechanisms by which the solidification textures are formed and gain full control over the microstructure, more sophisticated modeling (e.g., coupling phase field with multi-physics modeling) would be extremely helpful.

4.5 Conclusion

This work introduced a wiggle deposition strategy for the wire-laser DED of 316L SS, which involved an alternating transversal component of scanning. Through *operando* NIR imaging, synchrotron x-ray diffraction, and multi-physics simulation, it was found that the resulting wobbling motion of the melt pool induced asymmetric laser absorption and thereby led to highly dynamic melt flow and complex thermal conditions inside the melt pool. Consequently, a specific solidification texture in samples was generated, which differed from those built with the conventional deposition pattern (e.g., bi-directional scanning). The tensile loading experiment revealed that both the Bi and Wig samples exhibited superior ductility and satisfactory ultimate tensile strength; however, they presented distinct mechanical anisotropy in samples cut along SD, TD, and BD. Crystal plastic simulation verified that the Wig BD sample, with its specific fiber texture, demonstrated a higher flow stress and work hardening rate compared to the Bi sample. This characteristic could delay plastic instability within the Wig sample, consequently leading to higher ductility. In the field of laser AM, the community believes that a stable melt pool is desirable for assuring build consistency and avoiding structure defects. However, the Wig deposition strategy described here challenges this traditional wisdom by suggesting that a certain degree of melt pool instability can be utilized to directly modify the solidification texture and thereby control the mechanical properties.

5. Atomic structure of melt pool and its evolution during the rapid solidification in metal additive manufacturing

According to the new understanding gained from the previous research chapters about the wire-laser directed energy deposition (DED) process, this work focuses on an "abnormal" columnar-to-equiaxial transition (CET), an attractive but controversial topic raised recently in the metal additive manufacturing (AM) field. This chapter conducted a comprehensive measurement of the processing map to investigate the occurrence of this "abnormal" CET in the wire-laser DED of Inconel 718. Based on existing theory, the microstructural features in the "abnormal" CET region obtained in the wire-laser DED of Inconel 718 agree with the hypothesis of icosahedral-short-range-ordering (ISRO)-mediated nucleation. To investigate this hypothesis further with solid evidence, this work employed operando synchrotron x-ray diffraction and corresponding total-scattering analysis for wire-laser DED processes under different printing conditions. This advanced characterization first revealed the atomic structure of the melt pool and its evolution during the rapid solidification in metal AM. By incorporating multi-physics simulation, the "abnormal" CET formation mechanism in metal AM has been explained and clarified.

5.1 Introduction

An "abnormal" CET and the hypothesized ISRO-mediated nucleation theory recently attracted significant attention in metal AM [53]. As explained in Chapter 1.6, this CET phenomenon was considered "abnormal" due to the unique solidification structure in this region, e.g., the five-fold symmetry among neighboring grains, and its inconsistency with conventional CET knowledge. This emerging finding is promising to be manipulated for producing metallic samples with refined microstructure, weak crystallographic texture, and superior performance [137]. However, the current perspectives on ISRO-mediated solidification have only been derived from the ex-situ characterization and post-analysis of as-printed samples. Hence, whether the ISRO-mediated solidification takes effect in AM is still debatable. In other words, it remains uncertain whether the "abnormal" CET in AM processing is induced by ISRO in the liquid phase or by other factors. In addition, the existing understanding of atomic clusters in the melt pool is primarily derived from the traditional solidification of liquid melts. However, the solidification behavior in AM processing is more complex than the equilibrium solidification. Various factors, including intense melt flow, a heterogeneous temperature field, constitutional supercooling, and rapid solidification, challenge the hypotheses and conclusions proposed for the ISRO-mediated nucleation theory. Besides, there is still a lack of a comprehensive investigation of the "abnormal" CET in metal AM, thereby failing to illustrate the correlation between printing conditions/printing behaviors and the occurrence of "abnormal" CET in metal AM. As a consequence, many conclusions raised for the ISRO-mediated solidification in metal AM might be inconsistent. As reported by previous works [55,60], for example, ISRO-mediated solidification led to equiaxed grains in DED samples but was also responsible for the elongated grains in LPBF samples. A more systematic investigation is necessary to reconcile these contradictions, incorporating advanced *operando* characterizations and integrating multi-physics simulations for additional support.

5.2 Methods

5.2.1 Printing process and sample preparation

The single-track printing of Inconel 718 alloy was executed using a commercial DED system (Additec μPrinter). The specification of this DED system and the printing procedure can be found in Chapter 2.1. The feedstock used for the printing is a commercial Inconel 718 wire with a 0.9 mm diameter. The deposition substrates are Inconel 718 strips with a dimension of 3.6 (Thickness) × 5.1 (Width) × 18 (Length) mm^3. Wire feeding rate (F), traveling/scanning speed (V), and total laser power (P) are the major variables for the printing process. The corresponding linear energy density (LED) and volumetric energy density (VED) were calculated according to eq. 1.2 and eq. 1.3, respectively. Given the three-fold symmetry of the laser distribution in this DED system, the printing direction described in Fig. 2.5 is defined as the default printing direction. The shielding gas, high-purity Ar, was active during the entire printing process. The detailed printing parameters of the three representative printing conditions are summarized in Table 5.1.

Table 5.1: *Three representative printing conditions applied for the wire-laser DED process of Inconel 718. The detailed parameters of these three printing conditions are summarized.*

Conditions	***P* (W)**	***V* (mm/s)**	***F* (mm/s)**	***LED* (J/mm)**	***VED* (J/mm^3)**
Lack of Fusion	400.0	10.0	17.0	40.0	37.0
Transitional	600.0	5.8	29.0	103.4	32.6
Normal	600.0	6.7	11.4	89.6	82.7

The post-characterization of as-printed samples, including optical imaging and scanning electron microscopy, and the procedure of sample preparation are described in Chapter 2.4.

5.2.3 *Operando* synchrotron x-ray characterization and PDF extraction

Operando synchrotron x-ray imaging and diffraction were conducted at the 1-ID-E beamline of Advanced Photon Source at Argonne National Laboratory. More details about the experiment setup and conditions are described in Chapter 2.3. For the high-energy x-ray diffraction employed in this study, the size of the x-ray beam on the sample was reduced to 50 μm (H) × 30 μm (V) to achieve a higher spatial resolution.

Following the procedure of data analysis described in Chapter 2.3, the raw x-ray images collected by the imaging detector were processed to optimize the background using *ImageJ* [95]. The radial integration of the diffraction patterns was performed using the *GSAS II* software [96]. The instrumental parameters, e.g., detector distance, were extracted from the diffraction data of a standard CeO_2 sample. The dead pixels on the diffraction patterns had been masked out before the integration. Pair distribution function (PDF) profiles were extracted using the software *PDFGetX2* [138]. The entire procedure incorporating the diffraction integration and PDF extraction is explained step by step as follows.

1. As described in Chapter 3, each *operando* x-ray diffraction data set covers the entire printing process, including 2000 frames of diffraction patterns. In the total-scattering analysis of each data set, 330 frames of scattering patterns corresponding to the statuses “before printing” and “stable printing period” were extracted from the entire sequence of scattering patterns. The scattering patterns belonging to the “stable printing period” were

designated as the sample data. In the dataset labeled “before printing,” the scattering from the sample was absent , which was used to measure the scattering background from the container (referring to the laser protection glasses shown in Fig. 2.4a). In addition, the instrument background was acquired through an additional diffraction measurement without the sample and laser protection glasses. It is important to note that the continued collection of 330 frames corresponds to the 1.32 seconds of printing. Then, summarization and integration were carried out for each data set using *GSAS-II*.

2. The 1D scattering profile was input in *PDFGetX2* for the PDF extraction. The scattering background from the instrument and containers was deducted from the scattering data profile. The x-ray attenuation across the Inconel 718 sample was calculated according to the following equation

$$\frac{I(z)}{I_0} = e^{-(\rho \sum_j w_j \mu_j) z} \qquad \text{eq. 4.1}$$

where ρ, w_j, μ_j, z refers to the density of Inconel 718, mass fraction of element j, mass attenuation of element j, and the thickness of the sample.

3. The ratios of each background term were evaluated based on the x-ray energy, sample thickness, and sample composition. Then, these ratios were subjected to fine-tuning based on the shape of the 1D scattering profile at the low wavevector (*Q*).
4. After the background correction, the 1D scattering intensity profile (*I(Q)*) was converted to the total-scattering structure function (*S(Q)*) and reduced pair distribution function (*G(r)*).

The detailed mathematics are described by eq. 1.4 and eq. 1.5. The Q range used for the PDF extraction was from 0.82 to 14.82 Å^{-1}.

5.2.2 Small-box fitting of *G(r)*

The small-box fitting was applied to analyze the measured *G(r)* using the software *PDFgui* [139]. The instrumental parameters, *Qdamp* and *Qbroad*, were obtained from the refinement associated with the calibrant. Several atomic models, including FCC-Crystal, FCC-MRO, ICO-MRO, and ICO-SRO, were used as input for fitting the *G(r)* profiles measured during the *operando* experiments. The isotropic Gaussian atomic displacement parameter (ADP), scale factor, linear atomic correlation factor δ_1, and lattice parameters were refined for each phase and atomic clusters within the *r* range from 1 to 80 Å. The fraction of each structure can be calculated through the fitted scale factors.

The term FCC-Crystal refers to the FCC solid phase with the space group of Fm-3m, indicating the unmelted wire and the solidified phase. In the *G(r)* component of the solid phase FCC-Crystal, sharp peaks extend to the high-r range, distinguishing the solid phase from the atomic orders in the liquid phase.

FCC-MRO represents the FCC-like medium-range ordering (MRO) in the liquid phase. Its structure information was extracted from the corresponding FCC solid phase, but an additional variable *spdiameter*, was refined specifically to account for the attenuation of peak amplitude resulting from the limited cluster size. Apart from this shape-damping function, the FCC-MRO *G(r)* component shows broad peaks and different "lattice parameters" compared to those of the

FCC-Crystal phase. The peak broadening is associated with a significant ADP value, consistent with the liquid nature of FCC-MRO. In the raw diffraction pattern, FCC-MRO and FCC-Crystal are associated with diffusive scattering and Bragg diffraction, respectively. Although the atomic model of FCC-MRO input in the refinement was created based on the FCC crystal phase, the large ADP value refined in the PDF analysis for FCC-MRO elucidates the significant atomic deviation of this atomic ordering in the liquid phase. For such a liquid ordering, the refined parameters of FCC-MRO, such as the "lattice parameters," only indicate the average information of its structure.

The ICO-MRO and ICO-SRO indicate icosahedral MRO and icosahedral short-range ordering (SRO) in the liquid phase. As there is no crystal structure corresponding to these two types of orders, their input atomic models were generated using a Matlab code [140]. This code allows the modification of the cluster size by increasing or decreasing the number of FCC shells. The *PDFgui* underestimates the packing density of such atomic clusters because this software considers the input atomic clusters as the unit cells of corresponding crystals. To address this issue in the refinement of icosahedral MRO and SRO, a composite modeling approach [141] was adopted. The size of the ICO-MRO was fitted by manually testing the refinement with different numbers of FCC shells instead of using the parameter *spdiameter*. The *G(r)* components of ICO-MRO and FCC-MRO present different peak positions due to the different configurations of atomic pairs. Therefore, these two orders can be accurately distinguished in the refinement, even though both display broad peaks. In contrast to these MROs, the ICO-SRO consists of only 13 atoms and fewer atomic pairs. It was assigned to refine more randomly arranged atoms in the liquid phase and provided larger separation distances between atoms. The refinement of ICO-SRO is the final step in the PDF analysis, and this structure only represents a low fraction among all fitted phases and liquid clusters.

It should be noted that this refinement only considered the topological ordering in liquid. The chemical order was assumed to have less effect on *G(r)* due to the near-identical scattering cross-section of the principal elements in Inconel 718 when interacting with high-energy x-rays. Another source of uncertainty arises from the crystallographic texture of solidified columnar grains, particularly notable in the Normal printing condition. The preferred orientation slightly influences the relative height of individual peaks. For this purpose, the PDF refinement was not performed for the late solidification stage. The model agreement scores for all refinements fall within the range of $8.0\% < Rw < 15.1\%$, indicating excellent reliability and logical model selection in the present PDF analysis. It should be noted that *Rw* refers to the standard deviation between the fitted and experimental profiles. Error bars were determined for the fraction of each fitted structure based on the 10% deviation from the *Rw* value.

5.3 Results

5.3.1 Processing map of the “abnormal” CET in the wire-laser DED of Inconel 718

To get a comprehensive insight into the solidification microstructure, especially the occurrence of “abnormal” CET, of Inconel 718 alloy fabricated by wire-laser DED, single-track printing was conducted under different printing conditions. The variation of solidification microstructures with critical printing parameters, including laser power (*P*), traveling speed (*V*), and wire feeding rate (*F*), are summarized in Fig. 5.1. A 3D processing map shown in Fig. 5.1a was generated, displaying the correlation between the occurrence of “abnormal” CET and the critical printing parameters.

The failure deposition marked on the processing map refers to an unstable printing process generating apparent printing defects such as wire stubbing or dipping. The successfully printed samples were divided into three categories, namely "Lack of Fusion," "Transitional," and "Normal," based on their solidification microstructures. Optical images of the three representative microstructures are shown in Figs. 5.1b-5.1d. The cross-section of the Normal sample (Fig. 5.1d) is dominated by coarse columnar grains, which is commonly observed in WAAM and wire-laser DED samples. However, for the scenario of Lack of Fusion (Fig. 5.1c), the insufficient energy input resulted in the formation of Lack-of-Fusion cracks. Above the crack, a large area of finer equiaxed grains can be observed on the central bottom region of the cross-section. However, the Transitional microstructure (Fig. 5.1b) refers to an intermediate state between the Lack of Fusion and Normal conditions. The Lack-of-Fusion cracks were not observed, but finer equiaxed grains were still generated at a similar region. The detailed comparison of those solidification microstructures is illustrated in the later section of this chapter. The specific parameters of the three representative printing conditions are summarized in Table 5.1.

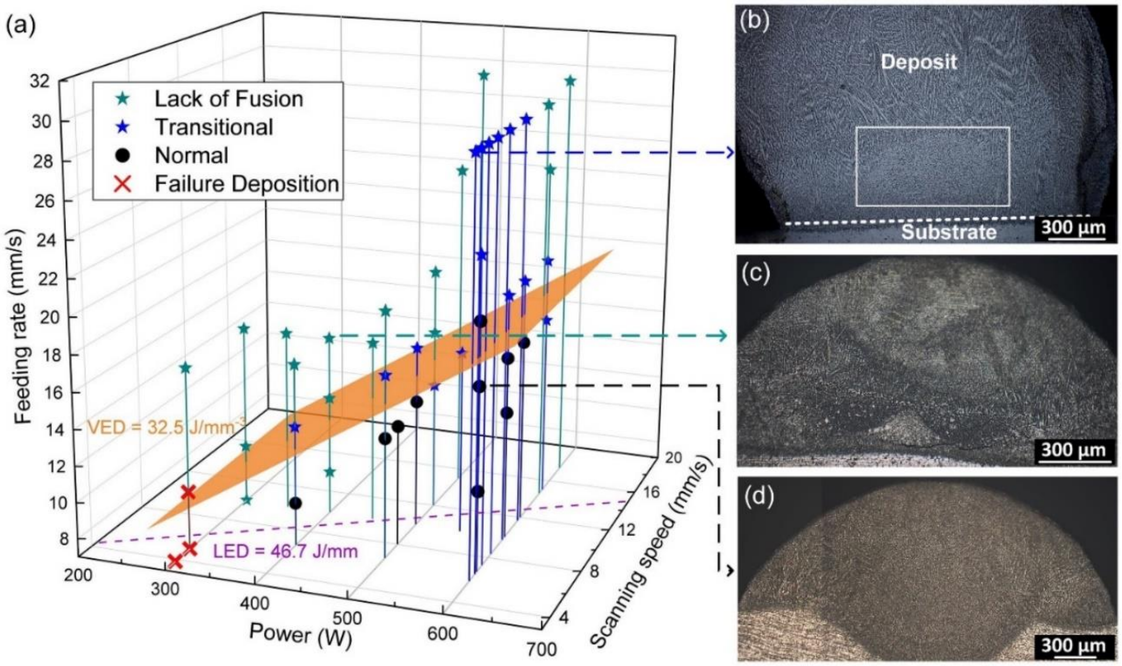

***Figure 5.1**: The 3D processing map of the wire-lase DED of Inconel 718. The variation of grain morphology with critical printing conditions, including laser power, scanning speed, and wire feeding rate, is presented. The yellow plane represents the constant VED of 32.5 J/mm^3. The purple dashed line is the projection of the constant LED plane of 46.7 J/mm on the power-scanning speed plane of the processing map. The representative solidification microstructures of (b) Transitional, (c) Lack of Fusion, and (d) Normal samples are displayed by corresponding optical images.*

To better understand the effect of printing conditions on grain morphology, linear energy density (LED) and volumetric energy density (VED) are introduced to quantify the energy input of different printing conditions. The mathematical definitions of LED and VED are presented by eq. 1.2 and eq. 1.3, respectively. The constant VED of 32.5 J/mm^3 presents as a 2D plane filled with orange in the 3D processing map. The purple dashed line is the projection of the constant

LED plane of 46.7 J/mm on the power-scanning speed plane. The 3D processing map (Fig. 5.1a) illustrates that the Lack of Fusion microstructure results from insufficient energy input, dominating the low-power region with $P < 400$ W. However, as P increases, the Normal and Transitional microstructures appear, and the constant VED plane arbitrarily highlights the boundary between these zones. A lower VED is more conducive to generating Transitional and Lack of Fusion microstructures. Additionally, the constant LED establishes another boundary separating different microstructures in the 3D processing map. The processing zone for the Transitional condition expands with LED increasing, i.e., increasing P but decreasing S. The above observation suggests that both VED and LED play critical roles in forming equiaxed grains in the wire-laser DED of Inconel 718.

5.3.2 Detailed characterization of as-printed samples

The formation of equiaxed grains in Lack of Fusion and Transitional samples is mainly attributed to the "abnormal" CET because such tiny grains are not commonly observed in as-printed DED samples. A more detailed characterization was conducted for all three samples. Figure 5.2a is a magnified view of Fig. 5.1c, presenting the cross-section of a Lack of Fusion sample. A long crack, i.e., the Lack-of-Fusion crack, lies horizontally and is close to the deposit-substrate interface, as pointed out by red arrows in Fig. 5.2a. A band region consisting of equiaxed grains is observed just above that crack. However, there is a variation in contrasts within this band region. Specifically, a fan-shaped region at the center exhibits a brighter contrast. This observation indicates the presence of microstructure heterogeneity within the band region and implies two different formation mechanisms of equiaxed grains. In addition to the Lack-of-Fusion crack, this contrast variation is another feature distinguishing Lack-of-fusion and Transitional samples. Figure 5.2b is the EBSD inverse pole figure (IPF) map of the band region consisting of equiaxed grains. The color scheme of the EBSD-IPF map indicates different crystal orientations of grains, further highlighting the band region consisting of equiaxed grains. Dashed circles labeled B-1 and B-2 distinguish the bright and dark regions in the optical image Fig. 5.2a. Through a direct comparison, grains in the B-2 regions exhibit more irregular morphologies and more non-uniform sizes compared to those in the B-1 region. Pole figures corresponding to the grains in these two regions are extracted and shown in Fig. 5.2c. In contrast to the strong crystallographic texture in the B-1 region, the crystal orientations of equiaxed grains in the B-2 regions exhibit a more random distribution. This difference in crystallographic texture helps distinguish the equiaxed grains originating from the unmelted wire and those formed during solidification.

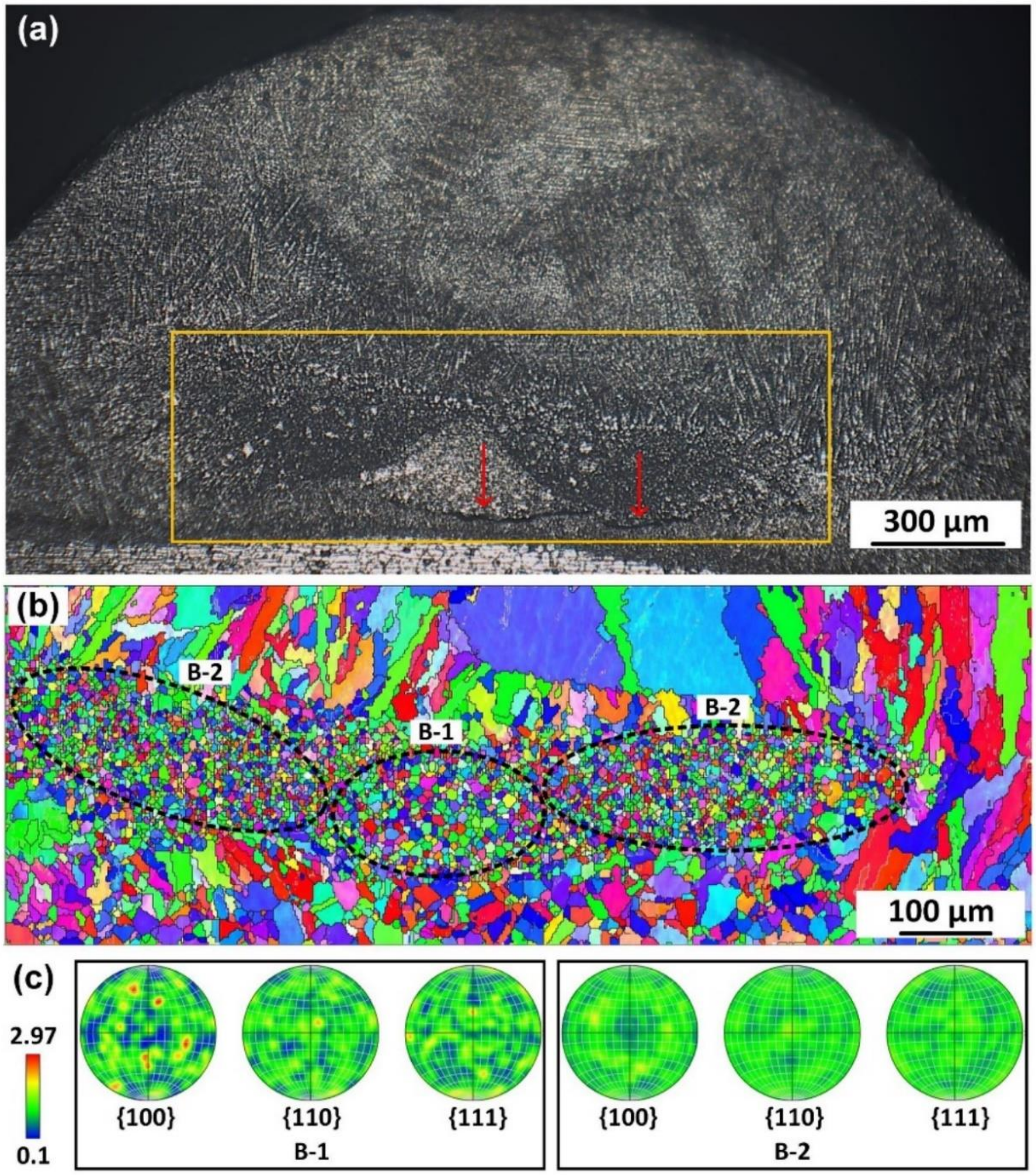

Figure 5.2*: The detailed characterization of the Lack of Fusion sample. (a) The magnified image of Fig. 5.1c. Red arrows point out a long Lack-of-Fusion crack lying horizontally in this sample. (b) The EBSD IPF map corresponding to the region marked by an orange rectangular in figure (a). (c) The pole figures extracted from the grains in the B-1 and B-2 regions that are marked in (b).*

EBSD characterization was also conducted for the other two samples, namely the Transitional and Normal samples. Figure 5.3a is the EBSD IPF map depicting the grain refinement region in the Transitional sample. The characterization region is marked in the original optical image Fig. 5.1b. In this sample, the area of the grain refinement region approximates 900 μm (width) × 300 μm (height) and is located ~100 μm above the deposit-substrate interface. The equiaxial grains within this region are less than 20 μm in size and exhibit relatively random orientation. Excluding this grain refinement region, the printed track is composed entirely of coarser columnar grains. Figure 5.3b is a counterpart of Fig. 5.3a, highlighting the twinning boundaries and random grain boundaries. Within the grain refinement region, abundant twinning boundaries, represented by red, are observed. In addition, the five-fold symmetry was found among several neighboring grains numbered from 1 to 5 in Fig. 5.3c. The white, instead of red, represents the twinning boundaries for improved visualization. The {110} and {111} pole figures of these five grains are displayed in Fig. 5.3d. The crystal orientations corresponding to individual grains are identified by the color of the number marked on the grains in Fig. 5.3c. As shown in the {110} pole figure, there is a twinning relationship between neighboring grains, which is also evidenced by the white twining boundaries between neighboring grains shown in Fig. 5.3c. The blue arcs indicate the common {111} planes between neighboring grains. These common {111} planes all rotate along a common <110> axis (i.e., the five-fold symmetry axis marked by the dashed circle in Fig. 5.3d). The rotation angle of common {111} planes between each neighboring grain pair is approximately 71°, e.g., the common {111} planes between the grain pairs 2-3 and 3-4. In the {111} pole figure, the common {111} planes between neighboring grains and the five-fold symmetry are also revealed by the overlapping pole figures of neighboring grains and their distribution with rotational symmetry, respectively. These features agree with the established theory relevant to the "abnormal" CET in metal AM and the ISRO-mediated nucleation [55].

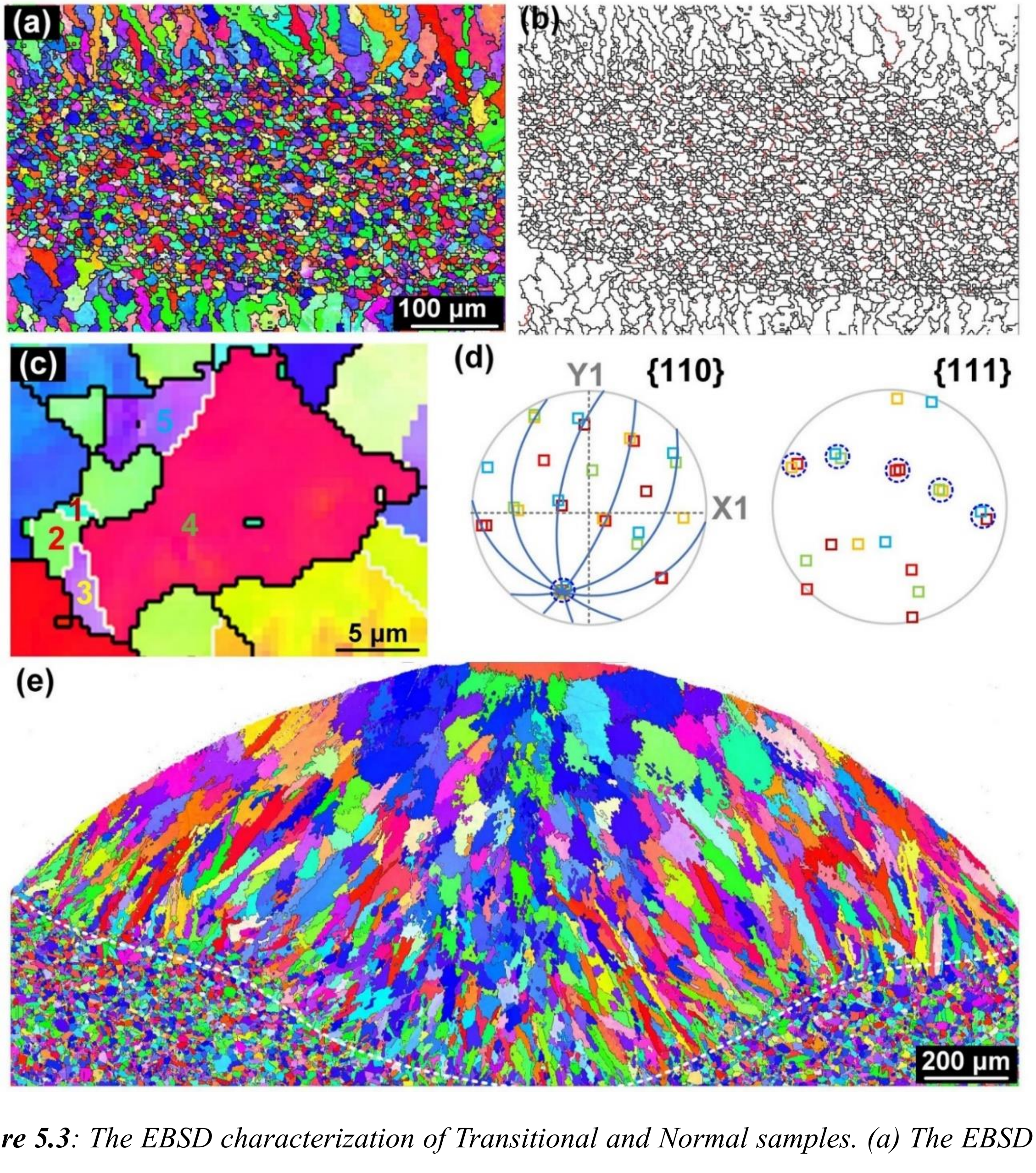

***Figure 5.3**: The EBSD characterization of Transitional and Normal samples. (a) The EBSD IPF map of the transitional sample, corresponding to the region marked by the rectangular in Fig. 5.1b.*

(b) The distribution of random grain boundaries and twinning boundaries in (a). The high-angle grain boundary between grains with random and twinning relationships are marked by black and red colors, respectively. (c) A magnified region in (a) with the twinning boundaries depicted by the red color. (d) the pole figure of the five grains number 1-5 marked in (c). (e) The EBSD IPF map of a Normal sample, a copy of Fig. 3.8c in Chapter 3. The white dashed curve outlines the fusion boundary.

The EBSD characterization of a Normal sample is shown in Fig. 5.3e. Coarse columnar grains are the dominant feature in the cross-section of the printed track. The deep melting depth into the substrate suggests a higher energy input under this printing condition. Furthermore, it is essential to note that the suppression of columnar grain growth investigated in Chapter 3 is irrelevant to the "abnormal" CET because of the absence of both small equiaxed grains and abundant twinning boundaries.

5.3.3 *Operando* x-ray characterizations

To better understand the printing processes and reveal underlying mechanisms regarding the "abnormal" CET, *operando* synchrotron x-ray characterizations were carried out for the wire-DED processes of Inconel 718 under different printing conditions. A detailed description of the experiment setup can be found in Chapter 2.3. The explanation of diffraction mapping and data interpretation are included in Chapter 3. The *operando* synchrotron x-ray characterizations of the

Lack of Fusion printing are presented in Fig. 5.4. Note that all the imaging and diffraction data presented here correspond to the stable printing period. Compared with other conditions, the Lack of Fusion printing adopted a low laser power, leading to limited energy input (both LED and VED). In the x-ray imaging (Fig.5.4a), a rough melt pool front was formed owing to insufficient melting. For the diffraction mode, the monochromatic x-ray beam was focused and probed at different locations marked in Fig. 5.4a. In this way, the microstructure of the melt pool can be resolved spatially. Figures 5.4b-5.4h are representative diffraction patterns collected during the stable printing process with the x-ray probed at different locations. A coordinate system was adopted to specify the location of each measurement, with the center of the wire and the substrate surface defined as the origin in the X and Y directions, respectively. Both sharp diffraction rings and diffuse scattering are observed at the position underneath the wire feeding (Fig. 5.4b), specifically when X = 0 mm. This observation indicates that the wire feedstock did not fully melt upon insertion into the melt pool. With X increases to 1.5 mm, sharp diffraction rings still exist, but their intensities decrease slightly due to the further melting. At the positions farther away from the laser, i.e., X = 2.7 mm (Fig. 5.4g) and X = 4.0 mm (Fig. 5.4h), the diffusive scattering becomes weak, indicating the occurrence of solidification. More and brighter diffraction spots appear, which suggests the formation of coarse grains. During solidification, the sharp diffraction rings still appear on the diffraction pattern, and their intensity slightly increases. This observation provides evidence that, under this printing condition, a portion of the wire did not fully melt throughout the printing process; additionally, new equiaxed grains also formed during the solidification process.

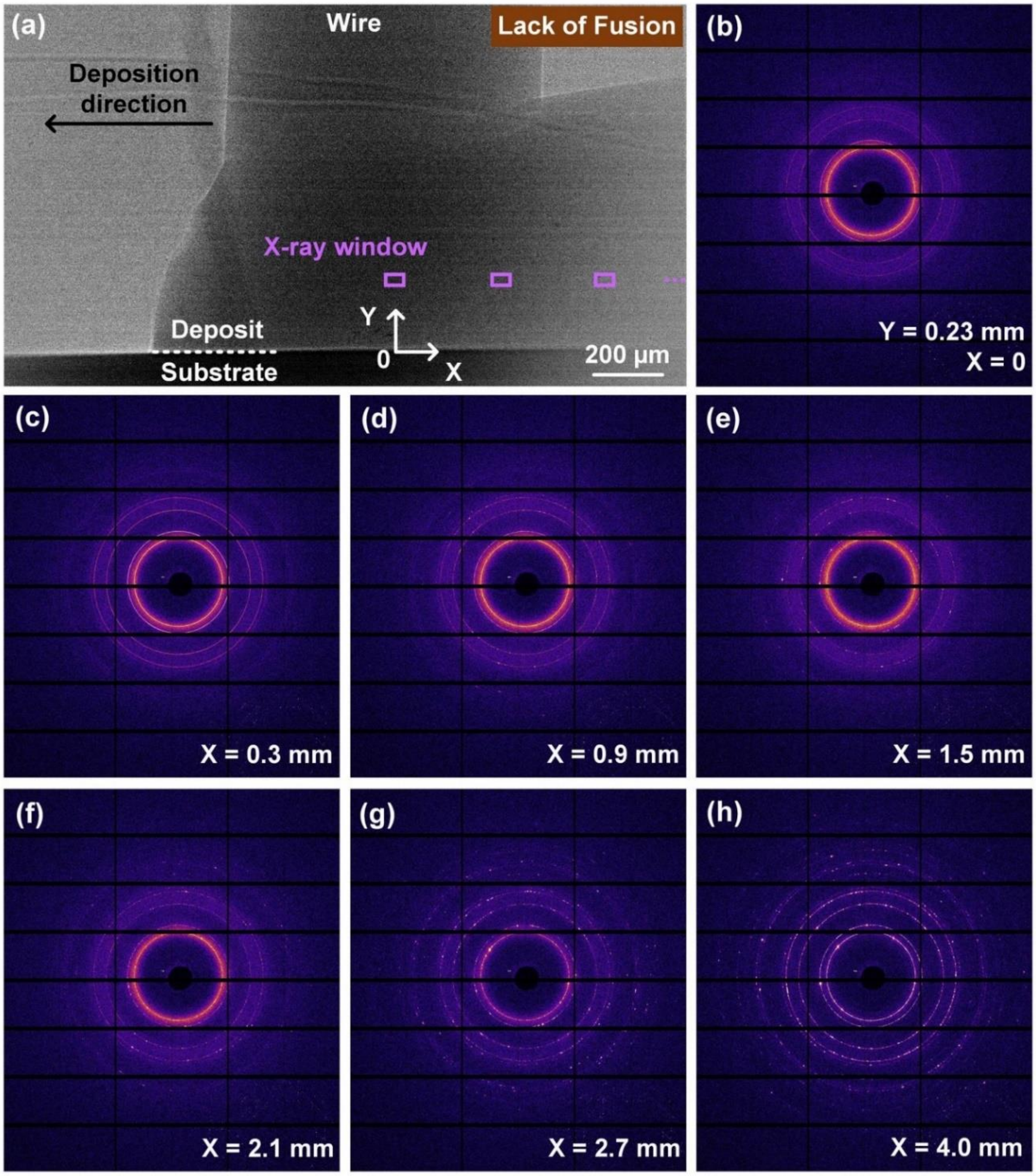

Figure 5.4*: The operando synchrotron x-ray characterizations of the Lack of Fusion printing. (a) x-ray imaging of the printing process. Purple rectangles in Figure (a) define the detection regions of diffraction experiments. (b-h) Representative diffraction patterns collected from different regions of the melt pool during the stable printing period. The coordinates of x-ray probing location are noted at the lower right corner of each subfigure. The center of the wire and the*

substrate surface are defined as the origin in the X and Y directions of the coordinates, respectively.

The *operando* characterization of the Normal printing is shown in Fig. 5.5, and Fig. 5.5a is the x-ray imaging of the stable printing process. In contrast to the rough melt pool front in the Lack of Fusion printing, the melt pool front here is flat and smooth. The wetting angle with respect to the substrate is approximately 47º. The diffraction mapping shows that only the diffusive scattering was detected at the location of X = 0 (Fig. 5.5b). The absence of diffraction rings indicates that the wire rapidly melted as it fed into the melt pool. The pure liquid region continuously extends until X = 2.4 mm. After that, bright and isolated diffraction spots appear, corresponding to the generation of coarse grains during solidification. The distribution of the diffraction spots concentrates at certain azimuth angles, which indicates the strong crystallographic texture in the as-printed sample. The microstructure evolution observed here is consistent with the majority of wire-based AM processes.

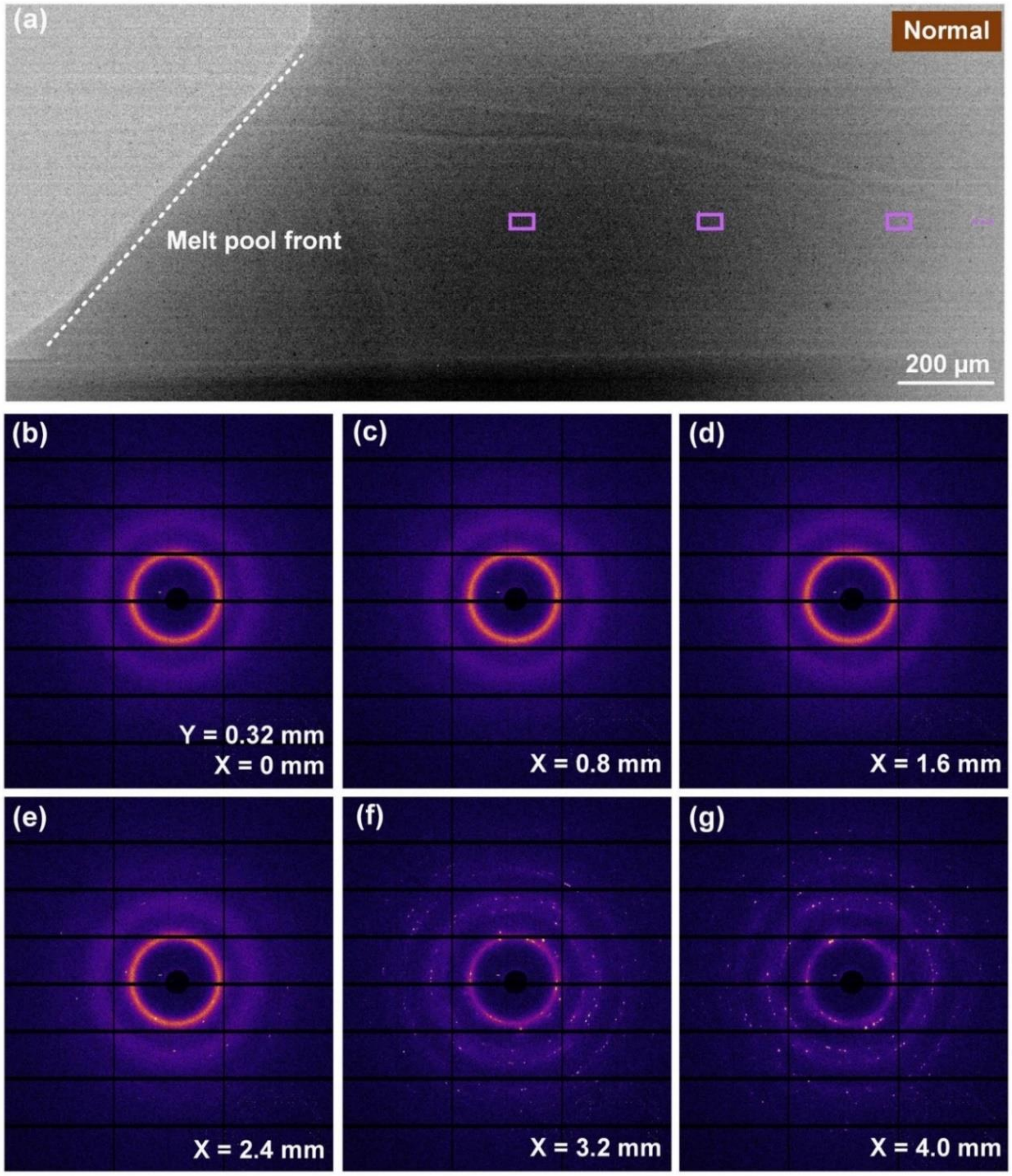

Figure 5.5*: The operando synchrotron x-ray characterizations of the Normal printing. (a) X-ray imaging of the stable printing process. Purple rectangles in Figure (a) define the characterization regions in diffraction experiments. (b-g) Representative diffraction patterns collected from different regions of the melt pool during the stable printing period. The coordinate system adopted in Fig. 5.4 is applicable here.*

Figure 5.6 displays the *operando* characterization corresponding to the Transitional printing condition. It should be noted that this *operando* characterization adopted the opposite printing direction, defined as “Transitional-R” here, while all other parameters are identical. The reason for introducing the opposite printing direction is that, according to the post-characterization, the samples printed along the opposite direction formed a larger CET region than the default printing direction. This difference might be attributed to the special energy distribution of the three lasers, which slightly vary the printing behavior in different directions. Thus, the printing condition Transitional-R is believed to be a more representative comparison with other printing conditions, making the following analysis more convincing. Given the reversion of the printing direction, the x-ray image of Transitional-R shown in Fig. 5.6a was flipped horizontally to avoid confusion. Because of the significant wire feeding rate, a larger melt pool was generated and slightly exceeded the field of view. A flat and smooth melt pool front was formed, as marked by a dashed line on the image, which is similar to the Normal printing (Fig. 5.5a). A series of diffraction experiments was conducted, as shown in Figs. 5.6b-5.6g. Similar to the Lack of Fusion printing (Fig. 5.4), the wire did not fully melt under the Transitional-R printing condition and was subsequently transported inside the melt pool. At position X = 0.9 mm (Fig. 5.6c), sharp diffraction rings remained visible, while their intensities were notably weak. However, the sharp diffraction peaks disappeared at X = 1.2 mm. After that, diffraction rings presented again, accompanied by the emergence of isolated diffraction spots, starting at X = 1.8 mm. In contrast to the Lack of Fusion printing, the solid wire in the Transitional-R printing was only able to survive temporarily in the melt pool but fully melted before the solidification process. There is a narrow region (< 0.9 mm) only consisting of liquid between the unmelted wire tip and the solidification front of the rear melt pool. At the end of the characterization region, i.e., X = 3.9 mm, sharp solidification rings are visible, which differs from the Normal printing (Fig. 5.5g). This observation confirms the occurrence of “abnormal” CET during the solidification under the Transitional-R printing condition.

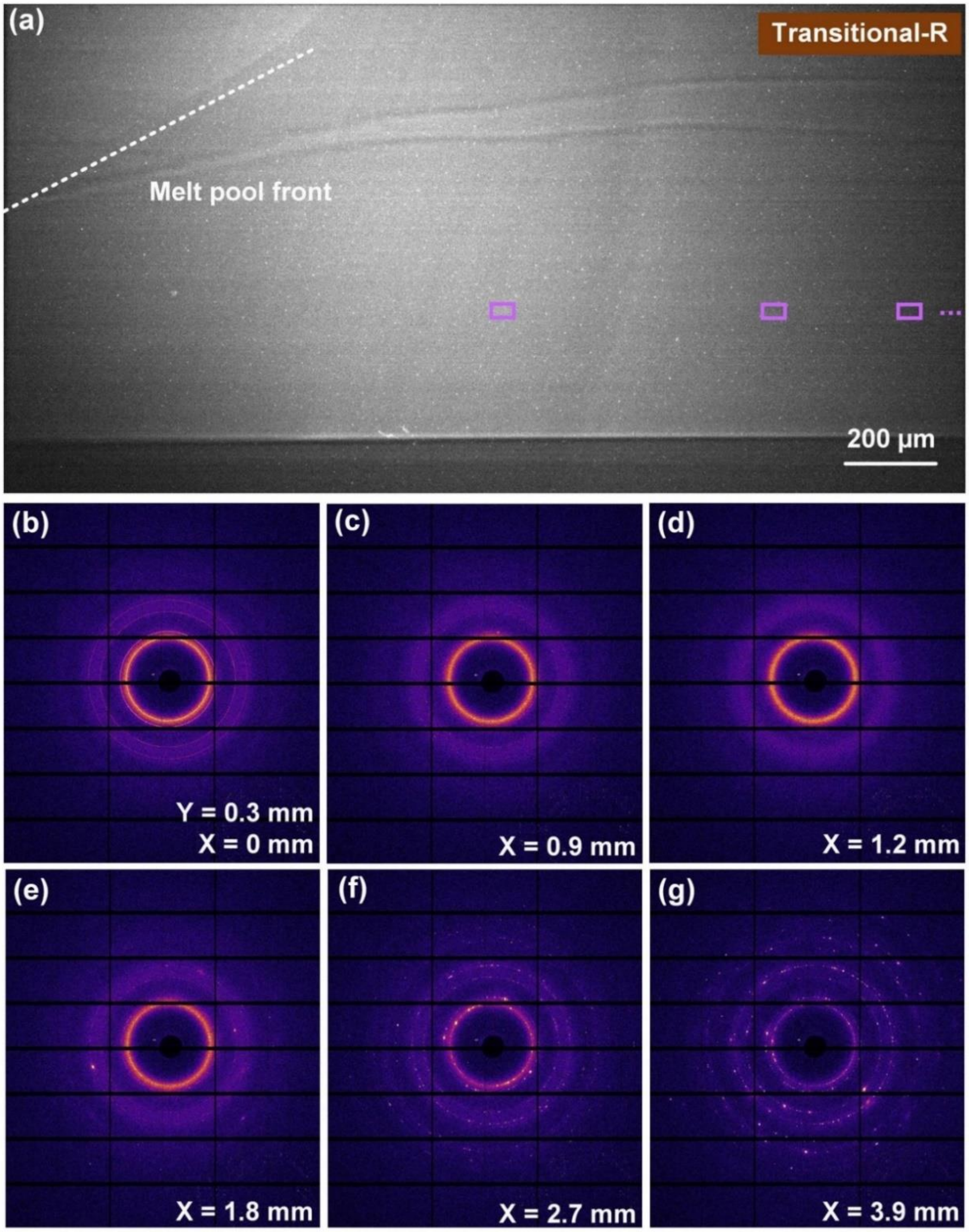

Figure 5.6*: The operando synchrotron x-ray characterizations of the Transitional-R printing. (a) x-ray imaging of the stable printing process. Purple rectangles in figure (a) define the characterization regions in diffraction experiments.). (b-g) Representative diffraction patterns collected from different regions of the melt pool during the stable printing period. The coordinates*

of x-ray location are noted at the lower right corner of each diffraction pattern. The coordinate system adopted in Fig. 5.4 is applicable here.

5.3.4 Post-characterization of samples printed from *operando* experiments

To establish a correlation between *operando* characterization and solidification microstructure, the present study conducted post-characterization on samples printed from the *operando* experiments. Figure 5.7 displays the EBSD IPF maps pertinent to the cross-sections of three tracks printed using different printing conditions. The solidification microstructure of these three samples, i.e., Lack of Fusion, Normal, and Transitional-R, is consistent with that observed in preliminary experiments (Figs. 5.2 and 5.3). However, the CET regions in the Lack of Fusion and Transitional-R samples printed in the *operando* experiments (Figs. 5.7a and 5.7c) exhibit asymmetry along the centerlines of their cross-sections, concentrating on one side. This phenomenon may result from the imperfect calibration of the three lasers before the *operando* synchrotron experiments. Nevertheless, this issue does not affect the subsequent analysis of the CET mechanism.

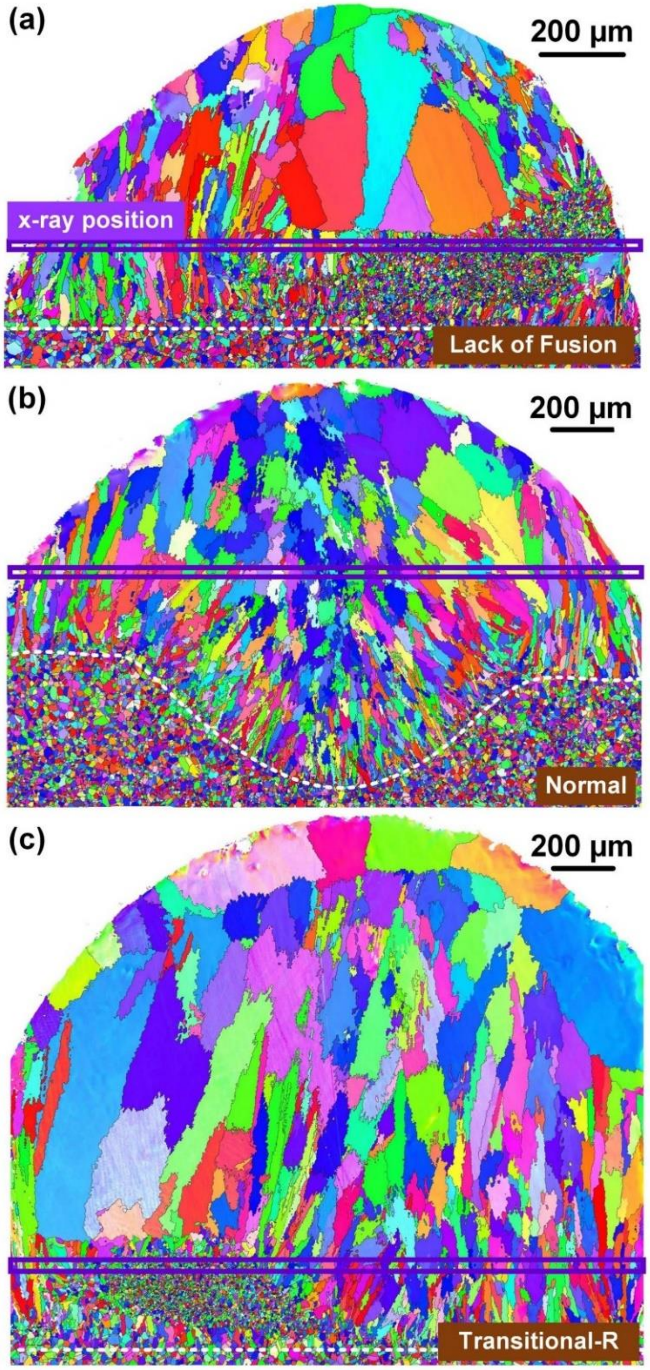

***Figure 5.7**: Post-characterization of Inconel 718 samples printed in the operando synchrotron x-ray diffraction experiments. The EBSD IPF maps displaying the cross-section of (a) Lack of Fusion, (b) Normal and (c) Transitional-R samples. The purple rectangular defines the characterization regions in operando x-ray diffraction experiments. Dashed lines/curves in white color mark the*

fusion boundaries between the printed tracks and Inconel 718 substrates.

The characterization regions of *operando* x-ray diffraction experiments are marked by purple rectangular on the EBSD maps. For the Lack of Fusion printing, the characterization region included both the unmelted wire and CET regions, as well as the coarse columnar grains on the other side. In terms of the Normal sample, only coarse columnar grains were involved. For the transitional-R printing, the formation of coarse columnar grains and the “abnormal” CET were characterized by the *operando* diffraction experiments. These microstructural features are consistent with the solidification processes observed through *operando* diffraction mapping (Figs. 5.4-5.6).

The grain refinement regions are compared in the Lack of Fusion (Fig. 5.7a) and Transitional-R (Fig. 5.7c) samples, as shown in Fig. 5.8. In the Lack of Fusion sample (Fig. 5.8a), two different equiaxed-grains regions, labeled as A-1 and A-2, can be readily identified. The grains in the A-1 region exhibited a more uniform size and regular shape. On the contrary, the grain shape and size in the A-2 region were more arbitrary. A microstructure similar to the A-2 region was observed in the Transitional-R sample, labeled as region B-1 in Fig. 5.8b. This equiaxed-grains region had a width of ~0.6 mm and was located near the deposit-substrate interface. The pole figures corresponding to the A-1, A-2, and B-1 regions were extracted from the EBSD maps, as displayed in Fig. 5.8c. In comparison, only grains in the A-1 region present a strong crystallographic texture, consistent with the previous characterization shown in Fig. 5.2c. The A-1 region with strong crystallographic texture is attributed to the unmelted wire. Nevertheless, the “abnormal” CET is responsible for the formation of both the A-2 region in the Lack of Fusion sample and the B-1 region in the Transitional-R sample.

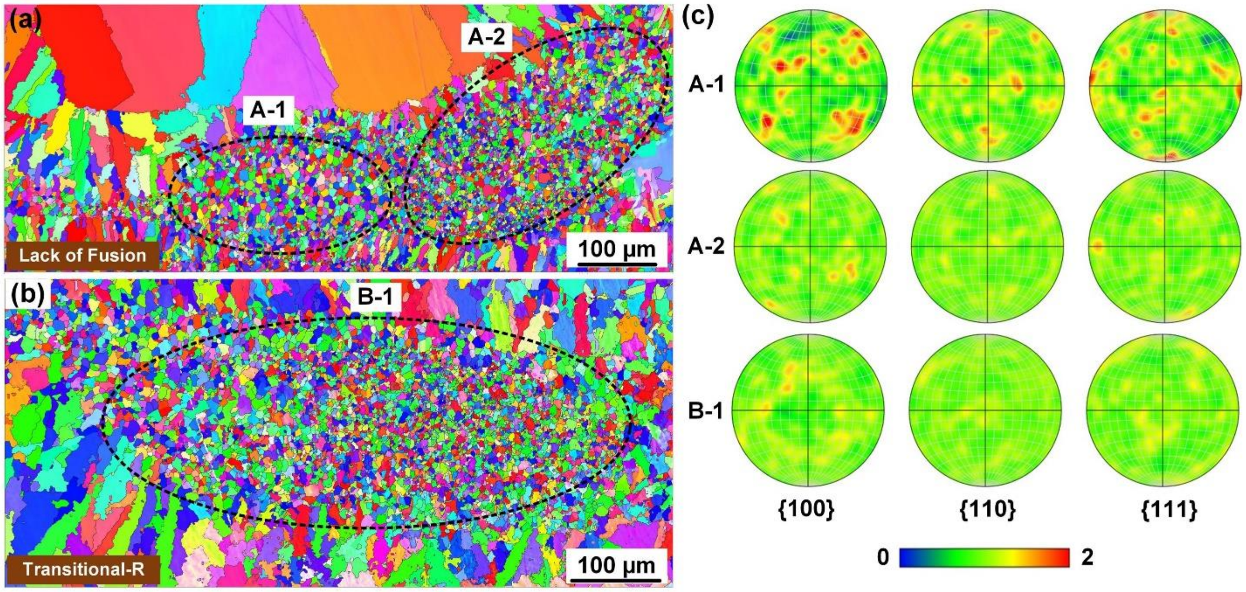

Figure 5.8: Post-characterization of the equiaxed-grains regions in the (a) Lack of Fusion and (b) Transitional-R samples. (c) The pole figures corresponding to the A-1, A-2, and B-1 regions marked in Figures (a) and (b).

5.3.5 Total-scattering analysis

Despite the *operando* characterization presented in Figs. 5.4-5.6, which confirms the occurrence of “abnormal” CET during solidification, the underlying mechanism associated with the “abnormal” CET remains unclear. The current hypothesis suggests that the preexisting icosahedral orders in the undercooled liquid are responsible for the “abnormal” CET in metal AM.

Total-scattering analysis of *operando* synchrotron diffraction offers a valid approach for investigating the atomic configuration of the melt pool. The narrow liquid region in the Transitional-R printing (Fig. 5.6d), located between the unmelted wire tip and the solidification front of the rear mushy zone, serves as a representative example for total scattering analysis. This is because, on one hand, this printing condition and detection region are directly correlated to the "abnormal" CET. On the other hand, the analysis of this fully liquid region offers a clearer presentation of the atomic orderings in the melt pool. In this data set, a batch of diffraction patterns collected during the stable printing period were summed to enhance the signal-to-noise ratio, as shown in Fig. 5.9a. This summed pattern only shows the diffusive scattering from the liquid phase, confirming the pure-liquid nature of this region. It should be noted that the bright dots concentrated at the lower right corner of the pattern are caused by the bad pixels on the detector. These artifacts had been appropriately removed prior to the analysis. The white arcs in Fig. 5.9a define the *Qmax* in the total scattering analysis. The total scattering data within *Qmax* was integrated over the azimuth angle. The total scattering intensity was converted to the total-scattering structure function *S(Q)* after background correction. As depicted in Fig. 5.9b, the *S(Q)* profile exhibits multiple oscillations at low *Q* values and gradually approaches one at high *Q* values. It is worth noting that a peak shoulder appears on the second oscillation of *S(Q),* as shown in the insert of Fig. 5.9b. This shoulder resulted from the overlap of two Gaussian peaks and was considered a feature associated with the presence of Icosahedral orderings in liquid metal [68,71]. The reduced PDF profile *Gr_Exp* was obtained by Fourier transforming *S(Q)* to gain a better understanding of the topological orderings in the liquid phase. This profile is represented by the black dots in Fig. 5.9c.

Each peak on *Gr_Exp* represents a specific atomic pair. The peak position refers to the distance between the two atoms in the pair. The peak broadening and limited number of peaks illustrate the amorphous nature of the liquid phase. Unlike the ordering in solid phases with a perfect crystal lattice, the atoms in the topological ordering clusters of liquid metal are more dynamic and can significantly deviate from their theoretical positions. In addition, the peak intensities of *Gr_Exp* decrease as r increases, and the oscillation ends at around r = 25 Å. This observation suggests that the size of certain atomic cluster(s) can reach 25 Å. It is worth noting that the *Gr_Exp* reflects the average information of a specific melt pool volume characterized by x-ray. Various topological orderings in the melt pool can contribute to this PDF profile. Furthermore, there are no apparent termination ripples at the high-r range, which illustrates the high quality of the *operando* data collection and the total scattering analysis.

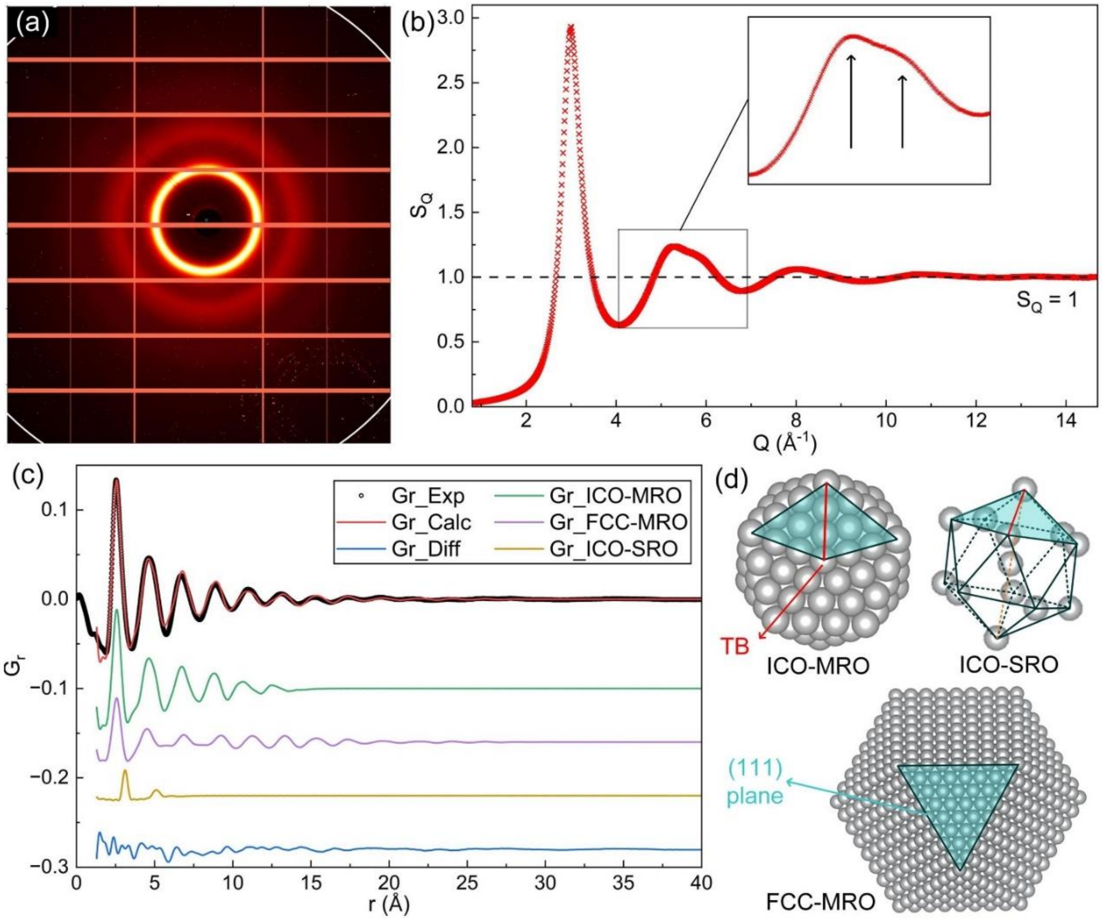

Figure 5.9: *Total scattering and PDF analysis of the operando diffraction experiments. (a) The summation of diffraction patterns corresponding to the stable printing period in the Transitional-R printing. The x-ray was probed in the narrow liquid region between the unmelted wire tip and the solidification front of the rear mushy zone, i.e., at X = 1.2 mm represented by Fig. 5.6d. (b) Total-scattering structure function S(Q) derived from Figure (a). (c) The PDF profiles converted from the S(Q) in Figure (b) and refined by small-box fitting. (d) The theoretical models of the atomic orderings in the melt pool.*

The peak shoulder on *S(Q)*, as highlighted in Fig 5.9b, indicates the presence of icosahedral orderings. In addition, the FCC-like cluster is one of the major ordering structures in FCC metals. Several characteristics of *S(Q)* also agree with the scattering of FCC-like orderings. Thus, the FCC-like and icosahedral topological ordering were identified as the two primary atomic clusters used as input for the small-box fitting of *Gr_Exp*. During the refinement process, icosahedral orderings with different sizes were tested. The size was adjusted by adding atomic shells to the unit icosahedron constructed by 13 atoms. The best fitting, namely *Gr_calc*, is presented by the red line overlaid on *Gr_Exp*. The blue profile, *Gr_diff*, represents the difference between *Gr_Exp* and *Gr_calc*. The good agreement between the *Gr_Exp* and *Gr_calc* illustrates adequate reliability of the refinement. The profiles *Gr_ICO-MRO* and *Gr_FCC-MRO* represent the partial PDF components contributed by the icosahedral and FCC-like medium-range orderings. Except for the first peak corresponding to the nearest atomic pair, the *Gr_ICO-MRO* and *Gr_FCC-MRO* profiles exhibit significant differences in peak positions and shapes. The size of the FCC-MRO was slightly larger than that of the ICO-MRO because the PDF profile at $r > 15$ Å was mainly attributed to the *Gr_FCC-MRO*. In addition, the unit icosahedron was applied to the refinement representing random atoms in the liquid phase, as displayed by the yellow profile in Fig. 5.9c. In the preliminary examination, the unit icosahedron resulted in a better fit than the unit FCC-like cluster. Compared to other medium-range orderings, the unit icosahedron offers a more significant atomic displacement for the random atoms and presents only a small portion of the liquid phase. The atomic models of the refined phases, namely, ICO-MRO, FCC-MRO, and ICO-SRO, are illustrated in Fig. 5.9d. Each type of cluster has a (111) plane or a distorted (111) plane on the free surface, depicted in blue. The five-fold axis of the ICO-MRO is normal to the page better to present the five-fold symmetry of this topological ordering. The adjacent (111) planes in both ICO-MRO and ICO-SRO exhibit a twinning relationship, and red lines on the atomic models mark the representative twinning boundaries (TBs).

PDF analysis was also applied to additional total-scattering data to gain a comprehensive understanding. The evolution of topological orderings during the AM processes is summarized in Fig. 5.10. The percentage bar charts in Figs. 5.10a, 5.10c, and 5.10e depict the volume fraction of each type of atomic cluster at various locations in the melt pool under the Lack of Fusion, Normal, and Transitional-R printing conditions, respectively. Error bars were determined based on the 10% deviation from the *Rw* value. The *Rw* value is a parameter used to evaluate the reliability of the refinement, referring to the standard deviation between the fitting and experimental profiles. In addition to the fraction of each atomic cluster, several refined parameters are shown in Figs. 5.10b, 5.10d and 5.10f. The atomic displacement of each topological ordering stands for the nearest distance between two neighbored atoms on the outer shell. Data points were not provided for the refined phases if they constituted only a negligible fraction. The x-axis of all subfigures in Fig. 5.10 indicates the distance from the characterization region to the wire feeding position, equivalent to the X coordinate shown in Fig. 5.4-5.6. In addition, “FCC-Crystal” refers to the FCC solid phase with a long-term periodicity resulting from either the unmelted wire or the solidified grains.

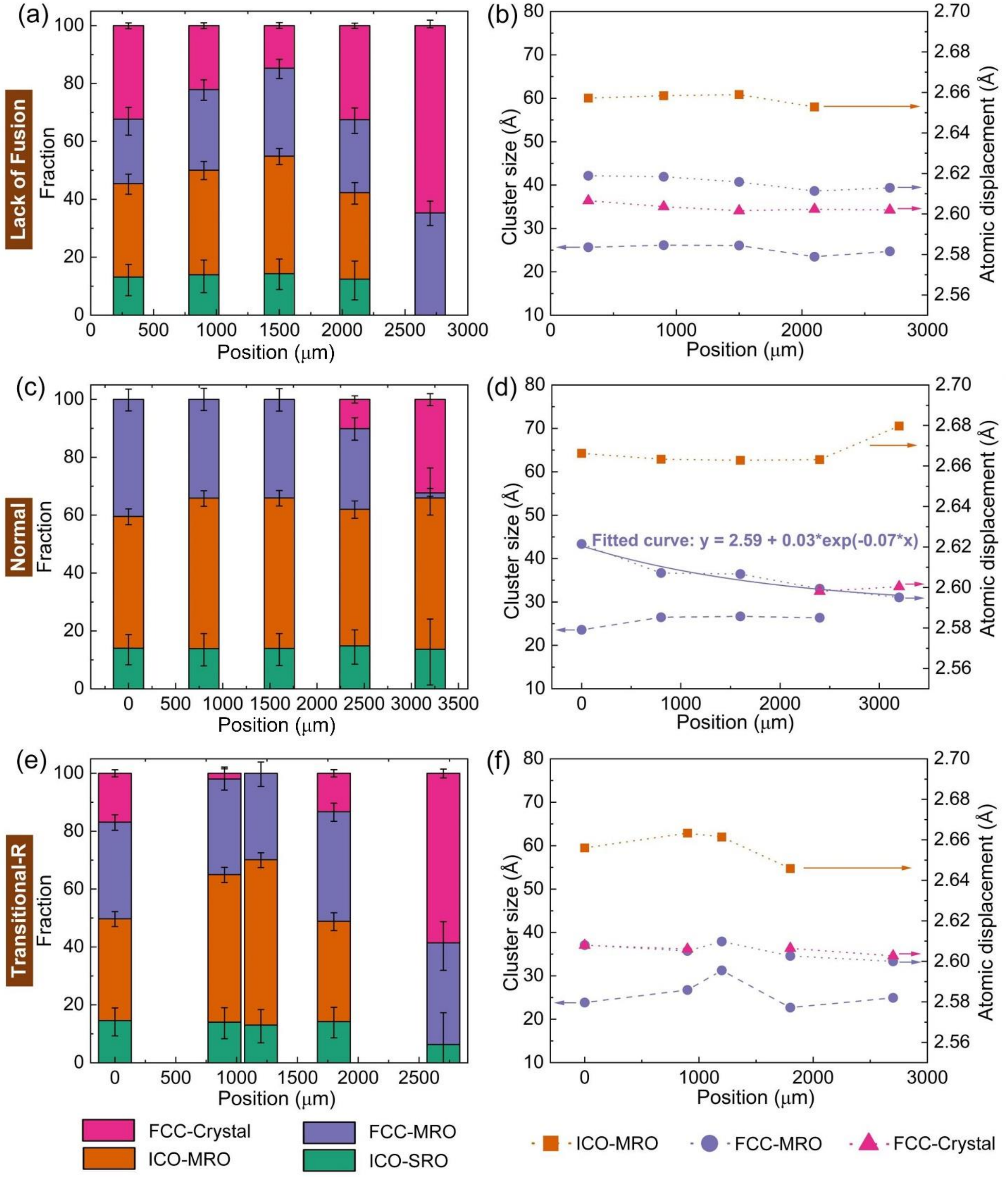

Figure 5.10: *The comprehensive analysis of operando total-scattering results reveals the evolution of topological orderings during the wire-laser DED processes. The percentage bar charts represent the volume fraction of each ordering structure corresponding to the (a) Lack of Fusion,*

(c) Normal, and (e) Transitional-R printing processes. Other refined parameters of each ordering structure corresponding to the (a) Lack of Fusion, (c) Normal, and (e) Transitional-R printing processes are shown in figures (b), (d), and (f), respectively.

Under the Lack of Fusion condition (Figs. 5.10a and 5.10b), the regions before the 1500 μm position correspond to further melting of the residual wire in the melt pool. During this process, the fraction of the solid phase decreased while more icosahedral and FCC-like medium-range orderings formed. The solidification process commenced at 1500 μm, accompanied by a continuous increase in the solid phase. In the early stage of solidification, the ICO-MRO was preferentially consumed. By the position of 2800 μm, only the FCC-MRO remained in the liquid phase. No significant variation in the refined parameters was observed during this printing process, as illustrated by Fig. 5.10b.

Figures 5.10c and 5.10d provide insights into the Normal printing process. Under this printing condition, no unmelted wire was present in the melt pool. These two subfigures thus indicate a typical rapid solidification process associated with generating coarse columnar grains. In the high-temperature region of the melt pool, i.e., at positions < 2500 μm, FCC-MRO and ICO-MRO were still the major topological orderings. The fraction of these two orderings varied slightly at different regions, possibly resulting from the temperature gradient within the melt pool. In this printing process, solidification started at the position of 2400 μm. In contrast to the lack of fusion process, the FCC-MRO was selectively consumed at the start of solidification, but the ICO-MRO remained in the liquid. The variation in refined parameters is shown in Fig. 5.10d. Because of the temperature gradient, there is a significant decrease in the atomic displacement of the FCC-MRO from the melt pool front to the rear melt pool. As shown in the figure, this temperature-dependent effect was fitted by an exponential function. The size of FCC-MRO nearly remained constant during this period. The atomic displacement of ICO-MRO was stable, except during the later stage of solidification.

The investigation of the Transitional-R printing process is presented in Figs. 5.10e and 5.10f. Overall, this process was very similar to the Lack of Fusion printing (Figs. 5.10a and 5.10b). The solid wire existed and continuously melted inside the melt pool. Medium-range orderings, especially the ICO-MRO, accumulated further during this period. In the rear melt pool, the ICO-MRO quickly depleted with the onset of solidification. The evolution of the refined parameters also exhibited a stable trend. However, the key difference between the Transitional-R and the Lack of Fusion processes was whether the solid wire was fully melted inside the melt pool. In the Transitional-R condition, a narrow region of less than 900 μm in the length of the melt pool, consisting solely of liquid, formed between the unmelted wire tip and solidification front.

5.4 Discussion

5.4.1 Atomic orderings in the liquid Inconel 718 alloy under the AM condition

The icosahedral ordering in liquid metals has been investigated for decades since it was first proposed by Frank [70]. Compared to stable liquid metal at a temperature significantly higher than the melting point, more attention has been directed towards undercooled metallic melts. This is because the icosahedral ordering is more prominent in undercooled liquid metal [69], and the presence of icosahedral plays a critical role in the solidification and glass formation of liquid metals [142]. As reported by previous studies [69,143], near the melting temperature, the fraction of the icosahedral clusters in the liquid Ni is greater than 50%, with this cluster typically consisting of only 33 atoms. Generally, the fraction and size of icosahedral clusters increase as the temperature decreases. According to the measurement in this work, the major clusters observed in the melt pool of Inconel 718 alloy included both icosahedral and FCC-like orderings. Their fractions only slightly varied with temperature, as shown in Fig. 5.10c. This observation agrees with the result reported in the previous investigation. Wang *et al.* [144] conducted Molecular dynamics simulation for a $Ni_{60}Cr_{21}Fe_{19}$ alloy, which has a similar ratio of the principal elements in the Inconel 718 alloy. The oscillation of the calculated PDF profile extended to ~12Å at a significant undercooling, when T/T_L = 1100K/1685K. However, the sizes of the icosahedral and FCC-like clusters measured here under AM conditions were ~15 and 25 Å, respectively. Therefore, these clusters were considered as medium-range rather than short-range orderings. The variation of temperature inside the melt pool had less effect on the cluster size, and this was also applicable to the Normal printing condition which formed a melt pool with higher temperatures.

The medium-range size of the topological orderings in the melt pool can be explained and discussed from two aspects. First, the wire feedstock underwent rapid melting in the wire-laser DED process. As discussed in Chapter 3, the laser energy was only absorbed by the free surfaces of the melt pool and of the wire. The melt-pool interior was only heated by thermal conduction and heat convection. Materials such as Inconel 718 alloy, which have an elevated melting temperature but low thermal conductivity, are challenging to fully melt or decompose to a more amorphous state within a short timeframe. Compared to powder feedstocks, the adequate melting of wire feedstocks is even more challenging due to the low surface-to-volume ratio. Cleveland *et al*. investigated the rapid melting process of FCC Au nanocrystalline clusters using molecular dynamics simulation. Their study revealed that the icosahedral precursors can form during the rapid melting process. Therefore, the Inconel 718 wire may tend to generate icosahedral medium-range orders in the wire-laser DED process owing to inadequate superheating.

Another potential reason for the extended sizes of topological orderings is related to the complex composition of the material system. As a commercial alloy, Inconel 718 contains three principal elements (Ni, Cr, and Fe), along with several minor elements, including Nb, Mo, and Co. Ronchetti and Cozzini [145] reported that the icosahedral clusters are favorable when $r_A/r_B \leq 1.25$, where r_A and r_B represent the larger and smaller atoms in the alloy. The principal elements, Ni, Cr, and Fe, have similar atomic radii ranging from 1.35 to 1.4 Å, which is beneficial in forming icosahedral clusters. Certain minor elements also contribute to the stabilization of the atomic clusters. For instance, Nb is believed to stabilize icosahedral orderings by forming directional chemical bonding between Ni and Nb atoms [145,146]. Hence, the complex composition of the Inconel 718 alloy could be responsible for the extended atomic clusters.

To better understand the atomic ordering in the high-temperature melt pool, the *operando* synchrotron scattering was conducted for the Transitional-R printing, with the x-ray probing at a region near the upper surface of the melt pool. The coordinates of this region were X = 1200 μm and Y = 800 μm. The resulting PDF profile was compared with that from a lower region, X = 1200 μm and Y = 300 μm, i.e., *Gr_Exp* shown in Fig. 5.9c. Since the laser was directly applied to the upper surface, the temperature at the upper region could be ~200K higher than at the lower region, which was roughly evaluated through the multi-physics simulation. As shown in Fig. 5.11, the red profile corresponding to the upper melt pool exhibits a slight shift towards the high-*r* range compared to the lower region represented by the black curve. This shift indicates the thermal expansion in the upper region. However, these two PDF profiles still exhibit a strong agreement in peak shape and intensity, which suggests a near-identical configuration of atomic clusters in these two regions. This result suggests that the complex composition, rather than the insufficient melting, was the dominant factor leading to the medium-range ordering. It should be noted that the current experiment and analysis only considered the topological ordering in the liquid alloy. This consideration was valid for the PDF fitting in such a scenario where the principal elements of Inconel 718 exhibited similar scattering amplitudes at high x-ray energy. However, the current efforts are insufficient to provide more direct and robust evidence beyond the comparison above and to explain the role of minor elements. Differential PDF is an alternative measurement capable of providing both topological and chemical information about atomic clusters. In this method, the energy of incident x-rays is required to adjust according to the absorption edge of each species. However, applying this method in such *operando* experiments is still challenging. For instance, lower x-ray energy can result in significant x-ray attenuation for measuring thick metal samples. Thus, this chapter only focuses on the topological structures of the atomic orderings.

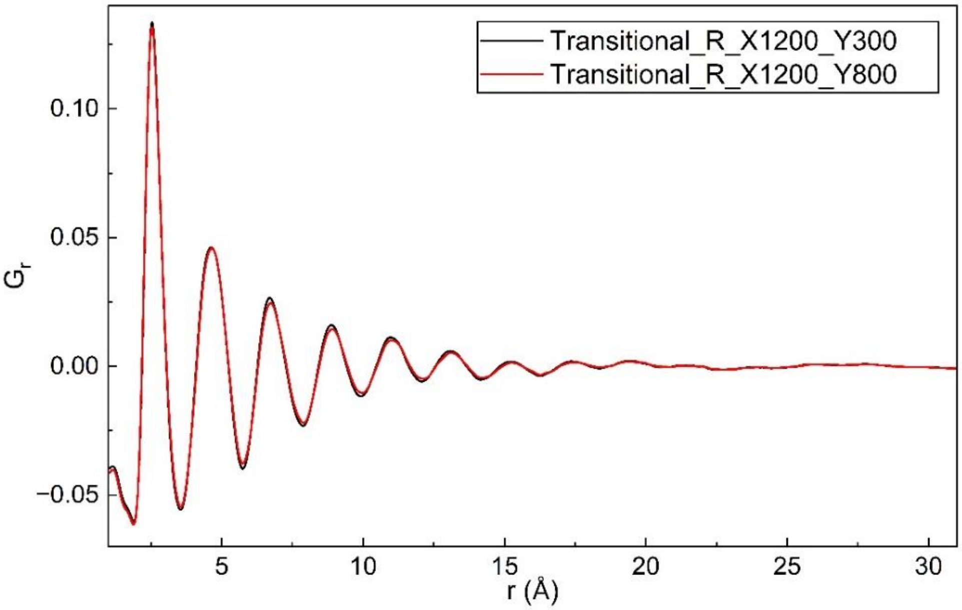

Figure 5.11: *PDF profiles extracted from an upper region (X = 1200 µm, Y = 500 µm) and a lower region (X = 1200 µm, Y = 300 µm) of the melt pool in the Transitional-R printing.*

5.4.2 Roles of atomic orderings in the solidification process of wire-laser DED

The solidification process in the wire-laser DED process of Inconel 718 is accompanied by the variation of atomic orderings. Atomic clusters can affect solidification in various aspects, including influencing atomic mobility and melt pool viscosity. The evolution of atomic orderings also provides insight into the solidification mechanism. In the case of Normal printing (Fig. 5.7b), where the columnar grains were included in the x-ray characterization volume, the solidification process was primarily governed by directional grain growth. For the Lack of Fusion and Transitional-R printing processes (Figs. 5.7a and 5.7c), both columnar grains and the “abnormal” CET were covered in the x-ray characterization volume. The CET formed at the center of the melt pool, close to the unmelted wire under the Lack of Fusion condition. In the entire x-ray characterization volume, solidification took place first at the center bottom region with lower temperatures, i.e., the "abnormal" CET region. In addition, more diffraction spots, indicating coarse grains, formed at positions farther from the laser, e.g., at X = 4.0 mm. Thus, the earlier stage of solidification in both the Lack of Fusion and Transitional-R processes was associated with the occurrence of the "abnormal" CET. The comprehensive analysis of *operando* total-scattering results shown in Fig. 5.10 provided valuable insight into the underlying mechanism of the "abnormal" CET process. As illustrated in Fig. 5.10b, solidification in Normal printing began with the consumption of FCC-MRO in the melt pool. In contrast, the ICO-MRO participated in solidification first for Lack of fusion and Transitional-R processes, corresponding to the occurrence of "abnormal" CET.

Liquid metal is a mixture of various atomic clusters, and the structures of these atomic clusters are dynamic. Similarly, the atomic structure of the melt pool here can be described as constructed by numerous atomic polyhedrons, i.e., atomic orderings. These polyhedrons exist in a dynamic structure. Atomic diffusion takes place inside or between the polyhedrons. In addition, there is a certain rotation degree for these polyhedrons [147]. Neighboring polyhedrons can be assembled and aggregated. For example, the ICO-MRO can be obtained by assembling a unit icosahedral short-range ordering with several FCC-like clusters. It was reported that icosahedral clusters exhibit a strong aggregation tendency [148]. The medium-range ordering plays a more critical role in solidification than the short-range ordering, because the former has better stability in the undercooled liquid and imposes a more significant impact on the properties of metallic liquid, like viscosity, [142]. The icosahedral orders are considered slow dynamic regions in which the surrounding diffusive motion of atoms is restrained. Therefore, crystal nucleation tends to occur in such a region through an ICO-MRO template. However, there is typically a significant mismatch of the atomic displacement between ICO-MRO and other structures, including FCC-like MRO and FCC crystal [149], which is also reflected by the atomic displacement measured in Fig. 5.10. The directional attachment between ICO-MRO and other structures is less likely, thereby slowing down or suppressing crystal growth. In contrast, the good structural coherence between the FCC-like and FCC crystals is favored for directional attachment, tending to induce a domino-like growth mode and accelerate grain growth.

The evolution of the atomic structure of the melt pool characterized in this study (Fig. 5.10) unveiled two different solidification mechanisms at the atomic level. At the early stage of solidification in the Normal printing, columnar grain growth was dominated and assisted by the directional attachment of FCC-like MRO. Therefore, the FCC-like MRO was preferably consumed during the initial solidification. In this printing condition, the remaining SRO-MRO had less effect on the solidification process and would then decompose to random atoms or smaller FCC-like SRO, contributing to the columnar growth of grains in the later solidification region. The abnormal lattice expansion of the ICO-SRO observed in Fig. 5.10d implied the subsequent decomposition process.

Except for the columnar grain growth explained above, the “abnormal” CET is another important solidification mechanism pertinent to atomic orderings. Although the “abnormal” CET in AM and ISRO-mediated solidification have already been hypothesized and widely propagated

[55,57–59,61], this work presented a direct and experimental insight into the atomic structure of the melt pool. One important difference is the size of the atomic clusters. The mainstream perspective from previous works is still based on the classic nucleation theory (CNT), in which the nucleation starts on a unit icosahedral SRO with only 13 atoms. Epitaxial growth takes place on the faces of SRO through the close packing of free atoms, leading to twinning boundaries and refined grains. However, it is suspected because the SRO is much smaller than the critical nuclei. For liquid Ni, the critical nuclei typically consist of ~55 atoms [150]. Thus, the direct diffusive motion of atoms to expand the SRO is not thermodynamically favored during solidification. Indeed, the icosahedral SRO may possess stronger and directional bonds, making it more specific to the chemical ordering [142]. With the observation of the medium-range orderings in this work, the concern about the critical nucleation size can now be addressed. Epitaxial growth can then take place via the diffusive motion of random atoms and lead to the "abnormal" CET. The icosahedral MRO can be described as the directional attachment between a unit ICO-SRO core and a shell consisting of FCC-like orderings. The wide distribution of ICO-MRO observed in the present *operando* experiments confirmed the moderate connection between ICO-SRO and FCC-like orderings. Similarly, the directional attachment between ICO-MRO and FCC-MRO could take place to facilitate the "abnormal" CET despite the lattice misfit. Except for the epitaxial growth and directional attachment, another potential mechanism of the "abnormal" CET is the decomposition of ICO-MRO. The metastable ICO-MRO is expected to decompose into several segregated FCC nuclei, thereby contributing to the "abnormal" CET. This mechanism is more consistent with the present PDF analysis that suggested the preferable consumption of ICO-MRO in the “abnormal” CET (Fig. 5.10). The epitaxial growth and directional attachment are less likely because, on one hand, both of them further increase the elastic strain energy of the cluster. On the other hand, as suggested by the *operando* measurements, the size of these clusters was very stable either with temperatures increasing or during solidification. Additionally, the fraction of FCC-MRO was not reduced during the “abnormal” CET. Given the considerable size of both ICO-MRO and FCC-MRO, the directional attachment was less efficient and less likely to generate several segregated grains with five-fold symmetry. In conclusion, the decomposition mechanism of the FCC-MRO is more reasonable for initiating the “abnormal” CET. It should be noted that this process is different from the later solidification stage of the Normal printing that decomposes FCC-MRO into random atoms.

Previous studies also suggested that the presence of the metastable icosahedral quasicrystals or icosahedral orderings is the primary reason triggering the “abnormal” CET in metal AM. It also should be noted that the medium-range orderings observed here are fundamentally distinct from the metastable icosahedral quasicrystals proposed in previous works [56–58,60]. They may have similar sizes, while the atoms in the medium-range orderings herein are more dynamic and disordered. Cazic et al. speculated that undissolved TiC particles could exist in the melt pool during the wire-laser DED of Inconel 718, which could result in local element segregation around the TiC particles and promote the formation of ISRO in the surrounding liquid [61]. Similar to their previous statement [55], the local grain refinement was attributed to the heterogeneous distribution of carbides and icosahedral orderings in the melt pool. Indeed, Chapter 3 of this dissertation demonstrated the possibility of unmelted carbides and other solid particles in the melt pool during the wire-laser DED of Inconel 718 with a restrained energy input. However, the “abnormal” CET did not occur under that printing condition. In the case of Transitional-R printing introduced in this chapter, almost no unmelted particles were observed in the narrow liquid region between the unmelted wire tip and the solidification front, but the “abnormal” CET occurred. Furthermore, the current *operando* experiments indicated a wide distribution of icosahedral orderings in the melt pool, even in the Normal printing and the upper melt pool of the Transition-R printing that only formed columnar grains. This discrepancy suggests that the presence of icosahedral orderings is neither the sole nor the most critical reason for triggering the “abnormal” CET in the wire-laser DED of Inconel 718. A more comprehensive understanding of the thermal conditions inside the melt pool, especially in the case of Transitional-R printing, is needed to explain the detailed mechanism of the “abnormal” CET.

5.4.3 Critical conditions for triggering the “abnormal” CET

The multi-physics simulation was performed to explore other factors that may be involved in the “abnormal” CET. Figure 5.12 displays the simulated wire-laser DED process of Inconel 718 under the Transitional-R condition. The color map and black arrows represent the temperature distribution and the plane vector of melt flow, respectively. Unlike the simulation in the previous chapters, the simulation performed here added a phantom region in a certain region of the melt pool, as marked by a white rectangular in Fig. 5.12a. This configuration aims to replicate the movement of unmelted wire inside the melt pool, as observed in the *operando* experiment (Fig. 5.6). Under this printing condition, the solid wire did not fully melt as it inserted into the melt pool.

After moving a short distance horizontally in the melt pool, the wire tip melted, and a narrow, fully melted region was generated between the wire tip and the rear melt pool, as marked by a purple circle in Fig. 5.12a. The relatively higher temperature of this narrow region results in a concave isothermal surface in the melt pool. While this phenomenon agrees with the experimental observations, it should be noted that this simulation might not perfectly replicate the real experiments in some aspects. For example, the interested region (as marked by the purple circle) in the simulation was slightly higher than the location of the "abnormal" CET region in the as-printed Transitional-R sample (Fig. 5.7c). This was because the simulation software lacked a more reliable function to accurately describe the actual motion of unmelted wire inside the melt pool. The phantom function of the simulation arbitrarily imposed a constant velocity for the solid phase within the target region. Despite this compromise, the current simulation is still valid for qualitatively analyzing the printing process. The present investigation focuses on the response of thermal conditions and melt pool dynamics in the narrow region between the wire tip and the solidification front. As revealed in Fig. 5.12a, that narrow (or concave) region is affected by two major streams of melt flow. The melt flow from the upper and rear melt pool regions gathered at the narrow region, thereby leading to a vortex in the concaved region, as displayed in the center plane of the melt pool. Figure 5.12b presents the front view of the cross-section relevant to the concave region, with the relative position of this visualization plane indicated in Fig. 5.12a. In this view, the concave region was also identified at the bottom of the melt pool, as suggested by the curved liquidus and solidus lines. As marked by the purple circle in Fig. 5.12b, this region experienced a melt flow from the upper melt pool. Two vortices in opposite directions were distributed on both sides of this region.

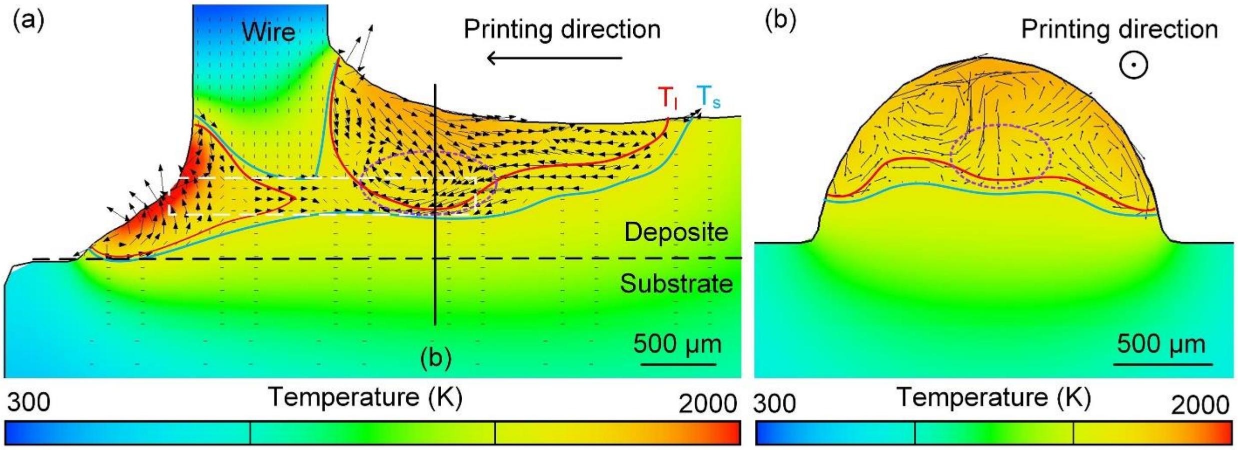

***Figure 5.12**: Multi-physics simulation of the wire DED process of Inconel 718 under the Transitional-R condition. The 2D slices of (a) the center plane on the lateral view and (c) the cross-section on the front view. The position of figure (b) relative to figure (a) is marked by a black line in (a). In both figures (a) and (b), the color map and black arrows within the melt pool display the temperature distribution and flow dynamics, respectively.*

To better understand the thermal conditions in the concave region, 3D contour maps of the solidification front were extracted from the multi-physics simulation, as shown in Fig. 5.13. The isosurface of the 3D contour maps was defined by the solidification fraction of 0.1, which corresponds to the solidification front. Similar to the 2D view of Fig. 5.12, a concave region between the wire tip and the rear mushy zone was also observed in the 3D view, as indicated by a purple circle in Fig. 5.13a. Three red arrows mark the approximate positions of laser beams. As indicated in Fig. 5.13a, the Z direction is parallel to the building direction that is normal to the substrate surface, while the Y direction is opposite to the printing direction. In the Transitional-R process, the melt pool absorbed energy from a front laser and two rear lasers. The two rear lasers were distributed on both sides of the melt pool, imposing intense heating symmetrically on the upper melt pool. Consequently, two vortices formed in the lateral melt pool, as shown in Fig. 5.12b, are formed. However, the heat convection from the upper melt pool was responsible for the formation of the concave region. The 3D contour maps were colored according to the distribution of temperature gradient (G), as shown in Figs. 5.13b-5.13d. The G component in the transverse direction (X direction) is displayed in Fig. 5.13b. As revealed by the color change, the direction of G_X reversed at the center of the concave region along the X direction. Additionally, the direction of G_X reversed again at the boundaries of the concave region. The G_X at the lateral melt pool (outside the concave region) was dominated by the thermal conduction from the upper lateral melt pool, which was directly heated by the rear lasers, to the melt pool interior. The special G_X distribution inside the concave region further demonstrated that the concave was generated due to the strong heat convection from the upper melt pool rather than directional heat conduction. Figure 5.13c displays the distribution of G_Y on the 3D counter. The concave region also experienced a complex G_Y along the printing direction. The colder wire tip and rear melt pool resulted in the opposite G_Y at the front and rear parts of the concave region. Compared to the components in other directions, the temperature gradient in the Z direction, i.e., G_Z, remained the dominant component in the concave region, as shown in Fig. 5.13d. However, a banded region corresponding to lower G_Z is displayed across the entire concave in the printing direction (-Y direction). Such complex thermal conditions in the concave region are rarely observed in common printing processes, for example, the similar analysis shown in Fig. 3.12.

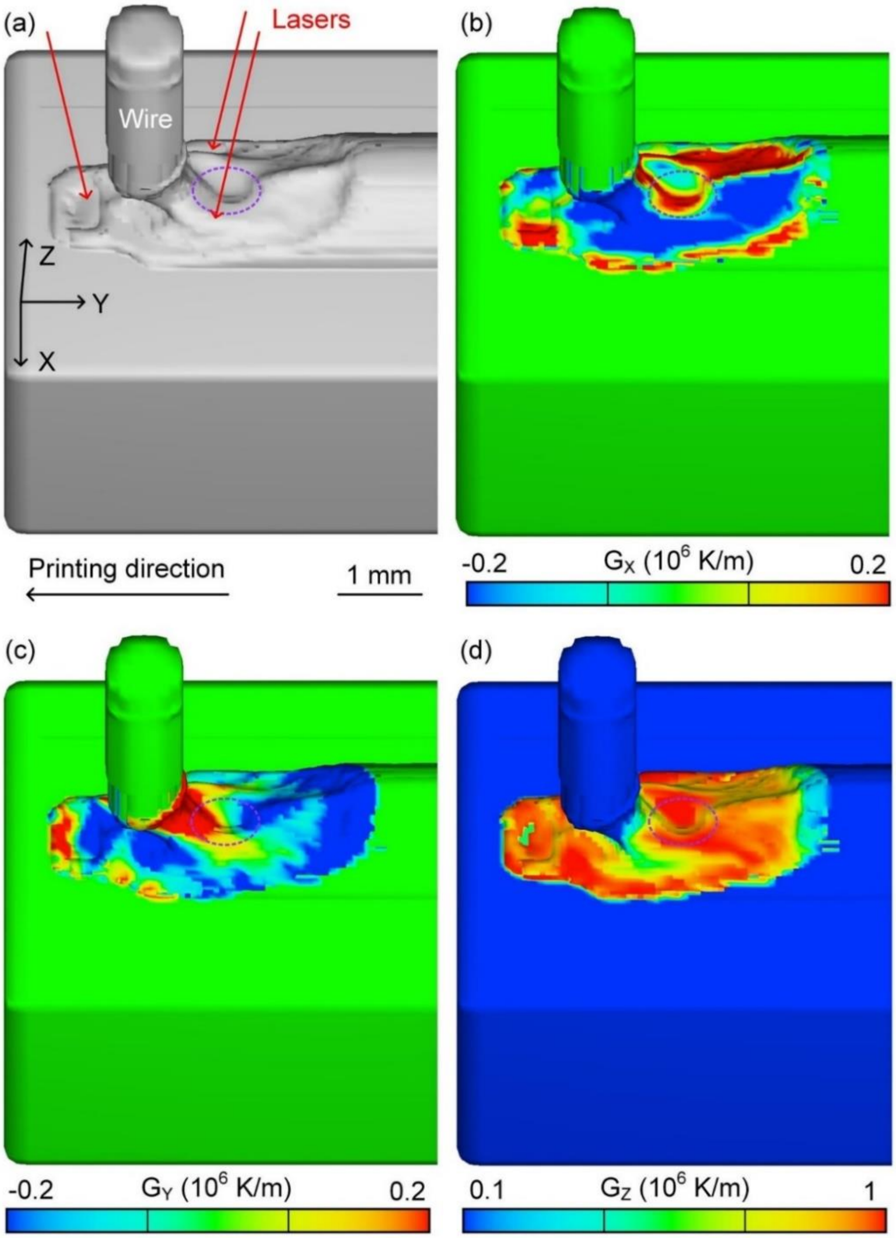

Figure 5.13*: Multi-physics simulation showing the 3D counter of solidification front and the distribution of temperature distribution. The iso-surface of the solidification front was determined by the solidification fraction of 0.1. (a) The 3D contour of the solidification front, and the counterparts colored by G_X, G_Y, and G_Z. A purple circle marks the concave region in each subfigure.*

Besides the preexisting atomic orderings in the melt pool, the thermal conditions and melt pool dynamics were considered critical factors that induced the “abnormal” CET. The multi-physics simulation reveals that the unique thermal conditions and melt pool dynamics in the concave region can contribute to the “abnormal” CET in the following ways. Like the common CET based on classic nucleation theory, the “abnormal” CET associated with atomic orderings also prefers a larger undercooling [142,151]. Although the current solidification model cannot precisely predict the undercooling at the concave region, the lower temperature gradient and faster solidification imply a higher undercooling [50]. The faster solidification rate is indicated by the steep solidification front shown in Fig. 5.12a. Therefore, the “abnormal” CET was promoted in the concave region, but quantifying this effect is challenging due to the limited knowledge of the “abnormal” CET. Nevertheless, it can be estimated that this contribution to normal CET was negligible because the temperature gradient, especially G_Z, did not reduce more than one order of magnitude. Another important factor is the directional thermal gradient in the concave region. As revealed by Fig. 5.13, the concave region experienced significant variations in G, especially in the X and Y directions. The spatial distribution of the maximum temperature gradient varied significantly in this region, which was not conducive to the growth of columnar grains. As a result, the “abnormal” CET was promoted owing to its competition with the growth of columnar grains [152]. The unique melt pool dynamics are also worth noting. On the one hand, the concave region was subjected to melt flow from both the upper and rear regions of the melt pool, resulting in a significant fluctuation of microstructures in this area. Structural fluctuation of MRO was required to accommodate crystal nuclei [54]. On the other hand, a melt flow vortex was generated in the concave region, as shown in Fig. 5.12a. Icosahedral orderings, especially the ICO-MRO, restrict atomic mobility and affect melt pool dynamics in the local region [142,148]. Consequently, more icosahedral orders tend to accumulate or become trapped in the concave region, leading to localized CET. As supported by the total-scattering analysis in Fig. 5.10, the fraction of ICO-MRO slightly increases in the concaved region. Henry et al. [153] studied the influence of convection on the solidification behavior of Al alloys. It was found that the fluid flow can promote twin dendritic growth. Twin dendritic growth recently was also believed to be a consequence of ISRO-mediated nucleation [154]. From this aspect, the additional flow vortex in the concave region was also beneficial in occurring the "abnormal" CET.

5.4.4 Insights into other material systems and the printing of bulk samples

Different material systems exhibit distinct atomic orderings in the liquid phase, influenced by interparticle interaction and entropy [54]. Atomic orderings formed in the liquid phase tend to follow the symmetry of their corresponding equilibrium crystals. For this consideration, *operando* synchrotron x-ray diffraction was also employed on 316L stainless steel (SS) to investigate the potential of this "abnormal" CET in the wire-laser DED of other materials systems. The 316L SS is a good example because its solid phase presents an allotropic transformation from the Austenite (FCC structure) to the Ferrite (BCC structure) phases as temperature increases. Typically, Ferrite is the primary phase during the solidification of 316L SS. Moreover, studying this commercially available feedstock is of practical significance for the metal AM community. Following the same procedure, the total-scattering analysis was also performed for the wire-laser DED printing of

316L. The *S(Q)* and *G(r)* profiles corresponding to the liquid phase from the rear melt pool were extracted, as shown in Fig. 5.14. The characteristics of *S(Q)*, particularly the shape of the second peak, agree with those observed in previous studies regarding liquid iron with BCC-like orderings [155,156]. The PDF profile, represented by black dots in Fig. 5.14b, was refined using the BCC phase with consideration of the effect of ordering size. The calculated *G(r)* of BCC-MRO and the difference profile are represented by a red and blue curve, respectively. The excellent refinement demonstrated that BCC-like ordering was dominant in the melt pool of 316L SS. While the ordering size, indicated by the final oscillation of *G(r)*, was similar to that of Inconel 718, the prevalence of BCC-like ordering in the melt pool made the occurrence of the "abnormal" CET less likely in printing 316L SS. This observation can explain the coincidence that the "abnormal" CET is mainly observed in the AM of FCC metals, like Ni and Al alloys. In contrast to the single type of atomic clusters in BCC alloys, the combination of FCC-like MRO and ICO MRO with comparable fractions could also benefit the "abnormal" CET of FCC alloys. However, König *et al.* recently conducted *operando* x-ray diffraction experiments for the laser powder bed fusion (LPBF) of steel, and they found that the high cooling rate can inhibit the formation of primary Ferrite during solidification [157]. Furthermore, Monier *et al.* reported that ISRO-mediated solidification can also occur in the LPBF of 316L SS, slightly refining the columnar grains and forming more twinning boundaries [59]. The adopted scanning speed was higher than that used in König's work. The above investigations suggest the potential of this "abnormal" CET in the AM of BCC materials. The rapid cooling rate in metal AM can result in a large undercooling, consequently affecting the atomic structure and the evolution of the undercooled liquid during rapid solidification.

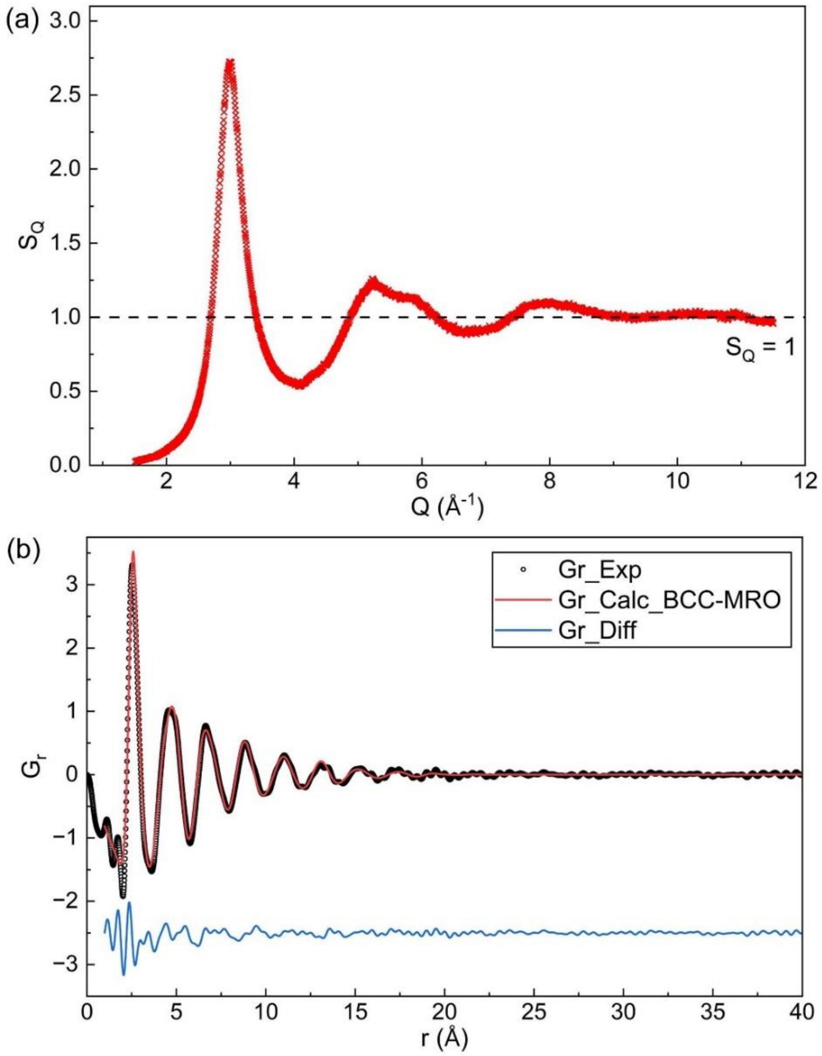

Figure 5.14: *(a) Total-scattering structure function S(Q) corresponding to the rear melt pool during the wire-laser DED of 316L SS. (b) The PDF profiles converted from the S(Q) in figure (a) and refined by small-box fitting. The experimental, as-refined, and differential G(r) profiles are represented by black circles, red, and blue lines, respectively. The high-frequency termination ripples on this PDF profile are artifacts due to insufficient background correction and a lower signal-to-noise ratio of the raw data. The parameters of the synchrotron experiments are similar to those applied for the Inconel 718, while the size of x-ray is 100 (Horizontal) × 30 (Vertical) μm^2. The printing conditions P = 360 W, S = 7 mm/s, and F = 7.35 mm/s were adopted for the wire-*

laser DED of 316L SS.

To ensure measurement consistency and simplify the analysis, *operando* synchrotron experiments were exclusively conducted for printing a single track on the substrate. As inferred from the processing window shown in Fig. 5.1, higher laser power is associated with a broader processing range for the “abnormal” CET. Typically, moderately high scanning speed *S* and feeding rate *F* are favored for triggering the “abnormal” CET in wire-laser DED. This statement is supported by the unmelted wire inside the melt pool and the appearance of the concave region between the wire tip and the rear melt pool. To further enhance the impact of these new insights, wire-laser DED of Inconel 718 was carried out to print a bulk sample using the M450 DED printer equipped with six laser beams. The laser power, scanning rate, and feeding rate were intentionally increased to 1000 W, 16.7 mm/s, and 83.3 mm/s, respectively. Figures 5.15a and 5.15b are optical images showing the magnified regions in the as-printed bulk sample. The printing (scanning) direction is normal to the plane of these two images, and white dashed curves mark the fusion boundaries. The “abnormal” CET is also observed in this bulk sample, as indicated by the red rectangle. Similar to single-track printing, the “abnormal” CET in the bulk sample tends to form at the lower region of each melting track.

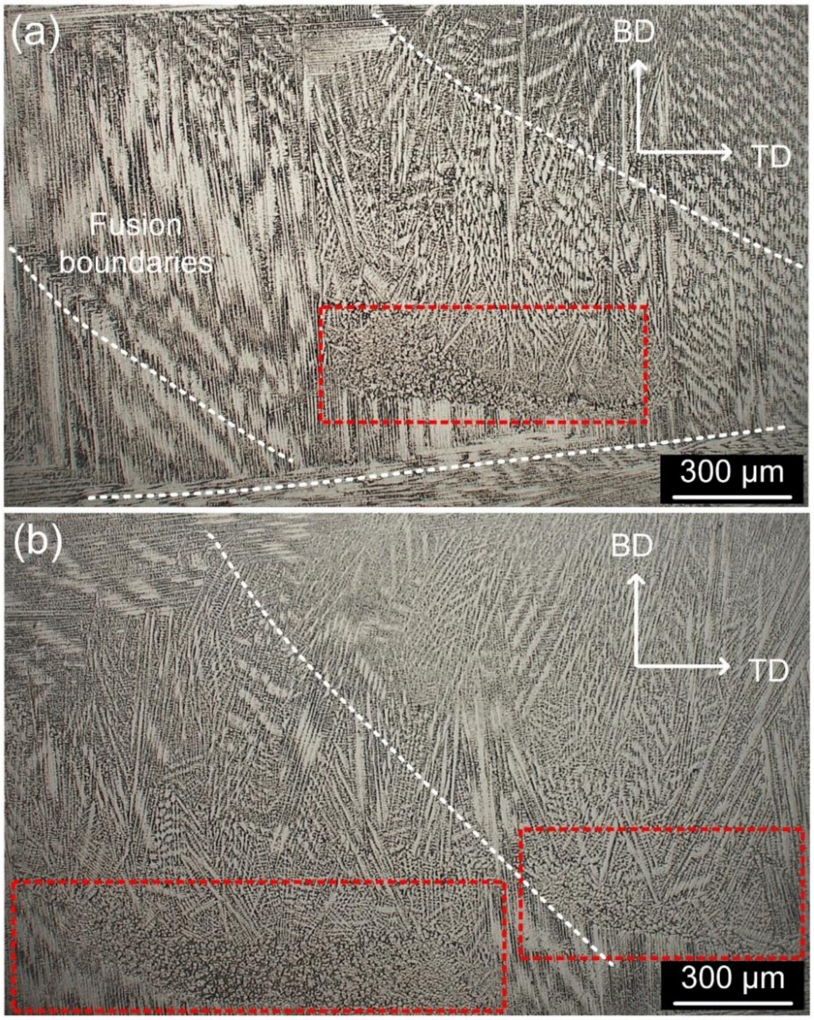

Figure 5. 15: Optical images showing magnified regions of the bulk Inconel 718 sample fabricated by wire-laser DED. The printing (scanning) direction is normal to the plane of these two figures. The fusion boundaries are marked by white dashed curves. The "abnormal" CET regions are highlighted by red rectangular.

5.5 Conclusions

This chapter investigates the "abnormal" CET in metal AM, focusing on the wire-laser DED of Inconel 718 alloy. A processing window has been generalized, reflecting the impact of printing parameters on the “abnormal” CET in the wire-laser DED of Inconel 718. Three representative solidification microstructures were defined, i.e., Lack of Fusion, Normal, and Transitional. The *operando* synchrotron characterization was employed to study the printing behavior under these three printing conditions. Total-scattering analysis has revealed the atomic structure of the melt pool and its evolution during solidification. The icosahedral MRO and FCC-like MRO represented two major types of topological ordering, and they were widely distributed in the melt pool. During rapid solidification, the “abnormal” CET and common grain growth were associated with two distinct evolution paths of the topological orderings in the liquid phase. By coupling it with multi-physics simulation, a fully melted concave region was observed between the wire tip and the rear melt pool. In addition to the presence of topological orderings, the complex thermal conditions and unique melt pool dynamics at the concave region triggered the “abnormal” CET at the local region. Furthermore, this work also provided valuable insights into the “abnormal” CET of other material systems.

The present research not only provided direct evidence of the presence of topological orderings in the liquid metal under AM conditions but also conducted a comprehensive investigation into their effects on rapid solidification. To the author’s best knowledge, this work presents the first total-scattering analysis of the *operando* x-ray diffraction experiment for metal AM. The experiments conducted in this Chapter clarified many long-standing confusions and questions originating from the hypothesis of the “abnormal” CET in metal AM. This work aims to advance modern solidification theory, contributing significantly to both the metal AM and material science communities.

6. Summary

The wire-laser DED process with coaxial wire-laser configuration is an emerging AM technology. A deepening understanding of the printing process is essential for better control of the as-printed microstructure and the production of components with superior properties. This dissertation contributed to the further development of this AM technology through three research topics. These three studies are all relevant to the microstructure evolution during printing, focusing on three different yet important mechanisms relevant to solidification microstructures. Furthermore, *operando* synchrotron x-ray diffraction was employed in all three research chapters for various purposes, which further developed the capability of *operando* synchrotron x-ray techniques in investigating metal AM. The first research chapter focuses on the wire-laser DED under an intentionally constrained energy input that resulted in the presence of unmelted solid particles in the melt pool. The capability of *operando* synchrotron x-ray imaging and diffraction in studying the wire-laser DED process has been comprehensively introduced, especially in probing transient phenomena, such as the remaining carbides in the melt pool. The second research chapter developed a novel deposition strategy to induce an unstable melt pool, thereby modifying the crystallographic texture and mechanical anisotropy of the printed sample. Despite not being the principal portion of this section, synchrotron x-ray diffraction was adopted to monitor the stability of the mushy zone. Based on the understanding accumulated from the previous two chapters, including the wire-laser DED process, solidification behavior, and *operando* synchrotron x-ray characterization, the last research chapter focused on the short-range-ordering-mediated solidification and an “abnormal” columnar-to-equiaxed transformation (CET) in metal AM. The o*perando* synchrotron x-ray characterization and total-scattering analysis played critical roles in this study to reveal the atomic structure of the melt pool and its evolution during the solidification of wire-laser DED.

The new understanding gained from these studies directly influences wire-laser DED and extends to other metal AM technologies, enabling optimization of the printing process and achieving flexible microstructure control. In addition to the *operando* synchrotron x-ray characterization, this dissertation employed multi-physics simulation to investigate the coaxial wire-laser printing behavior. The integration of advanced characterization and numerical modeling has gained valuable insights into revealing the underlying mechanisms involved in the printing process. The further understanding and the comprehensive investigation provided by the present work encourage a broader application of this AM technology.

6.1 Main conclusions

The main conclusions drawn in this dissertation are summarized below.

1. Printing conditions can influence wire melting within the melt pool in the wire-laser DED process, consequently affecting the solidification microstructure. Under a specific printing condition with intentionally decreasing energy input, the feedstock wire only partially melted as it entered the melt pool while still maintaining a stable printing process. Although the wire continued to be heated up by the surrounding melt pool, some solid particles, such as MC-carbide, remained at the bottom region close to the mushy zone. These small particles promoted heterogeneous

nucleation and impeded grain coarsening, resulting in small grains in the region where they are present.

2. The capability of synchrotron x-ray techniques for *operando* studies of metal AM processes has been successfully demonstrated. Full-field x-ray imaging enabled an overview of the printing process and guided the positioning of the focused x-ray beam in the diffraction experiment. X-ray diffraction allowed for the characterization of wire melting, melt pool development, and solidification behavior. By fixing the printhead while scanning the build platform, the time delay in the dynamic diffraction data was translated into the spatial separation between the x-ray beam and the printhead. Thus, a longer probing time could be applied to achieve high-quality diffraction data, even from the liquid phase.

3. A wiggle deposition strategy was developed for the wire-laser DED of 316L SS, which involved an alternating transversal component of scanning. This novel printing strategy wobbled the motion of the melt pool, thereby inducing asymmetric laser absorption and leading to highly dynamic melt flow and complex thermal conditions inside the melt pool. This unique thermal condition can be manipulated to vary the evolution of crystallographic texture during solidification, resulting in a distinct mechanical anisotropy of as-printed samples.

4. The atomic structure of the melt pool was revealed for the first time through experiments. The melt pool of wire-laser DED of Inconel 718 exhibited the presence and wide distribution of two major types of topological ordering: icosahedral MRO and FCC-like MRO. The distribution and size of MROs were less affected by the temperature variation inside the melt pool. The complex composition in Inconel 718 plays a more critical role in generating MROs in the melt pool.

5. The occurrence of the “abnormal” CET in metal AM has been confirmed, and this process preferably consumed the icosahedral MROs in the melt pool. In addition to preexisting MROs, the complex thermal conditions and unique melt-pool dynamics at a specific region of the melt pool were responsible for triggering the “abnormal” CET at the local region. The melt pool in the wire-laser DED of 316L SS was dominated by BCC-like MROs, which may affect the occurrence of “abnormal” CET in this material. In the wire-laser DED process, higher laser power, higher feeding rate, and faster scanning speed are favorable for inducing the “abnormal” CET.

6.2 Recommendations for future work

As summarized above, many important conclusions and findings have been obtained through the three research chapters in this dissertation, which offers inspirational insights into the microstructure control in metal AM. However, several works are worthwhile to continue and explore.

First, as suggested by Chapter 3, a specific melting behavior of feedstock wire can form unmelted solid particles in the melt pool, thereby suppressing the growth of columnar grains. However, in the present investigation, unmelted particles might not be sufficiently abundant to induce the formation of tiny equiaxed grains or change the crystallographic texture. Thus, this effect is expected to be more prominent for materials that consist of a large number of secondary phases with elevated melting temperatures, as is the case with carbides in this study. In addition, the hot-wire function of the wire can preheat the wire feedstock during printing, further facilitating the melting of the matrix of wire feedstocks. Thus, further research can continue by considering these factors.

Second, this dissertation confirmed the feasibility of altering the solidification texture and mechanical anisotropy in the wire-laser DED of 316L SS by controlling the stability of the melt pool. This concept opens up many opportunities for programming the microstructure and property of as-printed samples. For example, by changing the frequency (or characteristic length scale) of wiggling, a variety of texture structures could be obtained. Also, by synergistically and alternatively applying the Bi and Wig depositions at different positions of the build, a single part with locally varied structures and properties can be achieved. More systematic investigations are recommended to achieve this goal.

Third, this dissertation provided experimental insight into the rapid solidification of liquid metal on the atomic scale. Two aspects are expected to be further considered. On the one hand, the current investigation did not offer much information about the chemical orderings in the liquid metal. A more practical approach is tailoring the composition of the deposit and then identifying which element(s) is responsible for the chemical ordering or required for the medium-range topological orderings. Meanwhile, molecular dynamics could be an important tool for accelerating the understanding of atomic orderings in liquid metals if the corresponding potential file is available. More versatile multi-physics simulations are also recommended. On the other hand, additional attention can be drawn to expanding the “abnormal” columnar-to-equiaxial transition (CET) region in printing bulk samples. A large CTE region is desirable for structural components. The printing of bulk samples has greater freedom to adjust the printing strategy. For example, modifying the hatching distance between the two adjacent tracks could influence the melt pool morphology, thereby affecting the “abnormal” CET region.

Last but not least, this dissertation suggests three different applications of *operando* synchrotron x-ray diffraction in the study of wire-laser DED. The special experiment setup has an apparent advantage in monitoring the dynamic microstructural evolution, making it beneficial for relevant studies such as the competitive growth of columnar grains and the formation of grain colonies during rapid solidification. Additionally, unlike previous *operando* diffraction experiments that scanned the entire sample, the current diffraction dataset summarizes information from a large number of grains in a relatively static region. This characterization strategy is critical for performing a quantitative analysis of the solidification front in which only a limited number of grains are solidified. Therefore, it is worthwhile to further explore the applicability of synchrotron X-ray techniques for *operando* studies of metal AM processes.

References:

[1] P. Kürnsteiner, M.B. Wilms, A. Weisheit, B. Gault, E.A. Jägle, D. Raabe, High-strength Damascus steel by additive manufacturing, Nature. 582 (2020) 515–519. https://doi.org/10.1038/s41586-020-2409-3.

[2] D. Gu, X. Shi, R. Poprawe, D.L. Bourell, R. Setchi, J. Zhu, Material-structure-performance integrated laser-metal additive manufacturing, Science. 372 (2021) eabg1487. https://doi.org/10.1126/science.abg1487.

[3] D. Herzog, V. Seyda, E. Wycisk, C. Emmelmann, Additive manufacturing of metals, Acta Mater. 117 (2016) 371–392. https://doi.org/10.1016/j.actamat.2016.07.019.

[4] S.A. Khairallah, A.T. Anderson, A. Rubenchik, W.E. King, Laser powder-bed fusion additive manufacturing: Physics of complex melt flow and formation mechanisms of pores, spatter, and denudation zones, Acta Mater. 108 (2016) 36–45. https://doi.org/10.1016/j.actamat.2016.02.014.

[5] B. Blinn, P. Lion, O. Jordan, S. Meiniger, S. Mischliwski, C. Tepper, C. Gläßner, J.C. Aurich, M. Weigold, T. Beck, Process-influenced fatigue behavior of AISI 316L manufactured by powder- and wire-based Laser Direct Energy Deposition, Mater. Sci. Eng. A. 818 (2021) 141383. https://doi.org/10.1016/j.msea.2021.141383.

[6] G.L. Knapp, M. Gussev, A. Shyam, T. Feldhausen, A. Plotkowski, Microstructure, deformation and fracture mechanisms in Al-4043 alloy produced by laser hot-wire additive manufacturing, Addit. Manuf. 59 (2022) 103150. https://doi.org/10.1016/j.addma.2022.103150.

[7] M. Lalegani Dezaki, A. Serjouei, A. Zolfagharian, M. Fotouhi, M. Moradi, M.K.A. Ariffin, M. Bodaghi, A review on additive/subtractive hybrid manufacturing of directed energy deposition

(DED) process, Adv. Powder Mater. 1 (2022) 100054. https://doi.org/10.1016/j.apmate.2022.100054.

[8] Z. Li, S. Sui, X. Ma, H. Tan, C. Zhong, G. Bi, A.T. Clare, A. Gasser, J. Chen, High deposition rate powder- and wire-based laser directed energy deposition of metallic materials: A review, Int. J. Mach. Tools Manuf. 181 (2022) 103942. https://doi.org/10.1016/j.ijmachtools.2022.103942.

[9] H. Lane D., G. Michelle L., G. Donald L., P. Gray A., Energetic Additive manufacturing ProcessWith Feed Wire, US006143378A, 2000.

[10] M. Bambach, I. Sizova, F. Kies, C. Haase, Directed energy deposition of Inconel 718 powder, cold and hot wire using a six-beam direct diode laser set-up, Addit. Manuf. 47 (2021) 102269. https://doi.org/10.1016/j.addma.2021.102269.

[11] C. Leyens, E. Beyer, Innovations in laser cladding and direct laser metal deposition, in: Laser Surf. Eng., Elsevier, 2015: pp. 181–192. https://doi.org/10.1016/B978-1-78242-074-3.00008-8.

[12] C. Zhao, Q. Guo, X. Li, N. Parab, K. Fezzaa, W. Tan, L. Chen, T. Sun, Bulk-Explosion-Induced Metal Spattering During Laser Processing, Phys. Rev. X. 9 (2019) 021052. https://doi.org/10.1103/PhysRevX.9.021052.

[13] N. Kouraytem, X. Li, R. Cunningham, C. Zhao, N. Parab, T. Sun, A.D. Rollett, A.D. Spear, W. Tan, Effect of Laser-Matter Interaction on Molten Pool Flow and Keyhole Dynamics, Phys. Rev. Appl. 11 (2019) 064054. https://doi.org/10.1103/PhysRevApplied.11.064054.

[14] J.P. Oliveira, T.G. Santos, R.M. Miranda, Revisiting fundamental welding concepts to improve additive manufacturing: From theory to practice, Prog. Mater. Sci. 107 (2020) 100590. https://doi.org/10.1016/j.pmatsci.2019.100590.

[15] S.M. Thompson, L. Bian, N. Shamsaei, A. Yadollahi, An overview of Direct Laser Deposition for additive manufacturing; Part I: Transport phenomena, modeling and diagnostics, Addit. Manuf. 8 (2015) 36–62. https://doi.org/10.1016/j.addma.2015.07.001.

[16] M. Kotar, M. Fujishima, G.N. Levy, E. Govekar, Advances in the understanding of the annular laser beam wire cladding process, J. Mater. Process. Technol. 294 (2021) 117105. https://doi.org/10.1016/j.jmatprotec.2021.117105.

[17] A. Aggarwal, A. Chouhan, S. Patel, D.K. Yadav, A. Kumar, A.R. Vinod, K.G. Prashanth, N.P. Gurao, Role of impinging powder particles on melt pool hydrodynamics, thermal behaviour and microstructure in laser-assisted DED process: A particle-scale DEM – CFD – CA approach, Int. J. Heat Mass Transf. 158 (2020) 119989. https://doi.org/10.1016/j.ijheatmasstransfer.2020.119989.

[18] T. DebRoy, H.L. Wei, J.S. Zuback, T. Mukherjee, J.W. Elmer, J.O. Milewski, A.M. Beese, A. Wilson-Heid, A. De, W. Zhang, Additive manufacturing of metallic components – Process, structure and properties, Prog. Mater. Sci. 92 (2018) 112–224. https://doi.org/10.1016/j.pmatsci.2017.10.001.

[19] P. Kürnsteiner, M.B. Wilms, A. Weisheit, P. Barriobero-Vila, E.A. Jägle, D. Raabe, Massive nanoprecipitation in an Fe-19Ni- x Al maraging steel triggered by the intrinsic heat treatment during laser metal deposition, Acta Mater. 129 (2017) 52–60. https://doi.org/10.1016/j.actamat.2017.02.069.

[20] J.-O. Andersson, T. Helander, L. Höglund, P. Shi, B. Sundman, Thermo-Calc & DICTRA, computational tools for materials science, Calphad. 26 (2002) 273–312. https://doi.org/10.1016/S0364-5916(02)00037-8.

[21] N.C. Ferreri, S.C. Vogel, M. Knezevic, Determining volume fractions of γ, γ′, γ″, δ, and MC-carbide phases in Inconel 718 as a function of its processing history using an advanced neutron diffraction procedure, Mater. Sci. Eng. A. 781 (2020) 139228. https://doi.org/10.1016/j.msea.2020.139228.

[22] Y. Wang, F. Lia, K. Wang, K. McNamara, Y. Ji, X. Chong, S.-L. Shang, Z.-K. Liu, R.P. Martukanitz, L.-Q. Chen, A thermochemical database from high-throughput first-principles calculations and its application to analyzing phase evolution in AM-fabricated IN718, Acta Mater. 240 (2022) 118331. https://doi.org/10.1016/j.actamat.2022.118331.

[23] R. Krakow, D.N. Johnstone, A.S. Eggeman, D. Hünert, M.C. Hardy, C.M.F. Rae, P.A. Midgley, On the crystallography and composition of topologically close-packed phases in ATI 718Plus®, Acta Mater. 130 (2017) 271–280. https://doi.org/10.1016/j.actamat.2017.03.038.

[24] R.M. R, M. Agilan, D. Mohan, G. Phanikumar, Integrated experimental and simulation approach to establish the effect of elemental segregation in Inconel 718 welds, Materialia. 26 (2022) 101593. https://doi.org/10.1016/j.mtla.2022.101593.

[25] E. Hosseini, V.A. Popovich, A review of mechanical properties of additively manufactured Inconel 718, Addit. Manuf. 30 (2019) 100877. https://doi.org/10.1016/j.addma.2019.100877.

[26] L. Xu, Z. Chai, H. Chen, X. Zhang, J. Xie, X. Chen, Tailoring Laves phase and mechanical properties of directed energy deposited Inconel 718 thin-wall via a gradient laser power method, Mater. Sci. Eng. A. 824 (2021) 141822. https://doi.org/10.1016/j.msea.2021.141822.

[27] Z. Yang, L. Zhu, S. Wang, J. Ning, Y. Dun, G. Meng, P. Xue, P. Xu, B. Xin, Effects of ultrasound on multilayer forming mechanism of Inconel 718 in directed energy deposition, Addit.

Manuf. 48 (2021) 102462. https://doi.org/10.1016/j.addma.2021.102462.

[28] A. Saboori, A. Aversa, G. Marchese, S. Biamino, M. Lombardi, P. Fino, Microstructure and Mechanical Properties of AISI 316L Produced by Directed Energy Deposition-Based Additive Manufacturing: A Review, Appl. Sci. 10 (2020) 3310. https://doi.org/10.3390/app10093310.

[29] Z.E. Tan, J.H.L. Pang, J. Kaminski, H. Pepin, Characterisation of porosity, density, and microstructure of directed energy deposited stainless steel AISI 316L, Addit. Manuf. 25 (2019) 286–296. https://doi.org/10.1016/j.addma.2018.11.014.

[30] X. Chen, J. Li, X. Cheng, B. He, H. Wang, Z. Huang, Microstructure and mechanical properties of the austenitic stainless steel 316L fabricated by gas metal arc additive manufacturing, Mater. Sci. Eng. A. 703 (2017) 567–577. https://doi.org/10.1016/j.msea.2017.05.024.

[31] A. Saboori, A. Aversa, F. Bosio, E. Bassini, E. Librera, M. De Chirico, S. Biamino, D. Ugues, P. Fino, M. Lombardi, An investigation on the effect of powder recycling on the microstructure and mechanical properties of AISI 316L produced by Directed Energy Deposition, Mater. Sci. Eng. A. 766 (2019) 138360. https://doi.org/10.1016/j.msea.2019.138360.

[32] A.T. Polonsky, W.C. Lenthe, M.P. Echlin, V. Livescu, G.T. Gray, T.M. Pollock, Solidification-driven orientation gradients in additively manufactured stainless steel, Acta Mater. 183 (2020) 249–260. https://doi.org/10.1016/j.actamat.2019.10.047.

[33] J. Shao, G. Yu, S. Li, X. He, C. Tian, B. Dong, Crystal growth control of Ni-based alloys by modulation of the melt pool morphology in DED, J. Alloys Compd. 898 (2022) 162976. https://doi.org/10.1016/j.jallcom.2021.162976.

[34] N. Shamsaei, A. Yadollahi, L. Bian, S.M. Thompson, An overview of Direct Laser Deposition

for additive manufacturing; Part II: Mechanical behavior, process parameter optimization and control, Addit. Manuf. 8 (2015) 12–35. https://doi.org/10.1016/j.addma.2015.07.002.

[35] A. Saboori, D. Gallo, S. Biamino, P. Fino, M. Lombardi, An Overview of Additive Manufacturing of Titanium Components by Directed Energy Deposition: Microstructure and Mechanical Properties, Appl. Sci. 7 (2017) 883. https://doi.org/10.3390/app7090883.

[36] K. Sofinowski, M. Wittwer, M. Seita, Encoding data into metal alloys using laser powder bed fusion, Addit. Manuf. 52 (2022) 102683. https://doi.org/10.1016/j.addma.2022.102683.

[37] Y. Wang, J. Shi, Texture control of Inconel 718 superalloy in laser additive manufacturing by an external magnetic field, J. Mater. Sci. 54 (2019) 9809–9823. https://doi.org/10.1007/s10853-019-03569-7.

[38] Y. Wang, J. Shi, Microstructure and Properties of Inconel 718 Fabricated by Directed Energy Deposition with In-Situ Ultrasonic Impact Peening, Metall. Mater. Trans. B. 50 (2019) 2815–2827. https://doi.org/10.1007/s11663-019-01672-3.

[39] L. Xi, P. Wang, K.G. Prashanth, H. Li, H.V. Prykhodko, S. Scudino, I. Kaban, Effect of TiB2 particles on microstructure and crystallographic texture of Al-12Si fabricated by selective laser melting, J. Alloys Compd. 786 (2019) 551–556. https://doi.org/10.1016/j.jallcom.2019.01.327.

[40] C.H. Ng, M.J. Bermingham, M.S. Dargusch, Controlling grain size, morphology and texture in additively manufactured β-titanium alloy with super transus hot isostatic pressing, Addit. Manuf. 59 (2022) 103176. https://doi.org/10.1016/j.addma.2022.103176.

[41] A. Carrozza, A. Aversa, F. Mazzucato, E. Bassini, D. Manfredi, S. Biamino, A. Valente, P. Fino, An investigation on the effect of different multi-step heat treatments on the microstructure,

texture and mechanical properties of the DED-produced Ti-6Al-4V alloy, Mater. Charact. 189 (2022) 111958. https://doi.org/10.1016/j.matchar.2022.111958.

[42] O. Gokcekaya, T. Ishimoto, S. Hibino, J. Yasutomi, T. Narushima, T. Nakano, Unique crystallographic texture formation in Inconel 718 by laser powder bed fusion and its effect on mechanical anisotropy, Acta Mater. 212 (2021) 116876. https://doi.org/10.1016/j.actamat.2021.116876.

[43] H.L. Wei, J. Mazumder, T. DebRoy, Evolution of solidification texture during additive manufacturing, Sci. Rep. 5 (2015) 16446. https://doi.org/10.1038/srep16446.

[44] L.L. Parimi, R.G. A., D. Clark, M.M. Attallah, Microstructural and texture development in direct laser fabricated IN718, Mater. Charact. 89 (2014) 102–111. https://doi.org/10.1016/j.matchar.2013.12.012.

[45] P. Fernandez-Zelaia, M.M. Kirka, S.N. Dryepondt, M.N. Gussev, Crystallographic texture control in electron beam additive manufacturing via conductive manipulation, Mater. Des. 195 (2020) 109010. https://doi.org/10.1016/j.matdes.2020.109010.

[46] L. Thijs, K. Kempen, J.-P. Kruth, J. Van Humbeeck, Fine-structured aluminium products with controllable texture by selective laser melting of pre-alloyed AlSi10Mg powder, Acta Mater. 61 (2013) 1809–1819. https://doi.org/10.1016/j.actamat.2012.11.052.

[47] J.G. Pauza, W.A. Tayon, A.D. Rollett, Computer simulation of microstructure development in powder-bed additive manufacturing with crystallographic texture, Model. Simul. Mater. Sci. Eng. 29 (2021) 055019. https://doi.org/10.1088/1361-651X/ac03a6.

[48] J.J. Blecher, T.A. Palmer, T. DebRoy, Solidification Map of a Nickel-Base Alloy, Metall. Mater.

Trans. A. 45 (2014) 2142–2151. https://doi.org/10.1007/s11661-013-2149-1.

[49] R. Shi, S.A. Khairallah, T.T. Roehling, T.W. Heo, J.T. McKeown, M.J. Matthews, Microstructural control in metal laser powder bed fusion additive manufacturing using laser beam shaping strategy, Acta Mater. 184 (2020) 284–305. https://doi.org/10.1016/j.actamat.2019.11.053.

[50] P. Liu, Z. Wang, Y. Xiao, M.F. Horstemeyer, X. Cui, L. Chen, Insight into the mechanisms of columnar to equiaxed grain transition during metallic additive manufacturing, Addit. Manuf. 26 (2019) 22–29. https://doi.org/10.1016/j.addma.2018.12.019.

[51] M.J. Bermingham, D.H. StJohn, J. Krynen, S. Tedman-Jones, M.S. Dargusch, Promoting the columnar to equiaxed transition and grain refinement of titanium alloys during additive manufacturing, Acta Mater. 168 (2019) 261–274. https://doi.org/10.1016/j.actamat.2019.02.020.

[52] J. Donoghue, A.E. Davis, C.S. Daniel, A. Garner, F. Martina, J. Quinta da Fonseca, P.B. Prangnell, On the observation of annealing twins during simulating β-grain refinement in Ti–6Al–4V high deposition rate AM with in-process deformation, Acta Mater. 186 (2020) 229–241. https://doi.org/10.1016/j.actamat.2020.01.009.

[53] M. Rappaz, Ph. Jarry, G. Kurtuldu, J. Zollinger, Solidification of Metallic Alloys: Does the Structure of the Liquid Matter?, Metall. Mater. Trans. A. 51 (2020) 2651–2664. https://doi.org/10.1007/s11661-020-05770-9.

[54] Y.-C. Hu, H. Tanaka, Revealing the role of liquid preordering in crystallisation of supercooled liquids, Nat. Commun. 13 (2022) 4519. https://doi.org/10.1038/s41467-022-32241-z.

[55] I. Cazic, J. Zollinger, S. Mathieu, M. El Kandaoui, P. Plapper, B. Appolaire, New insights into the origin of fine equiaxed microstructures in additively manufactured Inconel 718, Scr. Mater.

195 (2021) 113740. https://doi.org/10.1016/j.scriptamat.2021.113740.

[56] G. Kurtuldu, P. Jarry, M. Rappaz, Influence of Cr on the nucleation of primary Al and formation of twinned dendrites in Al–Zn–Cr alloys: Can icosahedral solid clusters play a role?, Acta Mater. 61 (2013) 7098–7108. https://doi.org/10.1016/j.actamat.2013.07.056.

[57] M. Buttard, G. Martin, P. Harrison, E.F. Rauch, B. Chéhab, P. Jarry, J.-J. Blandin, P. Donnadieu, Evidence that the liquid structure affects the nucleation of the primary metastable L12-Al3Zr in additive manufacturing, Scr. Mater. 226 (2023) 115212. https://doi.org/10.1016/j.scriptamat.2022.115212.

[58] M. Buttard, G. Martin, X. Bataillon, G. Renou, P. Lhuissier, J. Villanova, B. Chehab, P. Jarry, J.-J. Blandin, P. Donnadieu, Towards an alloy design strategy by tuning liquid local ordering: What solidification of an Al-alloy designed for laser powder bed fusion teaches us, Addit. Manuf. 61 (2023) 103313. https://doi.org/10.1016/j.addma.2022.103313.

[59] L. Monier, M. Buttard, M. Veron, J.-J. Blandin, G. Martin, F. Villaret, Y. Shen, B. Yrieix, C. Ernould, J. Guyon, A. Despres, On the origin of grain refinement and twin boundaries in as-fabricated austenitic stainless steels produced by laser powder bed fusion, Addit. Manuf. 61 (2023) 103351. https://doi.org/10.1016/j.addma.2022.103351.

[60] C. Galera-Rueda, X. Jin, J. LLorca, M.T. Pérez-Prado, Icosahedral quasicrystal enhanced nucleation in commercially pure Ni processed by selective laser melting, Scr. Mater. 211 (2022) 114512. https://doi.org/10.1016/j.scriptamat.2022.114512.

[61] I. Cazic, J. Zollinger, M. Engstler, J. Ghanbaja, T. Schenk, M. El Kandaoui, B. Appolaire, Nucleation burst in additively manufactured Inconel 718: 3D characterization of ISRO-induced

equiaxed microstructure, Addit. Manuf. 66 (2023) 103458. https://doi.org/10.1016/j.addma.2023.103458.

[62] D. Chen, J. Wang, C. Zhang, Coupling phase-field model and CFD for hot cracking predictions of Al-Li alloys, Comput. Mater. Sci. 192 (2021) 110361. https://doi.org/10.1016/j.commatsci.2021.110361.

[63] A. Pasturel, N. Jakse, Chemically induced structural heterogeneities and their relationship with component dynamics in a binary metallic liquid, Appl. Phys. Lett. 110 (2017) 121902. https://doi.org/10.1063/1.4978392.

[64] M. Leocmach, H. Tanaka, Roles of icosahedral and crystal-like order in the hard spheres glass transition, Nat. Commun. 3 (2012) 974. https://doi.org/10.1038/ncomms1974.

[65] Y. Yuan, D.S. Kim, J. Zhou, D.J. Chang, F. Zhu, Y. Nagaoka, Y. Yang, M. Pham, S.J. Osher, O. Chen, P. Ercius, A.K. Schmid, J. Miao, Three-dimensional atomic packing in amorphous solids with liquid-like structure, Nat. Mater. 21 (2022) 95–102. https://doi.org/10.1038/s41563-021-01114-z.

[66] D. Holland-Moritz, T. Schenk, V. Simonet, R. Bellissent, P. Convert, T. Hansen, Short-range order in undercooled melts forming quasicrystals and approximants, J. Alloys Compd. 342 (2002) 77–81. https://doi.org/10.1016/S0925-8388(02)00142-1.

[67] D. Holland-Moritz, T. Schenk, R. Bellissent, V. Simonet, K. Funakoshi, J.M. Merino, T. Buslaps, S. Reutzel, Short-range order in undercooled Co melts, J. Non-Cryst. Solids. 312–314 (2002) 47–51. https://doi.org/10.1016/S0022-3093(02)01648-4.

[68] G.W. Lee, A.K. Gangopadhyay, K.F. Kelton, R.W. Hyers, T.J. Rathz, J.R. Rogers, D.S.

Robinson, Difference in Icosahedral Short-Range Order in Early and Late Transition Metal Liquids, Phys. Rev. Lett. 93 (2004) 037802. https://doi.org/10.1103/PhysRevLett.93.037802.

[69] T. Schenk, D. Holland-Moritz, V. Simonet, R. Bellissent, D.M. Herlach, Icosahedral Short-Range Order in Deeply Undercooled Metallic Melts, Phys. Rev. Lett. 89 (2002) 075507. https://doi.org/10.1103/PhysRevLett.89.075507.

[70] F.C. Frank, Supercooling of liquids, Proc. R. Soc. Lond. Ser. A. 215 (1952) 43–46. https://doi.org/10.1098/rspa.1952.0194.

[71] K.F. Kelton, G.W. Lee, A.K. Gangopadhyay, R.W. Hyers, T.J. Rathz, J.R. Rogers, M.B. Robinson, D.S. Robinson, First X-Ray Scattering Studies on Electrostatically Levitated Metallic Liquids: Demonstrated Influence of Local Icosahedral Order on the Nucleation Barrier, Phys. Rev. Lett. 90 (2003) 195504. https://doi.org/10.1103/PhysRevLett.90.195504.

[72] A. Di Cicco, A. Trapananti, S. Faggioni, A. Filipponi, Is There Icosahedral Ordering in Liquid and Undercooled Metals?, Phys. Rev. Lett. 91 (2003) 135505. https://doi.org/10.1103/PhysRevLett.91.135505.

[73] K.H. Kuo, Mackay, Anti-Mackay, Double-Mackay, Pseudo-Mackay, and Related Icosahedral Shell Clusters, in: I. Hargittai, B. Hargittai (Eds.), Sci. Cryst. Struct., Springer International Publishing, Cham, 2015: pp. 43–52. https://doi.org/10.1007/978-3-319-19827-9_5.

[74] J.L. Bartlett, B.P. Croom, J. Burdick, D. Henkel, X. Li, Revealing mechanisms of residual stress development in additive manufacturing via digital image correlation, Addit. Manuf. 22 (2018) 1–12. https://doi.org/10.1016/j.addma.2018.04.025.

[75] M. Motta, A.G. Demir, B. Previtali, High-speed imaging and process characterization of

coaxial laser metal wire deposition, Addit. Manuf. 22 (2018) 497–507. https://doi.org/10.1016/j.addma.2018.05.043.

[76] H. Gaja, F. Liou, Defects monitoring of laser metal deposition using acoustic emission sensor, Int. J. Adv. Manuf. Technol. 90 (2017) 561–574. https://doi.org/10.1007/s00170-016-9366-x.

[77] R. Hu, M. Luo, T. Liu, L. Liang, A. Huang, D. Trushnikov, K.P. Karunakaran, S. Pang, Thermal fluid dynamics of liquid bridge transfer in laser wire deposition 3D printing, Sci. Technol. Weld. Join. 24 (2019) 401–411. https://doi.org/10.1080/13621718.2019.1591039.

[78] S. Wei, G. Wang, Y.C. Shin, Y. Rong, Comprehensive modeling of transport phenomena in laser hot-wire deposition process, Int. J. Heat Mass Transf. 125 (2018) 1356–1368. https://doi.org/10.1016/j.ijheatmasstransfer.2018.04.164.

[79] L. Liang, R. Hu, J. Wang, A. Huang, S. Pang, A thermal fluid mechanical model of stress evolution for wire feeding-based laser additive manufacturing, J. Manuf. Process. 69 (2021) 602–612. https://doi.org/10.1016/j.jmapro.2021.08.008.

[80] S.A. Khairallah, A.A. Martin, J.R.I. Lee, G. Guss, N.P. Calta, J.A. Hammons, M.H. Nielsen, K. Chaput, E. Schwalbach, M.N. Shah, M.G. Chapman, T.M. Willey, A.M. Rubenchik, A.T. Anderson, Y.M. Wang, M.J. Matthews, W.E. King, Controlling interdependent meso-nanosecond dynamics and defect generation in metal 3D printing, Science. 368 (2020) 660–665. https://doi.org/10.1126/science.aay7830.

[81] Z. Ren, L. Gao, S.J. Clark, K. Fezzaa, P. Shevchenko, A. Choi, W. Everhart, A.D. Rollett, L. Chen, T. Sun, Machine learning–aided real-time detection of keyhole pore generation in laser powder bed fusion, Science. 379 (2023) 89–94. https://doi.org/10.1126/science.add4667.

[82] J.T. McKeown, K. Zweiacker, C. Liu, D.R. Coughlin, A.J. Clarke, J.K. Baldwin, J.W. Gibbs, J.D. Roehling, S.D. Imhoff, P.J. Gibbs, D. Tourret, J.M.K. Wiezorek, G.H. Campbell, Time-Resolved In Situ Measurements During Rapid Alloy Solidification: Experimental Insight for Additive Manufacturing, JOM. 68 (2016) 985–999. https://doi.org/10.1007/s11837-015-1793-x.

[83] A. Plotkowski, K. Saleeby, C.M. Fancher, J. Haley, G. Madireddy, K. An, R. Kannan, T. Feldhausen, Y. Lee, D. Yu, C. Leach, J. Vaughan, S.S. Babu, Operando neutron diffraction reveals mechanisms for controlled strain evolution in 3D printing, Nat. Commun. 14 (2023) 4950. https://doi.org/10.1038/s41467-023-40456-x.

[84] C. Zhao, K. Fezzaa, R.W. Cunningham, H. Wen, F. De Carlo, L. Chen, A.D. Rollett, T. Sun, Real-time monitoring of laser powder bed fusion process using high-speed X-ray imaging and diffraction, Sci. Rep. 7 (2017) 3602. https://doi.org/10.1038/s41598-017-03761-2.

[85] H. Wang, F.E. Pfefferkorn, S.J. Wolff, Investigation of pore formation mechanisms induced by spherical-powder delivery in directed energy deposition using in situ high-speed X-ray imaging, Addit. Manuf. Lett. 3 (2022) 100050. https://doi.org/10.1016/j.addlet.2022.100050.

[86] Q. Guo, C. Zhao, M. Qu, L. Xiong, S.M.H. Hojjatzadeh, L.I. Escano, N.D. Parab, K. Fezzaa, T. Sun, L. Chen, In-situ full-field mapping of melt flow dynamics in laser metal additive manufacturing, Addit. Manuf. 31 (2020) 100939. https://doi.org/10.1016/j.addma.2019.100939.

[87] Q. Guo, M. Qu, C.A. Chuang, L. Xiong, A. Nabaa, Z.A. Young, Y. Ren, P. Kenesei, F. Zhang, L. Chen, Phase transformation dynamics guided alloy development for additive manufacturing, Addit. Manuf. 59 (2022) 103068. https://doi.org/10.1016/j.addma.2022.103068.

[88] Y. Chen, S.J. Clark, D.M. Collins, S. Marussi, S.A. Hunt, D.M. Fenech, T. Connolley, R.C.

Atwood, O.V. Magdysyuk, G.J. Baxter, M.A. Jones, C.L.A. Leung, P.D. Lee, Correlative Synchrotron X-ray Imaging and Diffraction of Directed Energy Deposition Additive Manufacturing, Acta Mater. 209 (2021) 116777. https://doi.org/10.1016/j.actamat.2021.116777.

[89] J.W. Elmer, J. Wong, T. Ressler, In-situ observations of phase transformations during solidification and cooling of austenitic stainless steel welds using time-resolved x-ray diffraction, Scr. Mater. 43 (2000) 751–757. https://doi.org/10.1016/S1359-6462(00)00481-4.

[90] D.W. Brown, A. Losko, J.S. Carpenter, B. Clausen, J.C. Cooley, V. Livescu, P. Kenesei, J.-S. Park, T.J. Stockman, M. Strantza, In-Situ High-Energy X-ray Diffraction During a Linear Deposition of 308 Stainless Steel via Wire Arc Additive Manufacture, Metall. Mater. Trans. A. 51 (2020) 1379–1394. https://doi.org/10.1007/s11661-019-05605-2.

[91] E. Takeshi, S.J.L. Billinge, The Method of Total Scattering and Atomic Pair Distribution Function Analysis, in: Pergamon Mater. Ser., Elsevier, 2012: pp. 55–111. https://doi.org/10.1016/B978-0-08-097133-9.00003-4.

[92] J. Als-Nielsen, D. McMorrow, Elements of Modern X-ray Physics, John Wiley & Sons (2011).

[93] H. Reichert, O. Klein, H. Dosch, M. Denk, T. Lippmann, G. Reiter, Observation of ®ve-fold local symmetry in liquid lead, 408 (2000) 3.

[94] S.D. Shastri, P. Kenesei, A. Mashayekhi, P.A. Shade, Focusing with saw-tooth refractive lenses at a high-energy X-ray beamline, J. Synchrotron Radiat. 27 (2020) 590–598. https://doi.org/10.1107/S1600577520003665.

[95] C.A. Schneider, W.S. Rasband, K.W. Eliceiri, NIH Image to ImageJ: 25 years of image analysis, Nat. Methods. 9 (2012) 671–675. https://doi.org/10.1038/nmeth.2089.

[96] B.H. Toby, R.B. Von Dreele, *GSAS-II*: the genesis of a modern open-source all purpose crystallography software package, J. Appl. Crystallogr. 46 (2013) 544–549. https://doi.org/10.1107/S0021889813003531.

[97] M. Bayat, A. Thanki, S. Mohanty, A. Witvrouw, S. Yang, J. Thorborg, N.S. Tiedje, J.H. Hattel, Keyhole-induced porosities in Laser-based Powder Bed Fusion (L-PBF) of Ti6Al4V: High-fidelity modelling and experimental validation, Addit. Manuf. 30 (2019) 100835. https://doi.org/10.1016/j.addma.2019.100835.

[98] Q. Chen, Y. Zhao, S. Strayer, Y. Zhao, K. Aoyagi, Y. Koizumi, A. Chiba, W. Xiong, A.C. To, Elucidating the effect of preheating temperature on melt pool morphology variation in Inconel 718 laser powder bed fusion via simulation and experiment, Addit. Manuf. (2020) 101642. https://doi.org/10.1016/j.addma.2020.101642.

[99] S. Zhou, X. Dai, X. Zeng, Effects of processing parameters on structure of Ni-based WC composite coatings during laser induction hybrid rapid cladding, Appl. Surf. Sci. 255 (2009) 8494–8500. https://doi.org/10.1016/j.apsusc.2009.05.161.

[100] E.W. Teichmann, J. Kelbassa, A. Gasser, S. Tarner, J.H. Schleifenbaum, Effect of wire feeder force control on laser metal deposition process using coaxial laser head, J. Laser Appl. 33 (2021) 012041. https://doi.org/10.2351/7.0000304.

[101] R.N. Abdullaev, R.A. Khairulin, S.V. Stankus, Yu.M. Kozlovskii, Density and volumetric expansion of the Inconel 718 alloy in solid and liquid states, Thermophys. Aeromechanics. 26 (2019) 785–788. https://doi.org/10.1134/S0869864319050160.

[102] S.A. Oh, R.E. Lim, J.W. Aroh, A.C. Chuang, B.J. Gould, J.V. Bernier, N. Parab, T. Sun,

R.M. Suter, A.D. Rollett, Microscale Observation via High-Speed X-ray Diffraction of Alloy 718 During In Situ Laser Melting, JOM. 73 (2021) 212–222. https://doi.org/10.1007/s11837-020-04481-1.

[103] A.M. Nair, G. Muvvala, S. Sarkar, A.K. Nath, Real-time detection of cooling rate using pyrometers in tandem in laser material processing and directed energy deposition, Mater. Lett. 277 (2020) 128330. https://doi.org/10.1016/j.matlet.2020.128330.

[104] L. Nastac, D.M. Stefanescu, Computational modeling of NbC/laves formation in INCONEL 718 equiaxed castings, Metall. Mater. Trans. A. 28 (1997) 1582–1587. https://doi.org/10.1007/s11661-997-0220-5.

[105] Y. Hu, X. Lin, Y. Li, Y. Ou, X. Gao, Q. Zhang, W. Li, W. Huang, Microstructural evolution and anisotropic mechanical properties of Inconel 625 superalloy fabricated by directed energy deposition, J. Alloys Compd. 870 (2021) 159426. https://doi.org/10.1016/j.jallcom.2021.159426.

[106] C. Wang, T.G. Liu, P. Zhu, Y.H. Lu, T. Shoji, Study on microstructure and tensile properties of 316L stainless steel fabricated by CMT wire and arc additive manufacturing, Mater. Sci. Eng. A. 796 (2020) 140006. https://doi.org/10.1016/j.msea.2020.140006.

[107] W.J. Sames, K.A. Unocic, R.R. Dehoff, T. Lolla, S.S. Babu, Thermal effects on microstructural heterogeneity of Inconel 718 materials fabricated by electron beam melting, J. Mater. Res. 29 (2014) 1920–1930. https://doi.org/10.1557/jmr.2014.140.

[108] D. Gürsoy, F. De Carlo, X. Xiao, C. Jacobsen, TomoPy: a framework for the analysis of synchrotron tomographic data, J. Synchrotron Radiat. 21 (2014) 1188–1193. https://doi.org/10.1107/S1600577514013939.

[109] A. Molinari, G.R. Canova, S. Ahzi, A Self Consistent Approach of the Large Deformation polycrystal viscoplasticity, Acta Metall. 35 (1987) 2983–2994. https://doi.org/10.1016/0001-6160(87)90297-5.

[110] S. Mercier, A. Molinari, Homogenization of elastic-viscoplastic heterogeneous materials: Self-consistent and Mori-Tanaka schemes, Int. J. Plast. 25 (2009) 1024–1048. https://doi.org/10.1016/j.ijplas.2008.08.006.

[111] H. Wang, P.D. Wu, C.N. Tomé, Y. Huang, A finite strain elastic-viscoplastic self-consistent model for polycrystalline materials, J. Mech. Phys. Solids. 58 (2010) 594–612. https://doi.org/10.1016/j.jmps.2010.01.004.

[112] C Calhoun, Thermomechanical response of polycrystalline α-uranium, PhD Thesis, University of Virginia, 2016.

[113] I.J. Beyerlein, C.N. Tomé, A dislocation-based constitutive law for pure Zr including temperature effects, Int. J. Plast. 24 (2008) 867–895. https://doi.org/10.1016/j.ijplas.2007.07.017.

[114] J.W. Hutchinson, Bounds and Self-Consistent Estimates for Creep of Polycrystalline Materials, Proc. R. Soc. Math. Phys. Eng. Sci. 348 (1976) 101–127. https://doi.org/10.1098/rspa.1976.0027.

[115] J. Pan, J.R. Rice, Rate sensitivity of plastic flow and implications for yield-surface vertices, Int. J. Solids Struct. 19 (1983) 973–987.

[116] R.J. Asaro, A. Needleman, Overview texture development and strain hardening in rate dependent polycrystals, Acta Mater. 33 (1985) 923–953.

[117] S. Kok, A.J. Beaudoin, D.A. Tortorelli, A polycrystal plasticity model based on the

mechanical threshold, Int. J. Plast. 18 (2002) 715–741.

[118] R.A. Lebensohn, C.N. Tome, A self-consistent anisotropic approach for the simulation of plastic deformation and texture development of polycrystals: application to zirconium alloys, Acta Metall. 41 (1993) 2611–2624.

[119] R. Masson, M. Bornert, P. Suquet, A. Zaoui, An affine formulation for the prediction of the effective properties of nonlinear composites and polycrystals, J. Mech. Phys. Solids. 48 (2000) 1203–1227. https://doi.org/10.1016/S0022-5096(99)00071-X.

[120] R.A. Lebensohn, C.N. Tomé, P.P. CastaÑeda, Self-consistent modelling of the mechanical behaviour of viscoplastic polycrystals incorporating intragranular field fluctuations, Philos. Mag. 87 (2007) 4287–4322. https://doi.org/10.1080/14786430701432619.

[121] H. Qiao, X.Q. Guo, A.L. Oppedal, H. El Kadiri, P.D. Wu, S.R. Agnew, Twin-induced hardening in extruded Mg alloy AM30, Mater. Sci. Eng. A. 687 (2017) 17–27. https://doi.org/10.1016/j.msea.2016.12.123.

[122] B. Zheng, J.C. Haley, N. Yang, J. Yee, K.W. Terrassa, Y. Zhou, E.J. Lavernia, J.M. Schoenung, On the evolution of microstructure and defect control in 316L SS components fabricated via directed energy deposition, Mater. Sci. Eng. A. 764 (2019) 138243. https://doi.org/10.1016/j.msea.2019.138243.

[123] W. Liu, C. Chen, S. Shuai, R. Zhao, L. Liu, X. Wang, T. Hu, W. Xuan, C. Li, J. Yu, J. Wang, R. Zhongming, Study of pore defect and mechanical properties in selective laser melted Ti6Al4V alloy based on X-ray computed tomography, Mater. Sci. Eng. A. 797 (2020) 139981. https://doi.org/10.1016/j.msea.2020.139981.

[124] A. Aversa, A. Saboori, E. Librera, M. de Chirico, S. Biamino, M. Lombardi, P. Fino, The role of Directed Energy Deposition atmosphere mode on the microstructure and mechanical properties of 316L samples, Addit. Manuf. 34 (2020) 101274. https://doi.org/10.1016/j.addma.2020.101274.

[125] D.R. Feenstra, V. Cruz, X. Gao, A. Molotnikov, N. Birbilis, Effect of build height on the properties of large format stainless steel 316L fabricated via directed energy deposition, Addit. Manuf. 34 (2020) 101205. https://doi.org/10.1016/j.addma.2020.101205.

[126] A. Yadollahi, N. Shamsaei, S.M. Thompson, D.W. Seely, Effects of process time interval and heat treatment on the mechanical and microstructural properties of direct laser deposited 316L stainless steel, Mater. Sci. Eng. A. 644 (2015) 171–183. https://doi.org/10.1016/j.msea.2015.07.056.

[127] M. Bassis, A. Kotliar, R. Koltiar, T. Ron, A. Leon, A. Shirizly, E. Aghion, The Effect of a Slow Strain Rate on the Stress Corrosion Resistance of Austenitic Stainless Steel Produced by the Wire Laser Additive Manufacturing Process, Metals. 11 (2021) 1930. https://doi.org/10.3390/met11121930.

[128] X. Wang, J.A. Muñiz-Lerma, O. Sánchez-Mata, M. Attarian Shandiz, M. Brochu, Microstructure and mechanical properties of stainless steel 316L vertical struts manufactured by laser powder bed fusion process, Mater. Sci. Eng. A. 736 (2018) 27–40. https://doi.org/10.1016/j.msea.2018.08.069.

[129] C. Wang, P. Zhu, Y.H. Lu, T. Shoji, Effect of heat treatment temperature on microstructure and tensile properties of austenitic stainless 316L using wire and arc additive manufacturing, Mater.

Sci. Eng. A. 832 (2022) 142446. https://doi.org/10.1016/j.msea.2021.142446.

[130] P. Guo, B. Zou, C. Huang, H. Gao, Study on microstructure, mechanical properties and machinability of efficiently additive manufactured AISI 316L stainless steel by high-power direct laser deposition, J. Mater. Process. Technol. 240 (2017) 12–22. https://doi.org/10.1016/j.jmatprotec.2016.09.005.

[131] A. Prasad, L. Yuan, P. Lee, M. Patel, D. Qiu, M. Easton, D. StJohn, Towards understanding grain nucleation under Additive Manufacturing solidification conditions, Acta Mater. 195 (2020) 392–403. https://doi.org/10.1016/j.actamat.2020.05.012.

[132] J.A. Dantzig, M. Rappaz, Solidification, EPFL press CRC press, Lausanne (Suisse) Boca Raton (Fla.), 2009.

[133] W. Wang, P.D. Lee, M. McLean, A model of solidification microstructures in nickel-based superalloys: predicting primary dendrite spacing selection, Acta Mater. 51 (2003) 2971–2987. https://doi.org/10.1016/S1359-6454(03)00110-1.

[134] G.P. Dinda, A.K. Dasgupta, J. Mazumder, Texture control during laser deposition of nickel-based superalloy, Scr. Mater. 67 (2012) 503–506. https://doi.org/10.1016/j.scriptamat.2012.06.014.

[135] S. Bahl, S. Mishra, K.U. Yazar, I.R. Kola, K. Chatterjee, S. Suwas, Non-equilibrium microstructure, crystallographic texture and morphological texture synergistically result in unusual mechanical properties of 3D printed 316L stainless steel, Addit. Manuf. 28 (2019) 65–77. https://doi.org/10.1016/j.addma.2019.04.016.

[136] W.H. Kan, M. Gao, X. Zhang, E. Liang, N.S.L. Chiu, C.V.S. Lim, A. Huang, The

influence of porosity on Ti-6Al-4V parts fabricated by laser powder bed fusion in the pursuit of process efficiency, Int. J. Adv. Manuf. Technol. (2022) 1–22. https://doi.org/10.1007/s00170-021-08374-8.

[137] Q. Jia, P. Rometsch, P. Kürnsteiner, Q. Chao, A. Huang, M. Weyland, L. Bourgeois, X. Wu, Selective laser melting of a high strength Al Mn Sc alloy: Alloy design and strengthening mechanisms, Acta Mater. 171 (2019) 108–118. https://doi.org/10.1016/j.actamat.2019.04.014.

[138] X. Qiu, J.W. Thompson, S.J.L. Billinge, *PDFgetX2* : a GUI-driven program to obtain the pair distribution function from X-ray powder diffraction data, J. Appl. Crystallogr. 37 (2004) 678–678. https://doi.org/10.1107/S0021889804011744.

[139] C.L. Farrow, P. Juhas, J.W. Liu, D. Bryndin, E.S. Božin, J. Bloch, T. Proffen, S.J.L. Billinge, PDFfit2 and PDFgui: computer programs for studying nanostructure in crystals, J. Phys. Condens. Matter. 19 (2007) 335219. https://doi.org/10.1088/0953-8984/19/33/335219.

[140] Dmitry, Cluster generator, MATLAB Cent. File Exch. (2023). https://www.mathworks.com/matlabcentral/fileexchange/33449-cluster-generator.

[141] Z. Chen, M.L. Beauvais, K.W. Chapman, Pair distribution function analysis of discrete nanomaterials in *PDFgui*, J. Appl. Crystallogr. 56 (2023) 328–337. https://doi.org/10.1107/S1600576723000237.

[142] K.F. Kelton, A perspective on metallic liquids and glasses, J. Appl. Phys. 134 (2023) 010902. https://doi.org/10.1063/5.0144250.

[143] A.D. Cicco, F. Iesari, S. De Panfilis, M. Celino, S. Giusepponi, A. Filipponi, Local fivefold symmetry in liquid and undercooled Ni probed by x-ray absorption spectroscopy and

computer simulations, Phys. Rev. B. 89 (2014) 060102. https://doi.org/10.1103/PhysRevB.89.060102.

[144] H.P. Wang, C.H. Zheng, P.F. Zou, S.J. Yang, L. Hu, B. Wei, Density determination and simulation of Inconel 718 alloy at normal and metastable liquid states, J. Mater. Sci. Technol. 34 (2018) 436–439. https://doi.org/10.1016/j.jmst.2017.10.014.

[145] W. Lu, J.-C. Tseng, A. Feng, J. Shen, Structural origin of the enhancement in glass-forming ability of binary Ni-Nb metallic glasses, J. Non-Cryst. Solids. 564 (2021) 120834. https://doi.org/10.1016/j.jnoncrysol.2021.120834.

[146] W. Lu, A. Feng, J. Shen, Exploration of the icosahedral clusters in Ni–Nb binary metallic glasses via first-principles theory, J. Non-Cryst. Solids. 575 (2022) 121232. https://doi.org/10.1016/j.jnoncrysol.2021.121232.

[147] H. Fredriksson, E. Fredriksson, A model of liquid metals and its relation to the solidification process, Mater. Sci. Eng. A. 413–414 (2005) 455–459. https://doi.org/10.1016/j.msea.2005.09.024.

[148] Z.W. Wu, M.Z. Li, W.H. Wang, K.X. Liu, Correlation between structural relaxation and connectivity of icosahedral clusters in CuZr metallic glass-forming liquids, Phys. Rev. B. 88 (2013) 054202. https://doi.org/10.1103/PhysRevB.88.054202.

[149] Q. Gao, J. Ai, S. Tang, M. Li, Y. Chen, J. Huang, H. Tong, L. Xu, L. Xu, H. Tanaka, P. Tan, Fast crystal growth at ultra-low temperatures, Nat. Mater. 20 (2021) 1431–1439. https://doi.org/10.1038/s41563-021-00993-6.

[150] H. Song, Y. Sun, F. Zhang, C.Z. Wang, K.M. Ho, M.I. Mendelev, Nucleation of

stoichiometric compounds from liquid: Role of the kinetic factor, Phys. Rev. Mater. 2 (2018) 023401. https://doi.org/10.1103/PhysRevMaterials.2.023401.

[151] Y. Shibuta, S. Sakane, E. Miyoshi, S. Okita, T. Takaki, M. Ohno, Heterogeneity in homogeneous nucleation from billion-atom molecular dynamics simulation of solidification of pure metal, Nat. Commun. 8 (2017) 10. https://doi.org/10.1038/s41467-017-00017-5.

[152] W. Chu, J. Shang, K. Yin, N. Ren, L. Hu, Y. Zhao, B. Dong, Generality of abnormal viscosity drop on cooling of CuZr alloy melts and its structural origin, Acta Mater. 196 (2020) 690–703. https://doi.org/10.1016/j.actamat.2020.07.018.

[153] S. Henry, G.-U. Gruen, M. Rappaz, Influence of convection on feathery grain formation in aluminum alloys, Metall. Mater. Trans. A. 35 (2004) 2495–2501. https://doi.org/10.1007/s11661-006-0229-1.

[154] G. Kurtuldu, P. Jarry, M. Rappaz, Influence of Minor Cr-Additions to the Growth of Columnar Dendrites in Al-Zn Alloys: Influence of Icosahedral Short Range Order in the Liquid, Metall. Mater. Trans. A. 51 (2020) 279–288. https://doi.org/10.1007/s11661-019-05493-6.

[155] M. Inui, K. Maruyama, Y. Kajihara, M. Nakada, Icosahedral ordering in liquid iron studied via x-ray scattering and Monte Carlo simulations, Phys. Rev. B. 80 (2009) 180201. https://doi.org/10.1103/PhysRevB.80.180201.

[156] J.P. Mithen, R.P. Sear, State between Liquid and Crystal: Locally Crystalline but with the Structure Factor of a Liquid, Cryst. Growth Des. 16 (2016) 3049–3053. https://doi.org/10.1021/acs.cgd.6b00209.

[157] H.-H. König, N.H. Pettersson, A. Durga, S. Van Petegem, D. Grolimund, A.C. Chuang,

Q. Guo, L. Chen, C. Oikonomou, F. Zhang, G. Lindwall, Solidification modes during additive manufacturing of steel revealed by high-speed X-ray diffraction, Acta Mater. 246 (2023) 118713. https://doi.org/10.1016/j.actamat.2023.118713.